LBNL-42663

ERNEST ORLANDO LAWRENCE
BERKELEY NATIONAL LABORATORY

Photodissociation and Reaction Dynamics Studies Using Third-Generation Synchrotron Radiation

Arthur G. Suits

Chemical Sciences Division

January 1999

Published as a chapter in
Chemical Applications of Synchrotron Radiation,
T.K. Sham, Ed.,
World Scientific,
Singapore, 1999

DISCLAIMER

LBNL-42663

Photodissociation and Reaction Dynamics Studies Using Third-Generation Synchrotron Radiation

Arthur G. Suits

Chemical Sciences Division
Ernest Orlando Lawrence Berkeley National Laboratory
University of California
Berkeley, California 94720

January 1999

This work was supported by the Director, Office of Energy Research, Office of Basic Energy Sciences, Chemical Sciences Division, of the U.S. Department of Energy under Contract No. DE-AC03-76SF00098.

Photodissociation and Reaction Dynamics Studies Using Third-Generation Synchrotron Radiation

Arthur G. Suits

1. Introduction

Application of the universal crossed molecular beams method to problems in bimolecular scattering and photodissociation have had a profound impact on our understanding of the underlying mechanisms of chemical reactions.[1] In most cases these experiments achieve universality in product detection by means of electron impact (EI) ionization.[2] Product angular and translational energy distributions are measured by time-of-flight of the neutral products. With the use of EI, a very steep price is paid to achieve the universality that has led to so many successful experiments. Principal among these

shortcomings of EI based experiments is fragmentation of the neutral molecules leading to appearance of the product ion at a different mass-to-charge ratio than that of the neutral. This greatly complicates interpretation of the experimental results, particularly for complex molecules and hydrocarbons where fragmentation is especially troublesome. The development of third generation synchrotron radiation sources with associated VUV photon fluxes greater then 10^{18} photons/cm^2/s has opened the door to a new era in universal crossed-beam scattering studies relying on VUV photoionization (PI) rather than EI. A universal crossed molecular beam endstation employing tunable undulator radiation for product photoionization based detection has recently been constructed on the Chemical Dynamics Beamline[3] at the Advanced Light Source.[4] This chapter will be devoted to introducing this apparatus and documenting the range of experiments that can be carried out.

2. Experimental

The endstation is based in principle on a single molecular beam source apparatus[5] employing EI detection that has been used very successfully for photochemistry studies. The design has been adapted to feature two crossed molecular beams along with oil free pumping to ensure compatibility with the synchrotron storage ring vacuum requirements.

The machine, shown schematically in Fig.1, features two differentially pumped molecular beam sources each of which is pumped by 2000 l/s high-throughput magnetic bearing turbomolecular pumps. The sources are fixed at 90° and housed in a chamber that rotates about an axis parallel to the undulator probe beam. The molecular beams cross

inside a main chamber pumped by a 2000 l/s turbopump. Scattered products fly out of the interaction region and those that enter a small aperture pass into a triply differentially pumped UHV detector region which with pressures maintained typically about 10^{-10} Torr. Product detection is accomplished by ionization of the neutral fragments some 15cm from the interaction region by tunable undulator light. The characteristics of the undulator radiation 'white beam' are a flux of 10^{16} photons/second with an energy spread of 2.2% FWHM. The resulting ions are then extracted from the ionization region, mass selected by means of a quadrapole mass filter and then counted using a Daly ion detector. The data is then recorded as a function of time and scattering angle to reconstruct the primary product velocity distributions from the scattering or photochemical event. The use of tunable undulator radiation-based PI in place of EI has many compelling advantages. First, as mentioned earlier, EI leads to dissociative ionization of parent and product molecules resulting in very large backgrounds at certain masses greatly complicating interpretation of the experimental results. Universal PI based detection, on the other hand, can be used in such a way that it is at once selective and universal. The photon energy can be tuned so that the molecule of interest can be detected but below the threshold for any dissociative ionization process. A second shortcoming of EI is that hot filaments are used to produce the flux of electrons. These filaments typically operate at temperatures of around 2000° C, resulting in much higher partial pressure of background gasses and further contributing to background interference problems. Yet another difficulty of EI is that, in order to minimize space charge problems, the size of the ionization region has to be large, typically on the order of 1 cm. As a result, this leads to

an associated uncertainty in the point of ionization and a corresponding uncertainty in the velocity inferred from the time of flight measurement. The undulator beam from a third generation synchrotron source, on the other hand, can be focused to yield a very small ionization volume. In this apparatus it is on the order of 0.25 mm in length. In consequence the location of the ionization region is very well determined, so that this contribution to the velocity uncertainty is negligible. Finally, the use of a cold photon beam in place of the hot filament allows us to use liquid helium cooling for cyropumping around the ionization region. In addition to the practical advantages sketched above for photoionization vs. EI, PI offers new opportunities simply not available to EI based systems. In particular, photoionization efficiency (PIE) curves for products can be measured, providing some information on the ionization thresholds for products, and insight into the internal energy content or electronic state of the product.

Figure 2 illustrates some of the advantages of PI over EI based studies. This figure shows a pair of time of flight spectra resulting from photodissociation of methylamine at 193 nm, specifically looking at the methyl + NH_2 channel. This channel is a minor channel, less then 1% of the total dissociation yield. Using EI, the methyl at m/e 15 is notoriously difficult to detect owing to interference from methane, a common contaminant in most machines. This methane contaminant also contributes signal at mass 16, where NH_2 would appear, making detection of either of these species extremely problematic in EI based machines. As can be seen in Fig. 2, very good signal-to-noise is obtained with just $4X10^5$ laser shots for both of these species, despite the fact that this is a minor channel. The solid lines show excellent momentum matching between the two cofragments. In addition to the improved signal-to-noise from reduced background

contributions, there is no evidence of dissociative ionization that would complicate interpretation of these spectra. The dominant photoproduct in these experiments would be CH_2NH_2, the H-loss channel, which in EI studies would overwhelm both the mass 15 and mass 16 primary products.

Figure 3 illustrates this additional feature of PI that the product internal states can be probed by varying the wavelength of the probe light. Shown in Fig. 3 are a series of time of flight spectra for the O_2 product from ozone photodissociation at 193 nm. The peaks are marked showing the dominant channels assigned in previous work.[6] The use of the tunable VUV allows for discrimination successively between the ground state O_2 (X) product (the fastest peak) the O_2 a ($^1\Delta_g$) state (the dominant peak at the low photon energy), and the b ($^1\Sigma_g^-$) state, and finally highly vibrationally excited levels of the ground state. No practical analogy exists in EI based studies.

3. Photochemistry

3.1 Dimethyl sulfoxide

Among the compelling advantages of PI-based photodissociation studies using photofragment translational spectroscopy (PTS) is the ability to study complex systems and complex dissociation processes in great detail. This is well illustrated in the recent study[7] of the photodissociation of dimethyl sulfoxide (DMSO). Earlier investigations based on state-resolved resonance-enhanced multiphoton ionization (REMPI) probe of the methyl radical in conjunction with laser induced fluorescence (LIF) studies on the SO product[8], concluded that the dissociation mechanism for DMSO at 193nm was a concerted one and which both methyl radicals departed simultaneously. This conclusion

was based on the observation of internally cold methyl radical products and the REMPI studies. Recent studies on the Chemical Dynamics Beamline, however, using the tunable VUV probe have found the dissociation mechanisms to be considerably more complex than previously supposed. Fig. 4 shows time of flight (TOF) spectra for the CD_3SO product from dissociation of deuterated DMSO at angles of 12° and 22.5°. The observation of this intermediate, made possible through the use of the tunable, soft ionization, demonstrates conclusively that this dissociation is stepwise rather than concerted. Furthermore, as is apparent in the TOF spectra and in the corresponding translational energy distribution shown in Fig. 5, this product arises from two distinct channels. One with considerable translational energy release, greater than 25 kcal/mol, and the other peaking at much lower translational energies, around 8 kcal/mol. The TOF spectra for the corresponding methyl radicals, shown in Fig. 6, mass 18 for CD_3^+, are momentum-matched to the sulfonyl intermediate shown in Fig. 4. It is worth noting that these very high signal-to-noise (S/N) time of flight spectra are recorded at m/e 18, a peak in the water background for conventional mass spectrometers. The use of the tunable VUV allows for probing CD_3 well below the ionization potential of water, resulting in greatly reduced background at these masses. In addition to the primary contributions shown in the methyl radical TOF spectra, there are also contributions from secondary decomposition of the intermediates. In fact, by fitting the TOF spectra for the methyl and the intermediates simultaneously, one can extract directly the fraction of intermediates that undergo secondary decomposition to give a second methyl radical. This is shown in Figure 7 where the shaded area represents the fraction of the primary sulfonyl

intermediates that subsequently decompose to give an additional methyl radical and an SO molecule. In addition, the SO product could be momentum-matched to the methyl from secondary decomposition of the sulfonyl intermediates shown in Fig. 5a.

The results for DMSO-h6 shows some fascinating differences from those for the perdeuterated molecule. Most significantly, no CH_3SO intermediates were observed. It is believed that the inability to observe these arises from several experimental factors. Foremost among these is that a larger fraction of the CH_3SO intermediates in the slow primary dissociation process undergo secondary decomposition. In addition, it appears that the fast channel is less important in DMSO-h6 than in DMSO-d6. In fact, the largest problem arises from the difficulty in resolving the mass 62 and mass 63 contributions, that is, the CH_3SO and CH_2SO fragments. For the DMSO-h6 a very substantial signal was observed at mass 62, that is, CH_2SO. All of these results are summarized schematically in Fig. 8. Initial decomposition of the molecule leads to the sulfonyl intermediate and methyl radicals via two different primary pathways: one likely involving an electronically excited sulfonyl intermediate, one occurring on the ground state surface. The former corresponds to the fast channel shown in Fig. 5 used to fit the TOF spectra. The ground state CH_3SO can then undergo secondary decomposition via two channels that have comparable barriers: one involves CS bond scission yielding a second methyl radical plus SO. Another channel slightly higher in energy results from C-H bond scission in the sulfonyl intermediate to yield CH_2SO and a hydrogen atom. It is likely that the barrier for the latter channel is a bit higher than the former channel and it is clear that tunneling through this barrier is important. Several key aspects of the use of tunable undulator radiation have made it possible to unravel these complex processes. One is the

ability to tune the VUV probe below the onset of dissociative ionization processes for some channels, making near background-free TOF measurements possible. Second is the knowledge of the probe photon energy. Even in the case where dissociative ionization is possible, its presence or absence is used to provide some insight into the internal energy in the products. Finally, the universal nature of the detection scheme allows for essential momentum-matching to exclude multiphoton and secondary decomposition processes and to allow for quantitative assignment of the branching into various channels.

3.2 Substituted Ethylenes

Another class of systems that shows clearly the power of tunable undulator radiation in conjunction with PTS is a collaborative study of the photodissociation dynamics of substituted ethylenes[9] involving the Brookhaven group of North and Hall, with the Berkeley team of Blank, Suits and Lee. Ethylene and the substitute ethylenes are a widely studied class of molecules that exhibit a strong $\pi^* \leftarrow \pi$ transition in the vicinity of 190 nm. We will first consider the dissociation of acrylonitrile or cyanoethylene and contrast its photodissociation dynamics with those of the more widely studied vinyl chloride system.

3.2.1 Acrylonitrile

Results for acrylonitrile dissociation at 193nm obtained on the Chemical Dynamics Beamline show four distinct dissociation channels, and the results are consistent with the occurrence of all of these on the ground state potential energy surface

following internal conversion from the excited state. Hydrogen elimination results in the C_3H_2N radical, m/e 52. TOF spectra for this product are shown in Fig. 9 along with the result of a forward convolution simulation. The energy distribution used to fit these spectra is shown in the Fig. 10 and compared with a statistical prior distribution. In addition to measuring the TOF spectra, one can also record a low-resolution photoionization efficiency (PIE) spectrum for this radical simply by tuning the undulator gap. This is shown in Fig. 11 at a source angle of 7.5°. The observed photoionization onsets depend on a complex combination of factors since the detected products contain unknown amounts of internal energy, and the influence of this internal energy on the photoionization threshold is not clear. Based on the energy release, the radicals that are probed in this figure contain an average of 20 kcal/mol internal energy. Since it is not clear how this energy will manifest itself in the shift of the photoionization spectrum, the onset measured 9.3±0.3 eV actually represents a lower limit to the IP of cold C_3H_2N radicals.

In addition to the hydrogen elimination channel, molecular hydrogen elimination is also observed. The corresponding TOF spectra are shown in Fig.12 at probe photon energies of 12 and 14 eV. This figure illustrates well the use of the tunable VUV to investigate the nature of different contributions to the TOF spectrum. At 12 eV, a spectrum more closely representing that of the C_3HN radical product is observed. As the probe energy is increased to 14 eV, however, a larger contribution of dissociative ionization at mass 52 is seen. This dissociative ionization contribution is fitted using the same distribution used in fitting the hydrogen elimination channel. As a result, these

relative contributions are now well determined. The results then yield the translational energy distribution shown in Fig. 13.

In addition to H and H_2 product channels, CN and HCN are also observed as primary products. In fact these two channels show precisely the same mass combination: HCN plus C_2H_2 is 27 and 26, and vinyl plus CN is 26 and 27. In traditional PTS experiments employing EI, it would be impossible to distinguish these dissociation channels. However the selectivity afforded by the VUV probe allows direct investigation of these two entirely different dissociation channels. The photoionization spectrum for the mass 27 product is shown in Fig. 14 at a scattering angle of 15°. The spectrum has a dominant feature with an onset of around 11 eV and a small shoulder with an onset of around 8.5 eV. Since the two possible products for this mass are HCN and the vinyl radical with ionization potentials of 13.6 and 8.6 eV respectively, the relative contributions in the spectrum are clear and the molecular product, HCN, is unquestionably the dominant channel. This is made even clearer in the corresponding TOF spectra for m/e 27 products shown in Fig. 15 at probe photon energies of 10 and 15 eV, respectively. These spectra show entirely different distributions owing to the fact that the minor channel has a lower ionization onset. The radical channel dominates the TOF spectrum at the lower probe photon energy. When the photon energy is increased so that both channels are detected, the dominant molecular channel overwhelms the small radical signal, yielding the TOF spectrum characteristic of the dominant molecular channel. The cofragment at m/e 26 reveals analogous behavior as shown in Fig. 16. The PIE spectrum is shown contrasted with that of cold acetylene seeded in a molecular beam. The

ionization onset is clearly suppressed relative to the cold acetylene beam, on the order of 1-1.5 eV.

These results, in conjunction with known values for the energetics of the various dissociation channels, lead to the following picture for the overall dissociation mechanism. Four channels are observed in the 193nm dissociation of acrylonitrile: atomic and molecular hydrogen elimination, and HCN and CN elimination. There is evidence that all of these processes occur on the ground electronic surface following internal conversion from the initially prepared state. The product translational energy distributions show a near statistical bond rupture for the radical channels and substantial recombination barriers for the molecular channels.

3.2.2 Vinyl Chloride

Vinyl chloride remains the most intensely studied substituted ethylene owing to its rich photochemistry and the availability of convenient laser probes for many of the products.[10-20] It provides a compelling illustration of the application of third-generation synchrotron radiation to reveal overlooked features and to provide new insights into the dynamics. Figs.17 and 18 show a schematic energy diagrams indicating the available primary dissociation channels and estimated barriers for molecular and radical elimination channels, respectively. We first consider the atomic hydrogen elimination channel, which can occur in conjunction with secondary decomposition of the chlorovinyl radical. Chlorovinyl, C_2H_2Cl, is observed as a primary product and TOF spectra have been recorded at a number of angles and a number of probe photon energies. Fitting of the TOF spectra yields the translational energy distribution for the primary hydrogen

elimination channel shown in Fig. 19. Note that this figure only extends to a minimum at around 11 kcal/ mol. At energies below that, m/e 61 is not seen owing to secondary decomposition of the unstable radicals containing greater than 36 kcal/mol internal energy. This truncation of this energy distribution shows a barrier to C-Cl bond cleavage in the radical that exceeds the endothermicity of the process by 11 kcal/mol, further implying a barrier to the reverse addition of chlorine to C_2H_2. A second channel observed in these experiments is molecular hydrogen elimination yielding mass 60, CH_2Cl. Time of flight spectra for the CH_2Cl product are shown in Fig. 20 at a probe photon energy of 12 eV. The dominant component at a scattering angle of 10° and the sole component at 15° is the primary H_2 elimination channel, fitted with the translational energy distribution shown in Fig. 21. This $P(E_T)$ has a roughly gaussian profile with an average translational energy release of 18±2 kcal/mol. The minor contribution to the time of flight spectrum at 10° arises from dissociative ionization of the chlorolvinyl intermediates.

A third observed channel results from HCl elimination from vinyl chloride, probed at mass 36, HCl^+. Fits to the time of flight spectra for HCl^+ shown in Fig. 22 yield the $P(E_T)$ in Fig. 23, showing a maximum probability of 12 kcal/mol, extending to 70 kcal/mol, with an average value of 18 ± 1 kcal/mol. The PIE spectrum for HCl, mass 36, is shown in Fig. 24 at a scattering angle of 20°. This spectrum shows a photoionization onset for this detected HCl fragment of 10.5 ± 0.3 eV. Comparison of this with the HCl ionization potential of 12.75 eV shows a profound red shift, greater than 2 eV, in the photoionization onset. This red shift shows a dramatic influence of internal excitation on

the HCl photoionization spectrum, revealing that a great deal of this internal energy is available for ionization.

A fourth primary decomposition channel involves direct chlorine elimination and can lead to secondary decomposition of the vinyl radical products. TOF spectra for mass 27, the vinyl radical, has angles of 15° and 25° and a probe photon energy of 11 eV are shown in Fig. 25. Vinyl radicals can only originate from primary C-Cl bond cleavage and have been fitted with the $P(E_T)$ shown in Fig. 26, assuming chlorine as the momentum matched partner fragment. This energy distribution is roughly gaussian in shape with an average energy release of 23 kcal/mol. Looking now to the partner fragment, Fig. 27 shows the TOF spectrum for mass 35, Cl^+, at several scattering angles, and a probe energy of 14 eV. These spectra have been fitted with three components. One very fast component, shown as dashed lines, is that shown in Fig. 26, derived from fitting the vinyl radical TOF spectrum. The remaining slow components in the chlorine spectra were fitted using two contributions: one representing a primary decomposition on the ground state surface, i.e. the $P(E_T)$ in Fig. 28. The second slow contribution is from secondary decomposition of chlorovinyl radicals. The energy distribution for the slow chlorine, shown in Fig. 28, peaks at only 0.5 kcal/mol decreasing to a limit of only 7 kcal/mol. The complex shape contains contributions from at least two components. In fact, the translationally slow chlorine atoms have no corresponding matching vinyl radicals. The absence of the slow vinyl radicals matching the chlorine are strong evidence of secondary decomposition of these intermediates. In addition, the $P(E_T)$ for the chlorine shows a contribution from C-Cl bond cleavage in the chlorovinyl intermediates as a further

secondary decomposition channel. The fits used to produce these energy distributions are quite sensitive to the secondary decomposition process, less so to the primary channel. The resulting energy distribution has a maximum probability at 8 kcal/mol, consistent with the recombination barrier measured of 11 ± 2 kcal/mol.

These experiments have allowed for determination of the branching fractions for each of the three atomic chlorine elimination channels that contribute to the time of flight spectra shown in Fig. 27. The fast primary chlorine elimination channel accounts for 86% of the total product chlorine atom, the slow primary channel accounts for 7% and secondary decomposition of the chlorovinyl radicals, an additional 7%. None of the fast and all of the slow vinyl radicals apparently undergo secondary decomposition so that this chlorine branching distribution provides a direct calibration of the primary H atom yield relative to the primary chlorine yield, and a good estimate of the ratio of primary to secondary H atoms.

The PIE spectrum for the vinyl radical is shown in Fig. 29 at a scattering angle of 23°. These stable vinyl radical products are only formed in coincidence with fast fragments, i.e., they contain relatively little internal energy. This figure shows a photoionization onset of 8.3 ± 0.3 eV for the vinyl radical, consistent with the lower of recently reported values for the ionization potential for the vinyl radical.

The results for the HCl elimination channel are more or less in agreement with the previously reported results showing considerable energy in vibration in the HCl product. A question remains about the identity of the C_2H_2 partner fragment for the HCl. This could be either acetylene (HCCH), or vinylidene ($:CCH_2$) ground state, or an excited

triplet vinylidene or acetylene. The latter are spin forbidden processes and no evidence is seen to suggest their presence in the spectra. The energy distribution suggests a barrier on the order of 12–13 kcal/mol or larger while calculations suggest a very small barrier for 1,1 HCl elimination. However, Gordon and co-workers have recently argued[21] that a larger translational energy distribution than expected for this process (formation of vinylidene) may well arise from contributions from the isomerization of vinylidene to acetylene on a time scale comparable to that of the separation of the fragments. Another view is simply that the reaction path involves extensive H atom motion and that the resulting energy is available for repulsion between the fragments of HCl and acetylene thereby formed.

For the molecular hydrogen elimination channel, these results represent the first study using universal detection. In general, they agree with the previous probes in areas where there are overlapping measurements. The atomic elimination channels, however, are not entirely consistent with previous work. For the H atom elimination channel, for example, Mo[22] and co-workers reported isotropic Doppler profiles for the H product and attributed this to electronic predissociation apparently involving internal conversion from the initially prepared state. In addition, they reported a very large average translational energy release of 17 kcal/mol for the H atom product. This is 35% of the available energy and somewhat inconsistent with barrierless dissociation in the ground state. In contrast to this, our measured distribution, which only includes contributions greater than 11 kcal/mol, provides an upper limit for the average translational energy release of 18 kcal/mol. In addition, from measurement of the chlorine products from secondary decomposition of the chlorovinyl radicals, there is strong evidence that the total primary

$P(E_T)$ must extend well below the truncation point so that the average translational energy release for the hydrogen atoms is likely to be much lower than our upper limit of 18 kcal/mol. In fact the energy distributions for the analagous H atom products and ethylene and acrylonitrile photodissociation at 193 were found to be consistent with statistical partitioning of available energy. At present it is difficult to reconcile the measurements of Mo et al. with these observations, but it is important to note that in the PI studies there is momentum-matching for both primary and secondary products. This provides an important check on the analyisis and interpretation that is not generally possible in the laser based studies. For the atomic chlorine elimination, Umemoto et al.[23] originally suggested two different dissociation channels from C-Cl bond cleavage on distinct potential energy surfaces, with the low velocity channel assigned to ground state dissociation and the fast channel assigned to direct dissociation involving the n-σ^* state localized on the C-Cl bond. These measurements show that the direct chlorine elimination channel accounts for 86% of the chlorine fragments in good agreement with the 84% reported by Suzuki and co-workers, but significantly larger than that deduced from REMPI-Doppler 6,9 measurements. In addition, the average translational energy release agrees with previous measurements. A comparison of the ground state chlorine elimination channel energy distribution to that expected on the basis of the statistical prior distribution suggests that there may not be complete randomization of the available vibrational energy prior to dissociation.

Using PTS with tunable VUV undulator radiation, a detailed investigation of these complex dissociation mechanisms is possible. In vinyl chloride following

excitation of the π-π^* transition at 193nm, one primary channel is observed to take place on the initially prepared excited surface while four additional primary dissociation mechanisms occur on the ground state surface following internal conversion from the initially prepared state. These include molecular channels, HCl and H_2 elimination, in addition to atomic elimination processes yielding hydrogen atoms and chlorine atoms. The results allow for a direct measurement of the recombination barrier for the chlorine plus acetylene reaction of 11 kcal/mol, suggesting this channel represents a concerted path of the formation of the α-chlorovinyl radical; hence the β-chlorovinyl radical is not expected to have a significant barrier. In addition, the photoionization spectrum measured for the HCl products shows a dramatic red shift in the photoionization onset which provides the opportunity for future detailed probes of the contribution of vibrational energy to the photoionization spectrum.

3.3 Oxalyl Chloride

Recent studies of the photochemistry of oxalyl chloride at 193nm on the Chemical Dynamics Beamline[24] show clearly how these universal studies can complement state-resolved laser based measurements in important ways. In a photofragment imaging study of oxalyl chloride dissociation near 230nm,[25] translational energy and angular distributions were obtained for both ground state and spin orbit excited chlorine atoms, as well as a number of rotational levels of the ground vibrational state of CO. On the basis of the observed distributions, an unusual dissociation mechanism was proposed in which, following the absorption of a photon, a strong impulse occurs between one of the chlorine atoms and one of the CO moieties with the CC bond breaking simultaneously

and with little concomitant momentum transfer to the ClCO fragment. The latter then undergoes secondary decomposition on a longer time scale, yielding, in total, two chlorine atoms and two CO molecules, each showing distinct translational energy and angular distributions. This unusual process, a concerted three-body dissociation followed by secondary decomposition of the ClCO, results in four photofragments arising out of absorption of a single UV photon. This is possible in oxalyl chloride owing to the relatively weak (25 kJ/mol) Cl-CO bond.[26] However, a number of questions remained following the laser-based studies. No chloroformyl radical product was detected in the original imaging experiments since those studies were based on resonant photoionization and no suitable transitions were known for ClCO. In addition, uncertainties remained in the branching among the various products owing to uncertainties in the relative line strengths for the probe transitions and in the deconvolution of the two different velocity components for the Cl and CO products. Finally, because the CO distributions were measured state-specifically, it was not possible to get the overall translational energy distributions for the CO. To address these outstanding questions, the photodissociation of oxalyl chloride was studied at 193nm using PTS on the Chemical Dynamics Beamline at the Advanced Light Source.

Time-of-flight spectra are shown for the CO (m/e 28) and Cl (m/e 35) products in Fig. 30 and 31, respectively . The ability to detect CO with this excellent signal-to-noise clearly shows one of the virtues of the apparatus and the use of tunable VUV probe. For m/e 28 (CO^+), the TOF spectra were obtained with 10^5 laser shots and 14.5 eV undulator radiation. For both of these products, it is clear that there is more than one dissociation

channel contributing. The data at 25° exhibits a fast component peaked at 55 μs and a slow component showing a clear shoulder near 100 μs. In addition to these masses, primary photofragments were observed at m/e 63, $ClCO^+$. This represents the first direct gas phase observation of this species. Analysis of the TOF spectra for all of these fragments yield the translational energy distributions shown in Fig 32. For CO the relative contributions obtained were 37% slow and 63% fast. The uncertainties in these values are large because of the range of possible approaches in decomposing the two contributions; however, the imaging experiment provided some guidance since the spin-orbit excited Cl was probed separately and showed exclusively the fast component. This provides some assurance about the shape of the distribution used to fit the fast component, which correspondingly constrains all of the fitting. While the slow dissociation channel is peaked near zero, the fast channel is peaked at 10 kcal/mol and extends to around 19 kcal/mol. For CO, the average energy release in the slow component is 2.5 kcal/mol; in the fast component it is 10.0 kcal/mol; the total average translational energy in CO is 7.2 kcal/mol. For the Cl fragment, the relative contributions obtained were 41% for the slow component and 59% for the fast component (c.f. 37% slow and 63% fast for CO). These are certainly equivalent within the range of uncertainty in the analysis. The average energy in the slow Cl was 3.5 kcal/mol, and in the fast Cl, 11.0 kcal/mol. The total translational energy in Cl was 7.9 kcal/mol. The ClCO translational energy distribution is a single contribution given in Fig. 32c, which shows small and narrow peak at low energy. The sharp edge of the lower energy side indicates that ClCO radicals with low velocity do not survive, and decompose into CO

and Cl. The minimum translational energy observed is about 1.0 kcal/mol and the average energy is 4.6 kcal/mol. ClCO products with energies down to 0.3 kcal/mol should be within the range of the detector at 10°. Based upon the fitting of the Cl and CO above, if one assumes the fast component must equal the slow component except for that portion that remains bound as ClCO, one obtains an estimate of the fraction of ClCO that remains bound. From the analysis of the CO, we find 21% of the ClCO might remain bound, while from the Cl analysis the fraction is 15%, giving an average of 18%. Again, these values are within the range of uncertainty associated with the analysis.

These observations suggest a simple picture of the dissociation dynamics similar to that proposed for photodissociation of oxalyl chloride at 230nm: the multiple bond-breaking processes for oxalyl chloride consists of two dissociation steps. The first step is an impulsive three-body dissociation,

$$(ClCO)_2 \rightarrow CO + Cl + ClCO$$

which yields fast CO, Cl, and the chloroformyl radical ClCO. The measured distributions imply that little momentum is transferred to the ClCO in this step, with the impulse primarily along the C-Cl bond. In the second step, most of the remaining ClCO undergoes subsequent decomposition:

$$ClCO \rightarrow CO + Cl$$

which yields slow CO and Cl. As suggested by the fast components of TOF spectra in Fig. 30 and 31, the fragments CO and Cl seem to be dynamically linked, that is, it is likely to break both the C-C and C-CCl bonds simultaneously. The direct observation of ClCO here confirms it as a primary product, and the translation energy distributions in

Fig. 32 show clearly that there is no fast contribution in that product, consistent with the picture outlined above. The results confirm a previous study at 230 nm using the photofragment imaging technique, and provide a broad view of the overall dynamics of the process and details of the branching fractions unavailable to laser-based studies. The use of this universal technique allows for complementary global insights into the dynamics when combined with the previous photofragment imaging study.

3.4 Propyne and Allene

A final illustration of the range of possibilities available for photochemistry studies using tunable VUV probe is provided by a recent study by Neumark and coworkers on the photodissociation of allene and propyne, two distinct C_3H_4 isomers.[27] In general for hydrocarbon photodissociation cleavage of the various inequivalent C-H bonds will result in chemically distinct isomers with the same mass, thereby complicating the identification of the primary photodissociation products. EI based studies cannot distinguish among isomers except in unusual cases. Laser-based methods such as laser-induced fluorescence or REMPI can do better, but this requires a fuller understanding of the electronic spectroscopy of polyatomic hydrocarbon radicals than is generally available. While C-H bond fission in allene can lead only to propargyl radical production (CH_2CCH), propyne can yield either the propargyl or propynyl (CH_3CC) radical, with latter energetically disfavored by 41 kcal/mol. In 1966, Ramsay and Thistlethwaite found that the flash photolysis of allene and propyne gave the same band structure as the propargyl radical,[28] suggesting that either the other C_3H_3 isomers have a lifetime shorter

than 25 μs or both precursors produced the C_3H_3 as propargyl radical. In 1991, two isotopic studies[29] were performed which show that photodissociation of propyne breaks the acetylenic C-H bond, but there was no evidence that the CH_3CC radical does not rearrange to CH_2CCH radical.

Fits to TOF spectra obtained on an EI-based instrument, confirmed on the PI machine, yielded center-of-mass translational energy distributions shown in Figs. 33a and 33b for propyne and allene, respectively. Although the two translational energy distributions are quite similar, the photoionization efficiency (PIE) curves for the C_3H_3 photoproduct from propyne and allene, shown in Figs. 34a and b, respectively, are very different. These were obtained on the Beamline at the laboratory angles indicated. At Θ=10°, the C_3H_3 product from propyne photodissociation shows an onset at 10 eV, whereas that from allene photodissociation shows an onset at 8 eV. Comparison with published values for the IPs indicates that the C_3H_3 isomer from propyne dissociation is primarily the propynyl radical, while the C_3H_3 isomer from allene is the propargyl radical. This is confirmed by the PIE curve for C_3H_3 from propyne at Θ=15° (Fig. 35), which was recorded outside the Newton circle for propynyl radical. The 8 eV onset is gone, and the remaining curve is quite similar to the propargyl curve from allene shown in Fig. 34b. In fact, this minor contribution may simply arise from allene impurity in the propyne beam.

The acetylenic bond in propyne is characteristically very strong, about 130 kcal/mol, whereas that for the methyl C-H bond is 89 kcal/mol. It is thus clear that 193 nm photolysis of propyne results in cleavage of the stronger bond. This bond selective dissociation likely occurs owing to the proximity of the acetylenic bond to the C-C π

bond on which the initial electronic transition is localized. Although the propynyl radical can in principle isomerize to the lower energy propargyl radical, this study shows that this does not happen. A recent theoretical study predicts an isomerization barrier of 60 kcal/mol for this process,[30] but since the photon energy at 193 nm is 148 kcal/mol, only 18 kcal/mol internal energy at most is available for propynyl product and isomerization is not expected.

4.0 Reactive Scattering

Metathesis reactions, in which a single atom is transferred from a stable molecule to an atom or radical, are the only truly bimolecular (i.e. bimolecular in both directions) gas phase reactions.[31] Those involving hydrogen atom transfer arguably represent the most important subclass of this vast body of reactions; for combustion dynamics this is clearly so. Free radical abstraction of hydrogen atoms in saturated hydrocarbons, for example, are reactions of great importance in combustion, and the differing propensities for reaction of primary, secondary, or tertiary H atoms, as well as the different dynamics underlying these pathways, are important to a detailed understanding of combustion chemistry. Crossed molecular beam scattering remains the most powerful means of investigating these fundamental reactive encounters, and the combination of intense, tunable VUV synchrotron radiation with the crossed beam technique on Beamline 9.02 is yielding important new insight into these reactions. The crossed-molecular beam technique has been used with a universal yet selective tunable VUV probe to measure double differential cross sections for reaction of Cl

atoms with saturated hydrocarbons. The use of tunable undulator radiation provides the unprecedented ability to probe the hydrocarbon radical fragment directly in these reactions.

An important pair of papers by Andresen and Luntz in 1980[32] reported experimental and theoretical studies of the reaction dynamics of $O(^3P)$ with a variety of saturated hydrocarbons chosen to underscore distinct trends in the reaction dynamics for primary, secondary or tertiary H atom abstraction. The trends they observed for the OH rotational state distributions have been confirmed in all subsequent studies of H abstraction dynamics, viz., all the newly formed hydride products, regardless of the identity of the hydrocarbon or the attacking atom, are formed rotationally cold. This was ascribed to the importance of a collinear O-H-C transition state (TS) in these reactions. In addition, they found that the more exothermic the process (exothermicity increases in the sequence primary < secondary < tertiary), the greater the yield of vibrationally excited OH product, with tertiary H atom abstraction preferentially populating v=1. They argued that this arises from a shift in the nature of the surfaces from repulsive to attractive across the series, with the more product-like TS for primary H abstraction favoring vibrationally cold products while the more reactant-like TS for the tertiary H abstraction yields greater vibrational excitation. Studies of the dynamics of chlorine atom reactions with hydrocarbons were stimulated in the early 90's when it was realized that these reactions represent a possible termination step for the chlorine-atom catalyzed ozone destruction cycle in the stratosphere. In recent years, considerable experimental effort has been devoted to understanding the detailed dynamics of these reactions. A pioneering series of papers from the Zare laboratory[33,34,35,36] reported studies of Cl reaction with both vibrationally excited and ground state methane

molecules, using their 'photoloc' technique to provide state-resolved differential cross sections for these reactions. Reaction of Cl atoms with vibrationally excited methane was found to be quite facile, showing the characteristic cold rotational distribution but predominantly forward scattered HCl, especially for the vibrationally excited HCl product. They argued that the association of low rotational excitation with a collinear TS, as adduced by Andresen and Luntz in the $O(^3P)$ reactions and Flynn and coworkers for the Cl-C_6D_6 reaction, is strictly appropriate only when there is impulsive energy release in the reaction. Varley and Dagdigian have reported an extensive investigation of the reaction dynamics of Cl with simple hydrocarbons using a technique similar to the 'photoloc' method employed in Zare's experiments. In these studies, state-resolved differential cross sections were obtained for the HCl product from reaction with a number of hydrocarbons including methane, propane, isobutane, and selectively deuterated propane. They observed backscattered HCl from the isobutane reaction, and vibrational population ratios that were similar for propane and isobutane, in contrast to the $O(^3P)$ results of Andresen and Luntz. Their results for the partially deuterated propane showed abstraction of the D atoms (as the primary substituents) led to sideways scattered DCl product, while abstraction of the H atoms (the secondary substituents) led to a more isotropic angular distribution, yet still favoring the backward direction. It must be noted that their collision energies were very broad, and extended to very high energies, owing to the crossed-flow conditions. It is also important to recognize that the distributions obtained in these laser-based studies are largely blind to internal energy in the undetected product. Often the assumption is made that the undetected product is internally cold. We

will see in the studies below based on universal product detection that this may be far from the truth in some cases.

Crossed molecular beam studies, traditionally using "universal" EI-based detection have proven to be powerful tools for obtaining a complete picture of bimolecular reaction dynamics under single collision conditions for an extensive list of chemical reactions.[40, 41] However, these hydrogen atom abstraction reactions present a serious challenge to this technique. Crossed molecular beam reactive scattering experiments generate an extremely small number density of products at the detection region, placing a premium on detection sensitivity for the reaction products. Discriminating against the large background from scattered reactant ^{35}Cl and ^{37}Cl when attempting to detect the signal from HCl products requires very high mass resolution, associated with very low quadrupole transmission and reduced product signal. There is also background from HCl contamination in the Cl beam. Detection of the radical product is even more problematic since the scattered hydrocarbon reactant will dissociatively ionize to give the radical ion (as well as smaller fragments) in the electron bombardment ionizer, resulting in tremendous background that cannot be avoided with mass filtering. As a result, these studies have not been possible using conventional means. Using tunable VUV synchrotron radiation for photoionization of the product molecules in place of electron bombardment provides a solution to these problems. Tuning the VUV probe energy above the ionization potential (IP) of the radical products but below the IP for the parent hydrocarbon provides discrimination against any background generated from dissociative ionization of scattered reactants and allows near background-free detection of the radical products. In addition, selective ionization also relaxes the need for mass

discrimination between the scattered reactants appearing at their parent mass and the radical product only one mass unit lower, allowing much greater quadrupole transmission and thus increased product signal. Finally, this selectivity is achieved without any prior spectroscopic knowledge about the products. Results below from the Chemical Dynamics Beamline for the reactions Cl + propane and Cl + pentane represent the first crossed molecular beam investigations of chemical reaction dynamics using tunable VUV synchrotron radiation to probe the scattered reaction products. Furthermore, these are the first detailed investigations of these metathesis reactions in which the *hydrocarbon radical* is detected, allowing the full picture of the reaction dynamics to emerge.

4.1 Crossed-beam reaction dynamics: Cl+Propane

The reaction of atomic chlorine with propane was studied at collision energies ranging from 8.0 kcal/mol to 31.6 kcal/mol. As mentioned above there are two different possible reactions depending on whether a primary or secondary hydrogen atom is abstracted, reactions 4.1.1 and 4.1.2.

$$C_3H_8 + Cl + HCl + n\text{-}C_3H_7 \rightarrow H_o = -2.0 \text{ kcal/mol} \qquad (4.1.1)$$

$$C_3H_8 + Cl + HCl + i\text{-}C_3H_7 \rightarrow H_o = -4.2 \text{ kcal/mol} \qquad (4.1.2)$$

These two pathways are illustrated both for the propane and pentane reaction in Fig. 36. The rate constant for this reaction has been reported at $(1.2\text{-}1.4)\times10^{-10}$ cm^3 $molecules^{-1}$ s^{-1}

and the temperature dependence over a range 220-600 K produced a very small activation energy of 40 K.

The Newton diagram for the reaction at 8.0 kcal/mol collision energy is shown in Fig. 37 along with the measured laboratory angular distribution for the propyl radical product. Fig. 38 shows a series of TOF spectra for the m/e 45 (propyl radical) product at numerous laboratory scattering angles, defined with respect to the propane beam. Angles scattered near the chlorine beam show a contribution from an effusive component, shown as a dashed line that is fitted separately. Both the measured angular distributions and TOF spectra are shown with the results of forward convolution simulations from which the center of mass distributions are obtained. These are summarized as the velocity-flux contour map shown in Fig. 39 for the 8.0 kcal/mol experiment. This contour map summarizes the dynamics inferred from the experiment. The angular distribution shows that the propyl radical product is scattered nearly isotropically, with some slight peaking in the forward direction. The velocity distribution is even more significant, however. The forward scattered product peaks strongly at the beam velocity itself, while the backscattered distribution peaks at somewhat slower velocities (lower recoil energies). This peaking at the beam velocity implies, since it is a light H atom that is transferred, that a stripping-type mechanism is likely responsible for the forward scattered product, as discussed below.

The lab angular distribution and corresponding Newton diagram for the experiment at a much higher collision energy, 31.6 kcal/mol, are shown in Fig. 40. The contour map derived from this experiment is shown in Fig. 41. Just as seen in the 8.0 kcal/mol result, the forward scattered distribution peaks at the propane beam, again

suggesting a stripping mechanism for this component. The broad backscattered distribution peaks at a somewhat lower recoil velocity, in addition to which a sideways scattered peak is observed.

Based on these measurements one can immediately eliminate the formation of a reaction complex with a lifetime comparable to or longer than its rotational period. The measured angular distributions do not exhibit the forward/backward symmetry associated with a long-lived complex and there is a clear coupling between the angular and translational energy distributions. The large partitioning of energy into translation is also inconsistent with a statistical partitioning of the available energy expected for decomposition of a long-lived reaction complex. All of these observations are consistent with a direct reaction mechanism, in agreement with the conclusions from previous investigations for H atom abstraction from saturated alkanes.

The measurements show near isotropic scattering at all measured collision energies with greater translational energy release for forward scattered products than sideways/backwards scattered products. At the higher collision energy, the difference in translational energy of the products is most apparent and suggests a separation of the scattering into two distinct reaction mechanisms. As mentioned above, the forward peaking at the beam velocity suggests a stripping mechanism for that component involving relatively large impact parameter collisions and no momentum transfer between the colliding species aside from that associated with the transfer of the H atom. This is consistent with *secondary* H abstraction, as no barrier is expected for this process. The backscattered contribution, however, shows evidence for involvement of the *primary* H atoms, since a modest barrier is anticipated for this channel. These likely arise from more

strongly coupled collisions, providing the necessary energy along the line of centers to overcome the barrier as suggested by Zare for the Cl-methane reaction. At the lower collision energy, 62% of the available energy appears in translation for the forward scattered product, while for the backscattered distribution, 53% of the available energy appears in translation. At the higher collision energy, this value is nearly unchanged for the backscattered component, while for the forward scattering the fraction increases from 62% to 74%, in effect directly tracking the collision energy. This shows coupling of the collision energy into internal degrees of freedom of the products for the backscattered distribution, again contrasting the close collisions responsible for that channel with the stripping contribution for the forward scattered product.

In addition to providing detailed insight into the dynamics of these H abstraction reactions, the use of tunable VUV probe allows for direct measurement of photoionization efficiency curves for these radicals, as shown in Fig. 42. This figure shows the PIE curve for the propyl radical from the reaction at 8.0 kcal mol and a Lab scattering angle of 10°. At this angle, the radical is known to be internally cold, so that this PIE spectrum accurately represents the threshold. This spectrum shows an ionization threshold of 7.5±0.3 eV, in good agreement with previously reported values for the isopropyl radical.

4.2 Cl + n-Pentane

The studies discussed above were recently extended to reaction of Cl with n-pentane, in an effort to examine the underlying trends in the reaction dynamics, in particular to probe the role of the extended carbon skeleton in these reactions.[42]

The reaction of chlorine atoms with n-pentane proceeds via either primary or secondary H atom abstraction:

$$Cl + n\text{-}C_5H_{12} \rightarrow HCl + H_2CH_2CH_2CH_2CH_2CH_3 \qquad (4.2.1)$$

$$Cl + n\text{-}C_5H_{12} \rightarrow HCl + H_3CHCH_2CH_2CH_2CH_3 \qquad (4.2.2)$$

$$Cl + n\text{-}C_5H_{12} \rightarrow HCl + H_3CH_2CHCH_2CH_2CH_3 \qquad (4.2.3)$$

Reactions 4.2.2 and 4.2.3 will be considered together since they both represent secondary H atom abstraction and are energetically indistinguishable. Fig. 36 shows the energetics of these reactions. Barriers for these two pathways are unknown, but rate constant measurements and analogy to smaller hydrocarbons suggest no barrier for the secondary H atom abstraction pathways (reactions 4.2.2 and 4.2.3), and a very small barrier for the primary abstraction channel (reaction 4.2.1).

The Newton diagram for the reaction is shown in Fig. 43, along with the measured laboratory angular distribution. The maximum available energy for the 2-pentyl radical product from this slightly exothermic reaction gives the recoil limit circle

indicated. Also shown in conjunction with the measured angular distribution is the simulated distribution resulting from the best fit to all of the data. The inherently coupled nature of the angular and energy distributions can be inferred directly from inspection of the angular distribution: the forward scattering extends beyond the beam in the forward direction, nearly to the recoil limit. The backscattered distribution, in contrast, drops sharply at a lab angle of 60°, well before the translational energy limit. This is confirmed by the time-of-flight distributions shown in Fig. 44. These distributions serve to constrain the simulations from which the translational energy and angular distributions are obtained.

Excellent fits were obtained simply by decomposing the center-of-mass distributions into two components shown in Fig 45. The first, shown as 'channel 1', is exclusively forward scattered, and shows a translational energy distribution peaking at the limit of the available energy. In contrast to channel 1, channel 2 shows a broad but predominantly backscattered distribution, with a vastly different translational energy release. The average energy release obtained for channel 1 is $\langle E \rangle_1 = 20.4$ kcal/mol, which is 92% of the available energy (E_{avail}), while for channel 2 it is $\langle E \rangle_2 = 7.7$ kcal/mol, which is 35% of E_{avail}. The branching fractions are 58% for channel 1 and 32% for channel 2.

As in any forward convolution simulation of crossed-molecular beam results, the fit obtained is not unique. However, the velocity-flux contour map obtained, shown in Fig. 46, faithfully reproduces the measured distributions. Nevertheless, for the forward-

scattered products in particular the decomposition into two components is somewhat arbitrary, and driven by the fit to the backscattered distribution.

The dynamics for the forward-scattered channel obtained from the fit are largely consistent with previous studies of Cl-hydrocarbon reaction dynamics. The P(E) peaks at the maximum energy available for formation of the isoenergetic 2-pentyl (butyl-1-methyl) or 3-pentyl (propyl-1-ethyl) radicals, with an average of only 1.8 kcal/mole remaining in rotation and vibration of the products. The bulk of the forward scattered distribution appears at translational energies exceeding the limit for formation of the 1-pentyl radical (see the limits in Figs. 45 and 46). Abstraction of primary H atoms is thus ruled out for channel 1; however, there is little here to suggest any different propensities for abstraction of the hydrogen atoms from the 2- or 3- carbons.

The results for this channel are reminiscent of those reported by Flynn et al. for the Cl-cyclohexane[43] reaction, and identified by others in propane[38,39,44] and even for vibrationally excited methane[33-36]. That is, the products are formed with very little internal energy. As mentioned above, many have attributed this to a collinear transition state; yet the correlation between forward scattering and a collinear transition state is problematic. Zare and coworkers considered several possible mechanisms that could reconcile these, but finally suggested an alternative interpretation of the dynamics.[33] They argued that if the reaction is not in the impulsive limit, then a cold product rotational distribution need not imply a collinear transition state.

The dynamics for channel 2, the backscattered distribution, diverge dramatically from previous work on H abstraction dynamics in hydrocarbons, even differing significantly from the above studies of the analogous Cl-propane reaction. The P(E) for

channel 2 peaks at 6.8 kcal/mol, with an average release of 7.7 kcal/mol, a fractional energy release of only 35%. This may be compared to results for Cl-propane, for which the fractional energy release for the backscattered component ranged from 52% at 11.5 kcal/mol collision energy to 48% at the highest 31 kcal/mol collision energy. This means that an average of 15 kcal/mol remains in internal degrees of freedom of the products. State-resolved studies for propane have shown only a small yield of vibrationally excited HCl product[38,39], so it is unlikely that this accounts for much of the energy. Furthermore, little difference is expected between the HCl energy content from propane or pentane, since the energetics are virtually the same for both reactants. The likely repository of the bulk of this energy is thus in the hydrocarbon fragment; the question is whether it is in rotation or vibration. One significant difference between n-pentane and propane is the average impact parameter: the long n-pentane molecule naturally will yield abstraction of primary H atoms a considerable distance from the center of mass of the molecule. One might expect this to lead to greater rotational excitation for the pentane case. However, these large impact parameter (b) collisions will also yield fairly large exit impact parameters (b') so that little of the necessary conversion of orbital to rotational angular momentum may occur. Large rotational excitation in general requires small impact parameters for effective coupling of the initial linear momentum into rotational excitation. It is only for these close collisions that the required large value of (b-b') can occur. Some measure of enhanced rotational excitation is plausible in the case of n-pentane, but for this to account for an increase to 65% of the available energy seems unlikely.

On the other hand, plausible reasons for greater vibrational excitation in the case of pentane vs. propane are readily apparent. There are many more vibrational modes for n-pentane (45 vs. 27), and perhaps more significantly, many more involving the low-frequency C-C-C bends. For these modes, with vibrational frequencies on the order of 800 cm^{-1}, the half-period is roughly 20 fs. We can compare this to the collision time under the conditions of the experiment: for an effective interaction region of 0.05nm at 2400 m/s we estimate a collision time of 21 fs, a very good match to the vibrational period. The combination of the higher density of states and the excellent match between the collision time and the bending mode vibrational period greatly favors coupling between the collision energy and the internal modes of the hydrocarbon. This suggests that in pentane one is seeing the direct participation of the extended carbon backbone in the reaction.

A final question concerns the nature of the two different channels. In the work on the propane reaction mentioned above, the forward-scattered distribution was associated with the abstraction of secondary H atoms, while the backscattered product was associated with primary H atoms. It is even clearer in the pentane case, since the bulk of the forward scattered products are formed at translational energies well exceeding that possible for production of the 1-pentyl radicals, that the forward scattered products are indeed the result of secondary H atom abstraction. The question remains for the backscattered products: Are they preferentially associated with primary H abstraction? Although there is no direct evidence indicating a connection between the predominantly backscattered 'channel 2' and the primary abstraction channel, reaction 1, several lines of evidence point this direction. First, the maximum energy release shown in Fig. 45, and

apparent in the contour map in Fig. 46, extends precisely to the limit of the available energy for production of the higher energy isomer. This distribution came directly from the best fit to the laboratory data and was in no way enforced. Secondly, there is the total branching between forward and backward scattered products. For the propane reaction, the fraction scattered forward of 90° was very close to 50% of the total. Assuming simply a limiting case association of forward scattering with secondary H abstraction implies three times higher reactivity of the secondary vs. primary H atoms. For pentane, then, one should expect the fraction forward scattered to increase from 1/2 to 3/4, since there are three times the number of secondary H. Indeed, considering only the fraction of the total scattered in the forward direction, in the same way the propane was treated, we find a value of 74%, a remarkable agreement. Comparing the fraction of the total scattered into 'channel 1' the value is 64%. If we make the association between channel 1 and secondary H abstraction, and channel 2 and primary H abstraction, this implies roughly a 1.8-fold higher reactivity of the secondary H atoms. However, this cannot be directly compared to the propane results since the distributions were decomposed differently. These values, on the order of 2- to 3-fold higher reactivity of secondary vs. primary H atoms, are consistent with those reported by Koplitz et al.[45] as well as Varley and Dagdigian[39] for selectively deuterated propane.

These translational energy distributions argue for a bit of caution on the part of those employing the 'photoloc' technique and other methods relying on state-resolved measurements of one of the fragments to extract the speed and angular distributions for the reaction. These studies are generally blind to internal energy in the undetected

fragment. Moreover, the reconstruction of the product distributions requires some assumptions about the unmeasured fragment. If these assumptions are in error, then the derived distributions are inaccurate. Usually the assumption is made that the undetected fragment is internally cold, although in at least one case this issue was considered explicitly.[38] As we have seen, for the forward scattered products in the pentane and propane case, this is a fairly accurate assumption. For the backscattered distributions, however, this is grossly incorrect.

5.0 Conclusion

The studies detailed above illustrate the broad range of new possibilities for chemical dynamics studies made possible by application of intense, tunable VUV light from third-generation synchrotron sources. Application in photodissociation studies have shown that advantages of a probe that is at once *selective* and *universal* for unraveling complex dynamics in challenging systems. Crossed-beam studies show the power of a very low-background, universal probe to yield a global view of the detailed dynamics for reactions involving challenging hydrocarbon systems. Exciting new possibilities are in the offing as ion imaging methods are adapted to chemical dynamics studies using synchrotron radiation in the near future.

Acknowledgments.

This work represents contributions of a great many people. Particular thanks go to Dr. Xueming Yang, Dr. David Blank, Dr. Philip Heimann, Dr. Yuan T. Lee and to the ALS

staff. This work was supported by the Director, Office of Energy Research, Office of Basic Energy Sciences, Chemical Sciences Division of the US Department of Energy under contract No. DE-AC03-76SF00098.

References

[1] Y. T. Lee, *Science*. **236**, 795 (1987).
[2] Y. T. Lee, J. D. McDonald, P. R. LeBreton and D. R. Hershback, *Rev. Sci. Instrum.* **40**, 1402 (1969).
[3] P.A. Heimann, M. Koike, C. Hsu, M.D. Evans, K. Lu, C.Y. Ng, A.G. Suits, and Y.T. Lee, *Rev. Sci. Instrum*, **68**, 1945, (1997).
[4] X. Yang, J. Lin, Y.T. Lee, D.A. Blank, A.g. Suits, A.M. Wodtke, *Rev. Sci. Instrum.* **68**, 3317 (1997).
[5] A. M. Wodke and Y. T. Lee, *J. Phys. Chem.* **89**, 4744 (1985)
[6] D. Stranges, X. Yang, J.D. Chesko, A.G. Suits, *J. Chem. Phys.* **102** (15) 6067 (1995).
[7] D.A. Blank, S.W. North, D. Stranges, A.G. Suits, Y.T. Lee, *J. Chem. Phys.*, **106** (2) 539 (1997).
[8] X. Chen, F. Asmar, H. Wang and B.R. Weiner, *J. Phys. Chem., 95,* 6415 (1991); X. Chen, H. Wnag, B.R. Weiner, M. Hawley, and H.H. Nelson, *ibid.* **97**, 12269 (1993).
[9] D.A. Blank, A. G. Suits, and Y. T. Lee, *J. Chem. Phys.* **108**, 5784 (1998); D.A. Blank, W. Sun, A. G. Suits, Y. T. Lee, S. W. North, and G. E. Hall, *J. Chem. Phys.*, in press.
[10] M. J. Berry, *J. Chem. Phys.* **61**, 3114 (1974); M. J. Molina and G. C. Pimentel, *J. Chem. Phys.* **56**, 3988 (1972).
[11] M. G. Moss, M. D. Ensminger, and J. D. McDonald, *J. Chem. Phys.* **74**, 6631 (1981).
[12] D. J. Donalson and S. R. Leone, *Chem. Phys. Lett.* **132**, 240 (1986).
[13] M. Umemoto, K. Seki, H. Shinohara, U. Nagashima, N. Nishi, M. Kinoshita, and R. Shimada, *J. Chem. Phys.* **83**, 1857 (1985).
[14] P. T. A. Reilly, Y. Xie, and R. J. Gordon, *Chem. Phys. Lett.* **178**, 511 (1991).
[15] Y. Mo, K. Tonokura, U. Matsumi, M. Kawasaki, T. Sato, T. Arikawa, P.T.A. Reilly, Y. Xie, Y. Yang, Y. Huang, and R. J. Gordon, *J. Chem. Phys.* **97**, 4815 (1992).
[16] G. He, Y. Yang, and R. J. Gordon, *J. Phys. Chem.* **97**, 2186 (1993).
[17] Y. Huang, Y. Yang, G. He, and R. J. Gordon, *J. Chem. Phys.* **99**, 2752 (1993).
[18] Y. Huang, G. He, Y. Yang, S. Hashimoto, and R. J. Gordon, *Chem. Phys. Lett.* **229**, 621 (1994).
[19] Y. Huang, Y. Yang, G. He, S. Hashimoto, and R. J. Gordon, *J. Chem. Phys.* **103**, 5476 (1995).
[20] K. Sato, Y. Shihirs, S. Tsunashima, H. Umemoto, T. Takayanagi, K. Furukawa, and S. Ohno, *J. Chem. Phys. 99,* 1703 (1993).
[21] Y. Mo, K. Tonokura, U. Matsumi, M. Kawasaki, T. Sato, T. Arikawa, P.T. Areilly, Y, Xie, Y. Yang, Y. Huang, and R. J. Gordon, *J. Chem. Phys.* **97**, 4815 (1992).
[22] M. Umemoto, K. Seki. H. Shinohara, U. Hagashima, N. Nishi, M. Kinoshita, and R. Shimada, *J. Chem. Phys.* **83**, 1857 (1985).
[23] P. Andresen and A. C. Luntz, *J. Chem. Phys.* **72**, 5842 (1980), A. C. Luntz and P. Andresen, *J. Chem. Phys.*, **72**, 5851 (1980).
[24] N. Hemmi and A. G. Suits, *J. Phys. Chem. A.* **101**, 6633 (1997).
[25] M. Ahmed, D. Blunt, D. Chen, and A.G. Suits, *J. Chem. Phys.* **106**, 7617 (1997).
[26] K. P. Lim and J. V. Michael, *J. Phys. Chem.* **98**, 211 (1994).
[27] W. Sun, K. Yokoyama, J. C. Robinson, A. G. Suits, and D. M. Neumark, *J. Chem. Phys.*, (in press).
[28] D. A. Ramsay and P. Thistlethwaite, *Can. J. Phys.* **44**, 1381 (1966).
[29] S. Satyapal and R. Bersoh, *J. Phys. Chem.* **95**, 8004 (1991); K. Seki and H. Okabe, *J. Phys. Chem.* **96**, 3345 (1992).
[30] L. Vereecken, K. Pierloot, and J. Perters, *J. Chem. Phys.* **108**, 1068 (1998).
[31] W. Bartok and A. F. Sarofim, *Fossil Fuel Combustion.* 88 (Wiley-Interscience, New York 1991).
[32] P. Andresen and A. C. Luntz, *J. Chem. Phys.* **72**, 5842 (1980), A. C. Luntz and P. Andresen, *J. Chem. Phys.*, **72**, 5851 (1980).
[33] W. R. Simpson, A. J. Orr-Ewing, and R. N. Zare, *Chem. Phys. Lett.*, **212**, 163 (1993).
[34] W. R. Simpson, T. P. Rakitzis, S. A. Kandel, A. J. Orr-Ewing and R. N. Zare, *J. Chem. Phys.*, **103**, 7313 (1995).
[35] W. R. Simpson, T. P. Rakitzis, S. A. Kandel, T. Lev-On, and R. N. Zare, *J. Phys. Chem.*, **100**, 7938 (1996).
[36] S. A. Kandel, T. P. Rakitzis , T. Lev-On, and R. N. Zare, *J. Chem. Phys.*, **105**, 7550 (1996).
[37] D. F. Varley and P. J. Dagdigian, *J. Phys. Chem.*, **99**, 9843 (1995).

[38] D. F. Varley and P. J. Dagdigian, *J. Phys. Chem.*, **100**, 4365 (1996).
[39] D. F. Varley and P. J. Dagdigian, *Chem. Phys. Lett.*, **255**, 393 (1996).
[40] Y. T. Lee, J. D. McDonald, P. R. LeBreton and D. R. Hershback, *Rev. Sci Instrum.* **40**, 1402 (1969).
[41] Y. T. Lee, *Science* **236**, 793 (1987).
[42] N. Hemmi and A. G. Suits, *J. Chem. Phys.* **109**, 5338 (1998).
[43] J. Park, Y. Lee, J. F. Hershberger, J. M. Hossenlopp, and G. W. Flynn, *J. Am. Chem. Soc.* **114**, 58 (1990).
[44] D. F. Varley and P. J. Dagdigian, *J. Phys. Chem.* **99**, 9843 (1995).
[45] Y. Fen, Z. Wang, B. Xue, and B. Koplitz, *J. Phys. Chem.* **98**, 4 (1994).

Figure Captions

FIG. 1. Schematic diagram of the universal crossed molecular beams apparatus with synchrotron photoionization product detection (Endstation 1).

Fig. 2. Time-of-flight (TOF) spectra of photodissociation products of methylamine ($CH_3NH_2 \rightarrow CH_3 + NH_2$) at 193 nm: The upper trace shows the TOF spectrum for the CH_3 radical detected at m/z = 15; the bottom trace results from the NH_2 radical, detected at m/z =16. There is no evidence of the much more likely H-atom loss channels because dissociative ionization of the CH_2NH_2 or CH_3NH radicals is suppressed by use of photoionization. Note that detection of reaction products at m/z = 15 and 16 is easily accomplished despite the large residual CH_4 background.

Fig. 3. Time of flight spectra of m/e=32 from ozone photodissociation at 193 nm detected at Θ=20°. Upper: ionization energy 17eV, middle: 13.5eV, lower: 10.5 eV. TOF peaks are labeled consistent with results from Ref. 2.[i]

Fig. 4. TOF spectra for m/e 66 (CD_3SO^+) at source angles of 12° and 22.5°. The forward convolution fit contains two contributions representing the fast and slow channels for reaction discussed in the text and fitted with the $P(E_T)$s in Fig. 5.

Fig. 5. The center of mass translational energy distribution used to fit the sulfonyl radicals in Fig. 4, showing fast and slow contributions ascribed to dissociation on excited and ground state potential surfaces, respectively.

Fig. 6. The TOF spectra for CD_3^+ at the indicated angles, showing three contributions as described in the text.

Fig. 7. The center of mass translational energy distributions derived from fitting both primary methyl and sulfonyl radical products. The shaded area is the difference between fits to the methyl and sulfonyl contributions, and represents the primary c.m. translation energy distribution for sulfonyl intermediates that undergo secondary C-S bond cleavage.

Fig. 8. A summary of the dissociation channels observed of DMSO following absorption at 193 nm.

Fig. 9. TOF spectra for m/e 52 (C_3H_2N+) photoproducts at source angles of 5° and 7.5°and a photoionization energy of 14.0 eV. The solid line is the forward convolution fit using the $P(E_T)$ shown in Fig. 10.

Fig. 10. The solid line is the $P(E_T)$ used to fit the TOF spectra in Fig. 9 for hydrogen atom elimination. $C_3H_3N \rightarrow H + C_3H_2N$. The dotted line is the calculated prior distribution given an available energy of 40 kcal/mol for comparison.

Fig. 11. The circles are the photoionization spectrum for the m/e 52 (C_3H_2N+) photoproducts from hydrogen atom elimination. $C_3H_3N \rightarrow H + C_3H_2N^+$, at a source angle of 7.5°. The triangles are the photoionization spectrum for the m/e 51 (C_3HN^+) photoproducts from molecular hydrogen elimination, $C_3H_3N \rightarrow H_2 + C_3HN$, at a source angle of 10°.

Fig. 12. TOF spectra for m/e 51 (C_3HN) photoproducts at the indicated scattering angle and probe photon energy. The dotted line representing the larger contribution to the fits is the forward convolution fit using the *P(E$_T$)* shown in Fig. 13. The solid line is the total forward convolution fit to the data.

Fig. 13. The *P(E$_T$)* for molecular hydrogen elimination, $C_3H_3N \rightarrow H_2 + C_3HN$, used for the forward convolution fits to the TOF spectra in Fig. 12. The two curves show the range of the uncertainty in the *P(E$_T$)*. Within this region we are able to obtain a satisfactory forward convolution fit to the TOF spectra in Fig. 12.

Fig. 14. The photoionization spectrum for m/e 27 photoproducts at a source angle of 15°. The major component with an onset ~ 11 eV is from HCN photoproducts, $C_3H_3N \rightarrow HCN + C_2H_2$, and the small shoulder with an onset at 8.5 eV is from vinyl radical photoproducts generated by CN elimination, $C_3H_3N \rightarrow CN + C_2H_3$.

Fig. 15. TOF spectra for m/e 27 photoproducts at a source angle of 20° and photoionization energies of 10.0 eV, solid line, and 15.0 eV, dashed line. The TOF spectrum at 10.0 eV represents vinyl radical products from CN elimination and the spectrum at 15.0 eV is dominated by HCN photoproducts; see text. The two TOF spectra have been independently scaled; however the TOF spectrum at 10.0 eV has a corrected signal intensity <1% of the TOF spectrum at 15.0 eV.

Fig. 16. The circles are the photoionization spectrum for m/e 26 photoproducts at a source angle or 15°. The triangles are the photoionization spectrum for a jet-cooled molecular beam of acetylene.

Fig. 17. Thermodynamically available molecular dissociation channels for vinyl chloride following absorption at 193 nm

Fig. 18. Thermodynamically available radical dissociation channels for vinyl chloride following absorption at 193 nm. Barriers connecting $ClCCH_2$ with ClHCCH and with Cl+HCCH illustrate hypotheses consistent with present results.

Fig. 19. $P(E_T)$ used to fit the TOF spectra for the H elimination channel. Dotted lines represent uncertainty in the truncation.

Fig. 20. TOF spectra for m/e 60 (C_2HCl^+) photoproducts at the indicated scattering angle and photoionization energy of 12.0 eV. The dominant component in the forward

convolution fits is from H_2 elimination, $H_2CCHCl \rightarrow H_2 + HCCCl$, and was fitted with the $P(E_T)$ shown in Fig. 21. The minor component in the 10° spectrum is from dissociative ionization of C_2H_2Cl photoproducts and was fitted with the $P(E_T)$ shown in Fig. 19.

Fig. 21. $P(E_T)$ for H_2 elimination, $H_2CCHCl \rightarrow H_2 + HCCCl$, used to fit the TOF spectra shown in figure 20.

Fig. 22. TOF spectra for m/e 36 (HCl^+) photoproducts at the indicated scattering angles and a photoionization energy of 12.0 eV.

Fig. 23. $P(E_T)$ for HCl elimination, $H_2CCHCl \rightarrow HCl + C_2H_2$, used to fit the TOF spectra shown in Figure 22.

Fig. 24. PIE spectrum for m/e 36 (HCl^+) photoproduct at a scattering angle of 20.

Fig. 25. TOF spectra for m/e 27 (C_2H_3+) photoproducts at scattering angles of 15°and 25° and a photoionization energy of 11.0 eV. The forward convolution fits to the spectra were done using the $P(E_T)$ in figure 24.

Fig. 26. $P(E_T)$ for C-Cl bond cleavage, $H_2CCHCl \rightarrow Cl + C_2H_3$, on the excited electronic state used in the forward convolution fitting in Figs. 25 and 27.

Fig. 27. TOF spectra for m/e 35 (Cl^+) photoproducts at the indicated scattering angles and a photoionization energy of 14.0 eV. The forward convolution fit to the spectra used the $P(E_T)$ in figure 26 for the fast component and figure 28 for the slow component.

Fig. 28. Translational energy distribution for the slow Cl photoproducts. The forward convolution fit to the TOF data in figure 27 is the dashed line representing the component from ~60-200 μsecs. Note that this is the translational energy distribution for Cl fragments alone and not the *total* c.m. translational energy distribution.

Fig. 29. PIE spectrum for the vinyl radical (m/e 27, $C_2H_3^+$) and scattering angle of 20.

Fig. 30. TOF spectra of *m/e* 28 (CO^+) at laboratory angles of 25 and 40° with photoionization energy of 14.5 eV. Circles represent the data, and lines are the forward convolution fits using the *P(E)* in Figure 31A.

Fig. 31. TOF spectra of *m/e* 35 (Cl^+) at laboratory angles of 15 and 40° with photoionization energy of 14.0 eV. Circles represent the data, and lines are the forward convolution fits using the *P(E)* in Figure 29B.

Fig. 32. Center-of-mass translational energy distribution A) for *m/e* 28 (CO^+), B) *m/e* 35 (Cl^+), and C) for *m/e* 63 ($ClCO^+$). Dashed lines represent the slow components, dotted-dashed lines are the fast contribution, and the solid line is the sum of these.

Fig. 33. $P(E_T)$ distributions of C_3H_3 + H from propyne (a) and allene (b) photodissociation.

Fig. 34. PIE curves of C_3H_3 product at $\Xi = 10°$ and 15° from photodissociation of propyne (a) and from allene photodissociation at $\Xi = 7°$ (b).

Fig. 35. Photoionization efficiency curves of C3H2 from (a) propyne and (b) allene dissociation.

Fig. 36. Schematic energy diagrams for reaction of Cl with propane and n-pentane.

Fig. 37. Laboratory angular distribution for C_3H_7 products and Newton diagram for the reaction Cl + propane at a collision energy of 8.0 kcal/mol. The solid line is the forward convolution fit and the circles are the data.

Fig. 38. TOF spectra for C_3H_7 at indicated laboratory angles for a collision energy of 8.0 kcal/mol. Circles are the data, solid line is the forward convolution fit, dash-dot-dash line is the forward convolution fit for the effusive component (see text) and the dashed line is the total fit to the data.

Fig. 39. Center of mass velocity-flux contour map for a propyl radical product from Cl + propane reaction at a collision energy of 8.0 kcal/mol.

Fig. 40. Laboratory angular distribution for C_3H_7 products and Newton diagram for Cl + propane reaction at a collision energy of 31.6 kcal.mol. The solid line is the forward convolution fit and the circles are the data.

Fig. 41 CM velocity-flux contour map for propyl radical product from Cl + propane reaction a collision energy of 31.6 kcal/mol.

Fig. 42 PIE spectrum for propyl radical product at a scattering angle of 10° and a collision energy of 8.0 kcal/mol.

Fig. 43. Laboratory angular distribution for C_5H_{11} product (top) and Newton diagram (bottom) for the reaction Cl + n-pentane. The circle on the Newton diagram represents maximum recoil limit for production of 2- or 3-pentyl radicals. Circles on the angular distribution are experimental data, open triangles are the best-fit simulations. The connecting line is included to guide the eye.

Fig. 44 TOF spectra at the indicated angles for pentyl radical product from reaction Cl + n-pentane at a collision energy of 16.8 kcal/mol.

Fig. 45. Center-of-mass angular (A) and translational energy (B) distributions obtained from the fit to the TOF spectra and the angular distribution data in Fig. 43. Arrows mark translational energy limits for production of indicated product isomers.

Fig. 46. Velocity-flux contour map for the pentyl radical from the reaction Cl + n-pentane at a collision energy of 16.8 kcal/mol. Inner circle shows recoil velocity limit for the 1-pentyl radical; outer circle indicates corresponding limit for 2- or 3-pentyl radicals. The contour line spacing is twice as dense for the lowest 25% of the distribution to reveal the channel 2 contribution more clearly.

---

[i] D. Stranges, X. Yang, J.D. Chesko, and A.G. Suits, *J. Chem. Phys.* **102** (15) 6067 (1995).

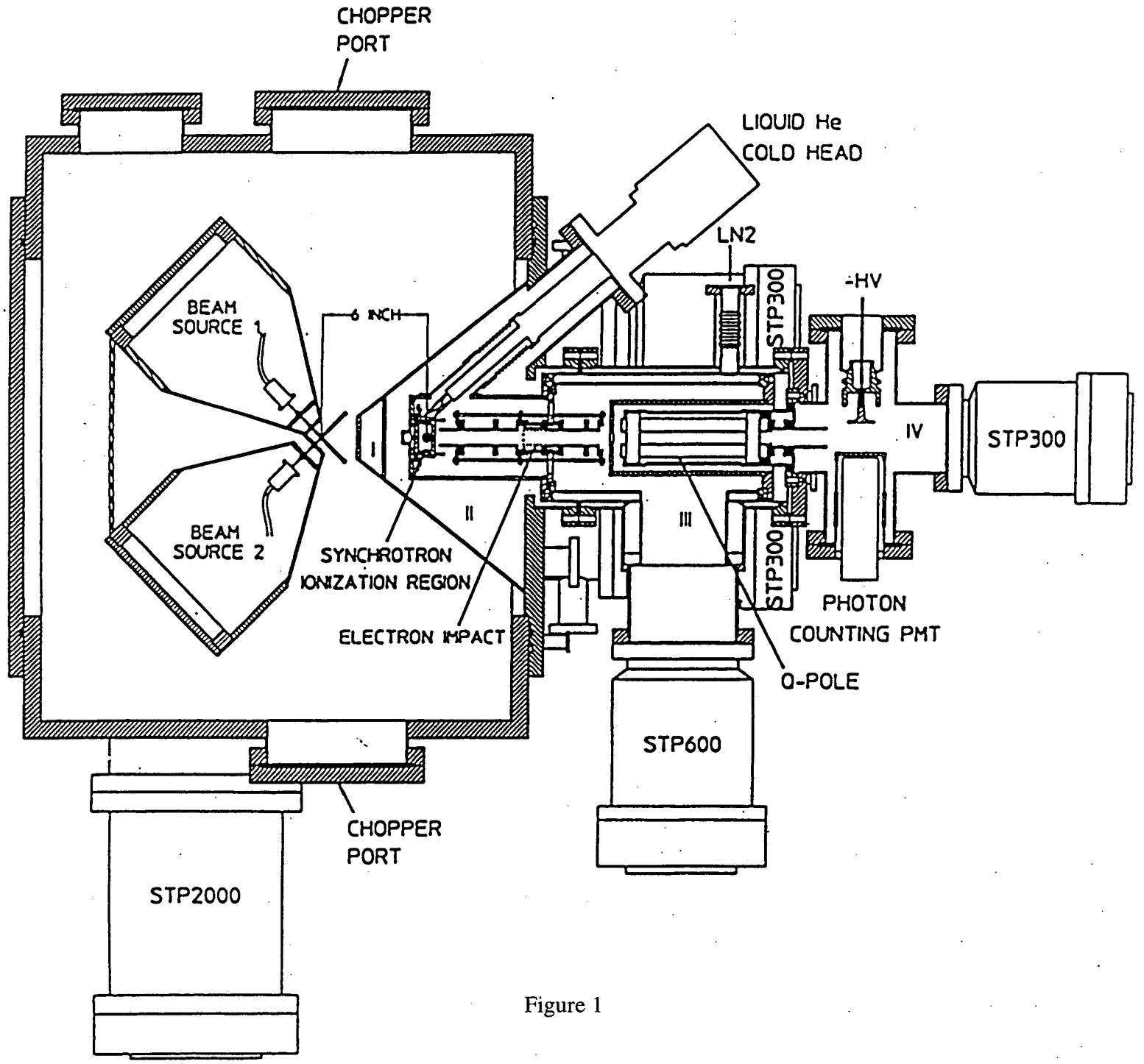
CHOPPER
PORT
LIQUID He
COLD HEAD
LN2
STP300
-HV
BEAM
SOURCE 1
6 INCH
I
IV
STP300
BEAM
SOURCE 2
II
III
STP300
SYNCHROTRON
IONIZATION REGION
PHOTON
COUNTING PMT
ELECTRON IMPACT
Q-POLE
STP600
CHOPPER
PORT
STP2000

Figure 1

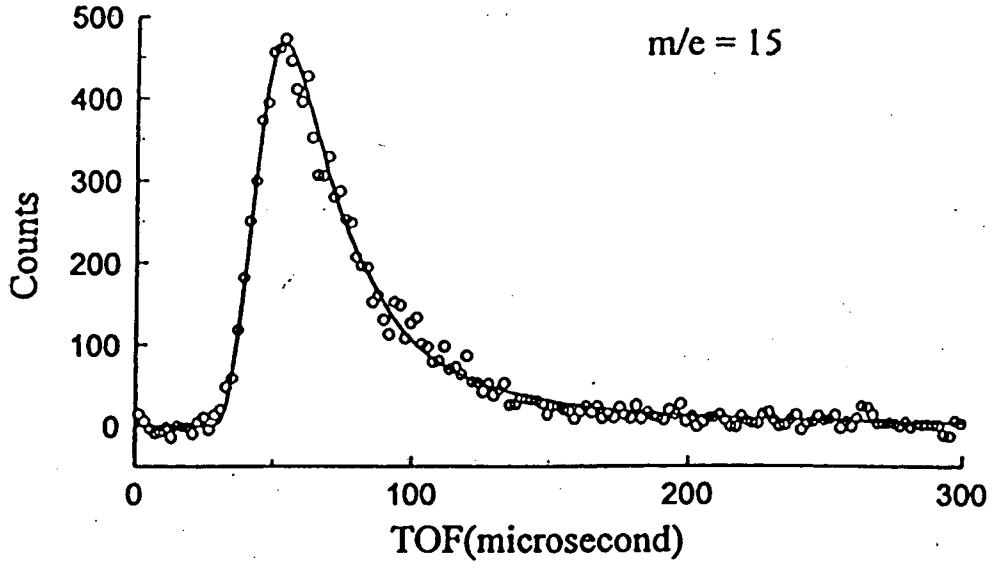
m/e = 15
Counts
500
400
300
200
100
0
0
100
200
300
TOF(microsecond)

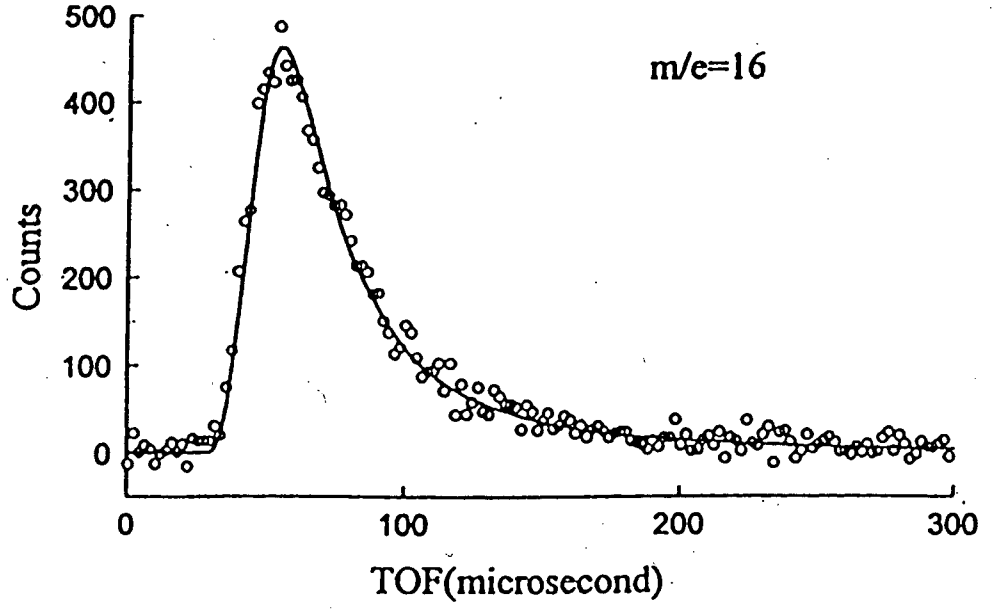
m/e=16
Counts
500
400
300
200
100
0
0
100
200
300
TOF(microsecond)

Figure 2

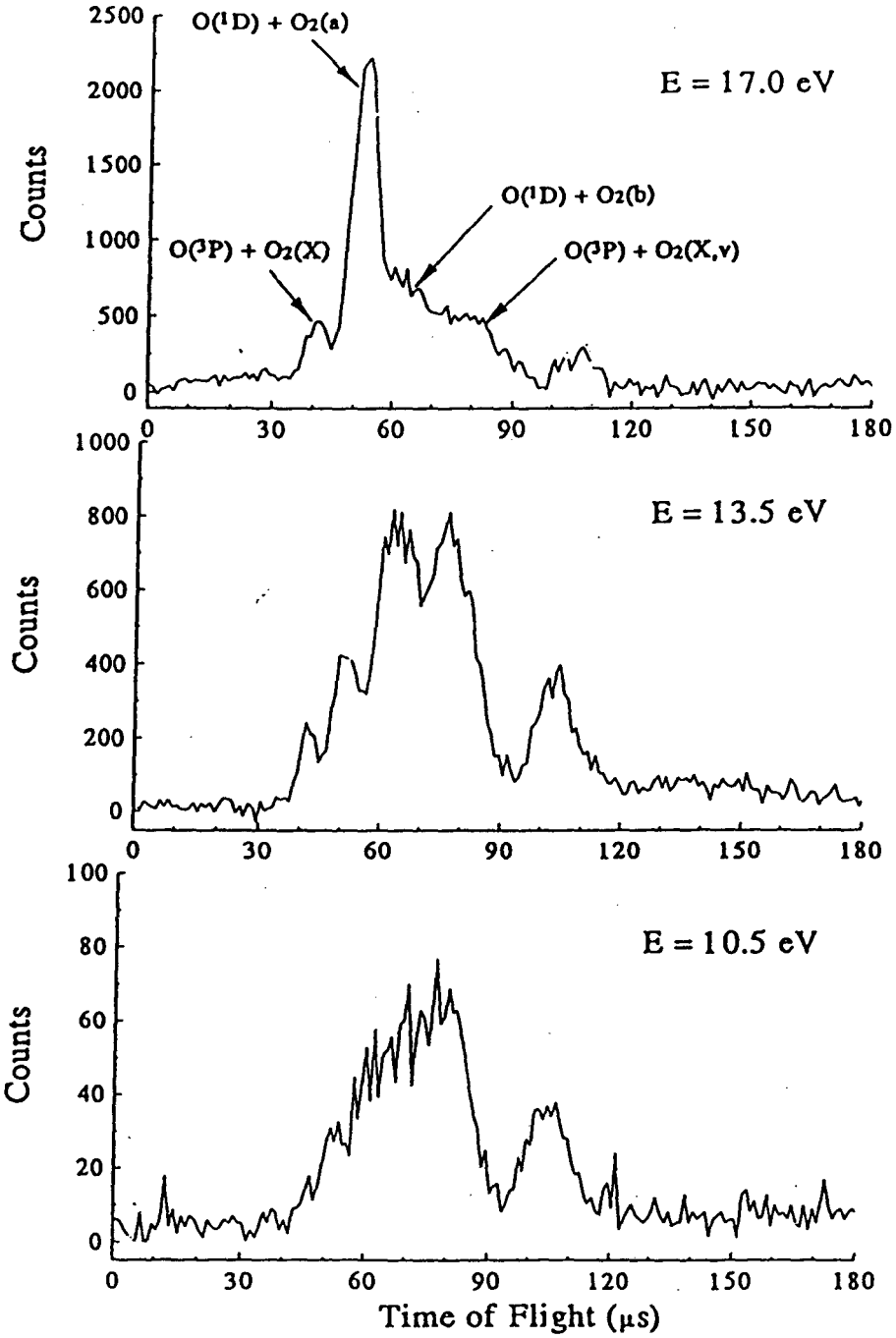
O(1D) + O2(a)
E = 17.0 eV
O(1D) + O2(b)
O(3P) + O2(X)
O(3P) + O2(X,v)
Counts
E = 13.5 eV
Counts
E = 10.5 eV
Counts
Time of Flight (μs)

Figure 3

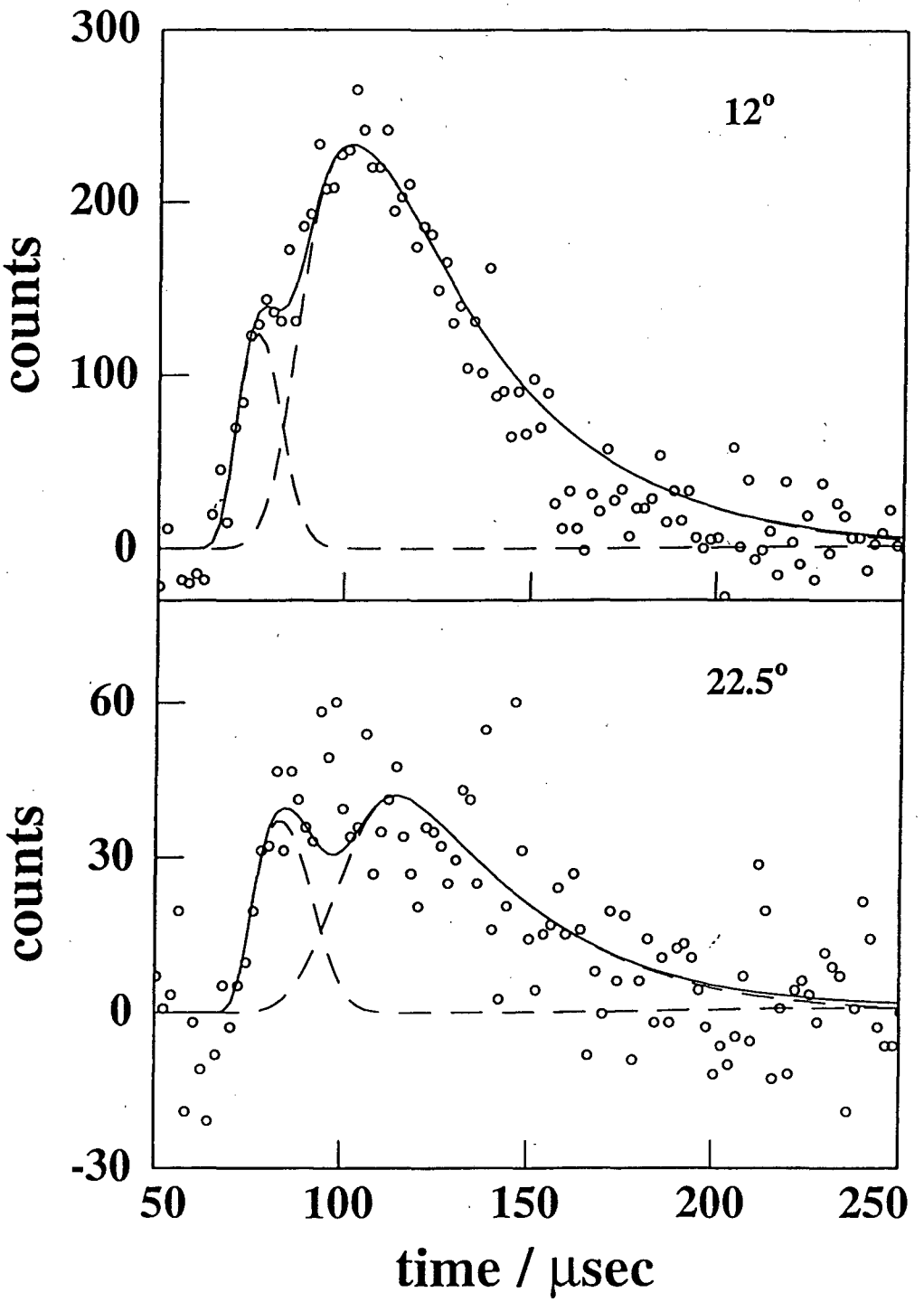
300
200
100
0
counts
12°
60
30
0
-30
counts
22.5°
50
100
150
200
250
time / μsec

Figure 4

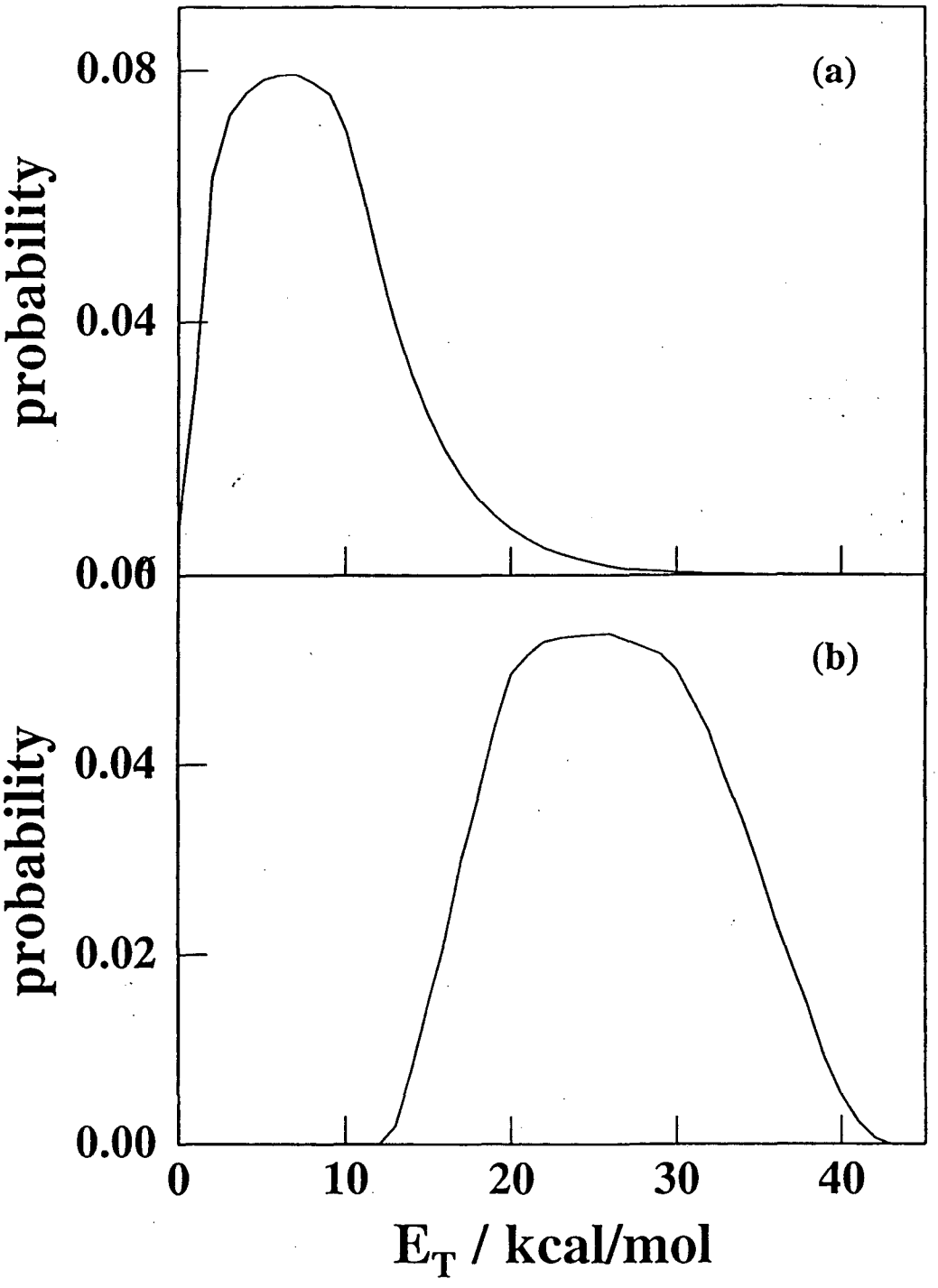
0.08
0.04
0.00
probability
(a)
0.04
0.02
0.00
probability
(b)
0
10
20
30
40
E_T / kcal/mol

Figure 5

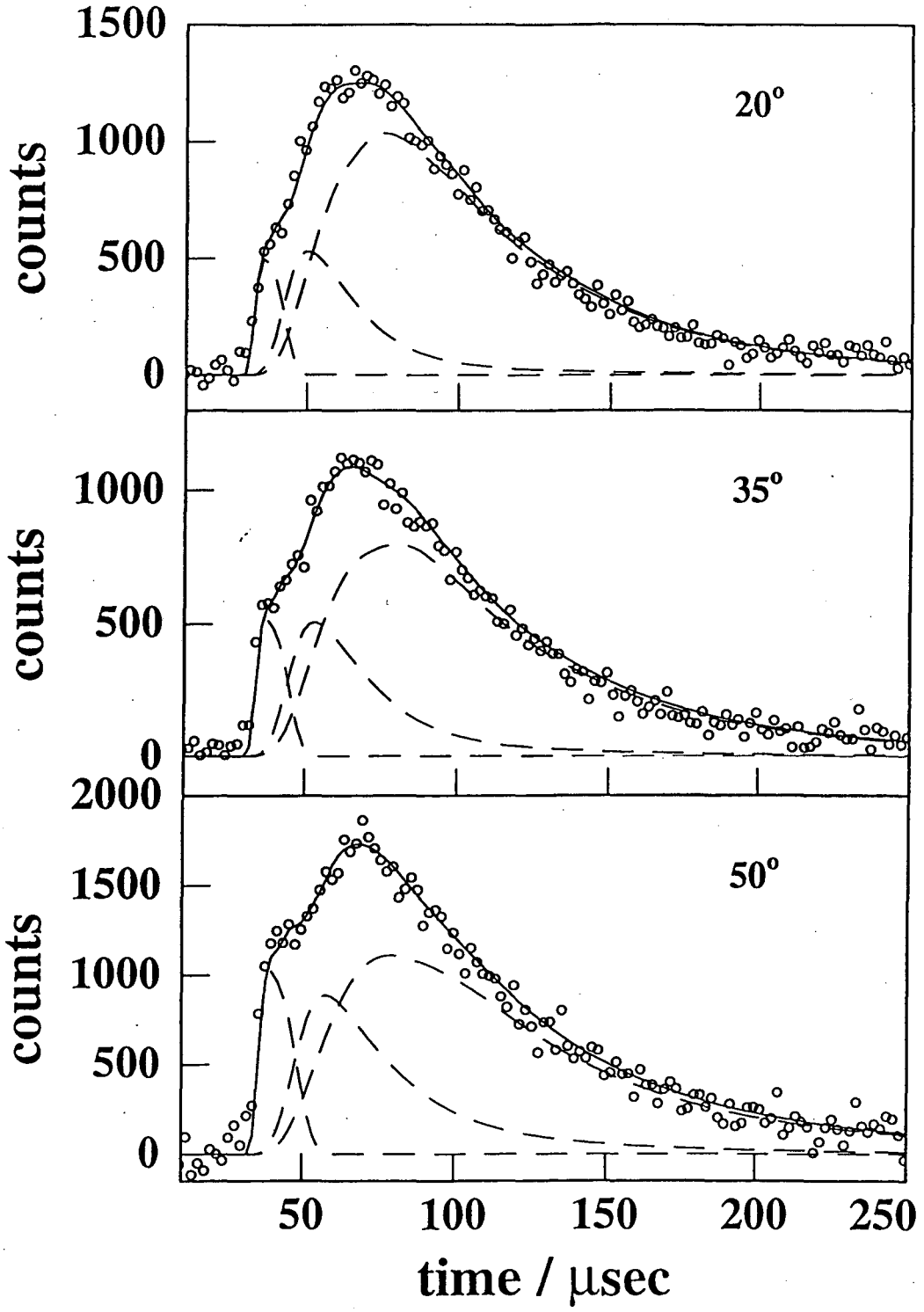
1500
1000
500
0
counts
20°
1000
500
0
counts
35°
2000
1500
1000
500
0
counts
50°
50
100
150
200
250
time / μsec

Figure 6

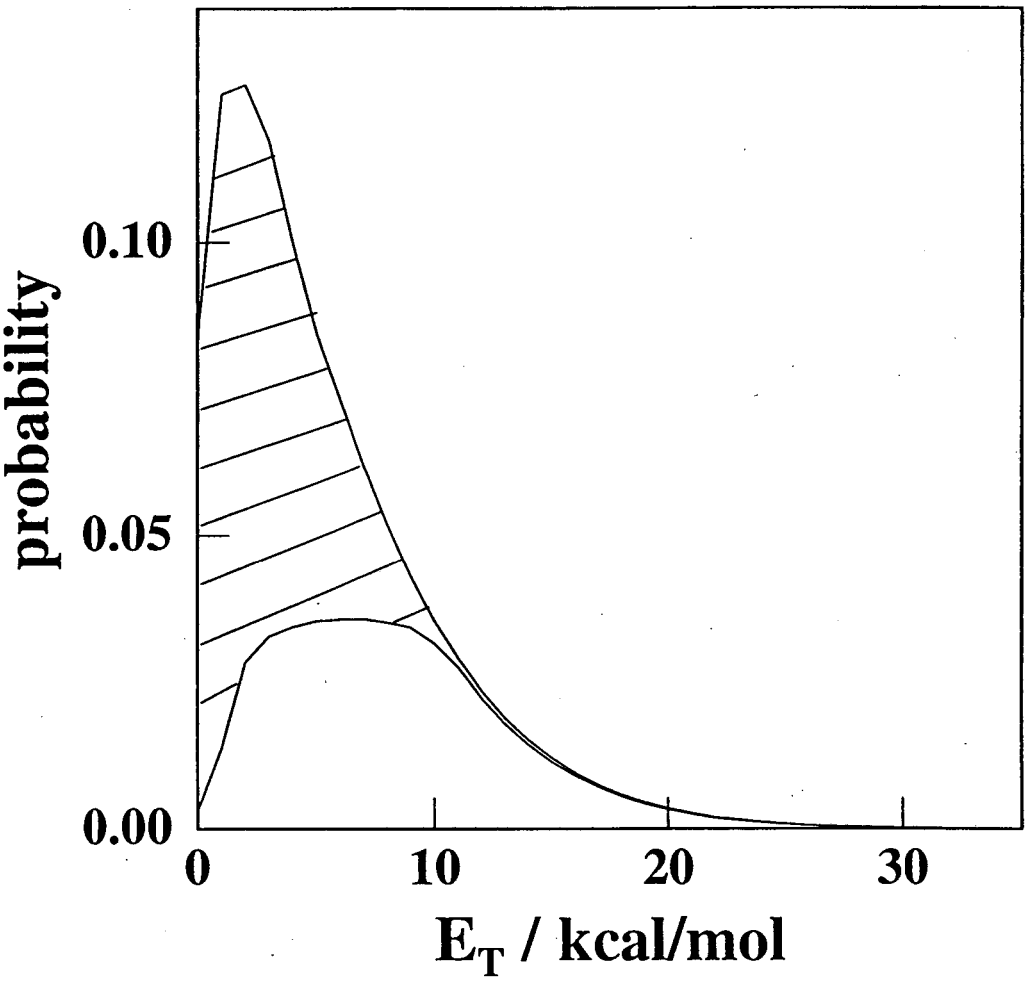

Figure 7

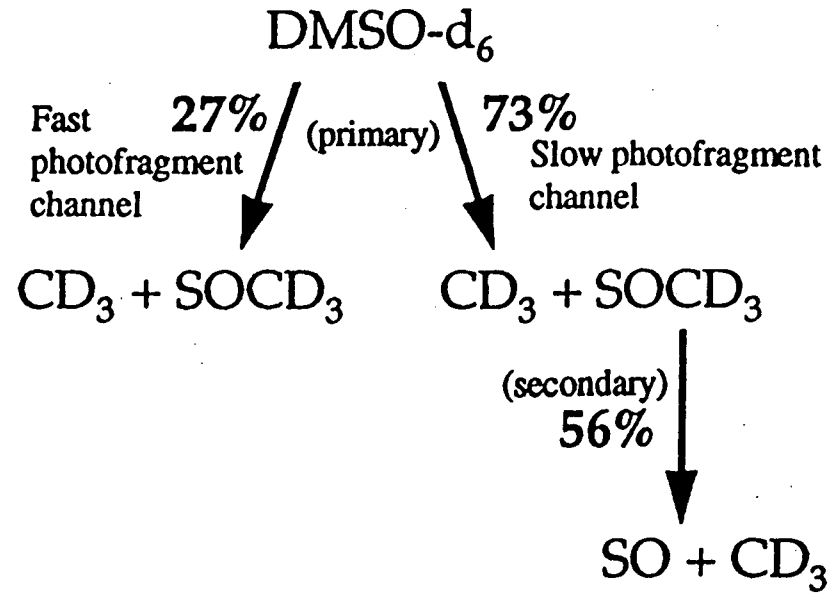
DMSO-d_6
Fast photofragment channel
27%
(primary)
73%
Slow photofragment channel
$CD_3 + SOCD_3$
$CD_3 + SOCD_3$
(secondary)
56%
$SO + CD_3$

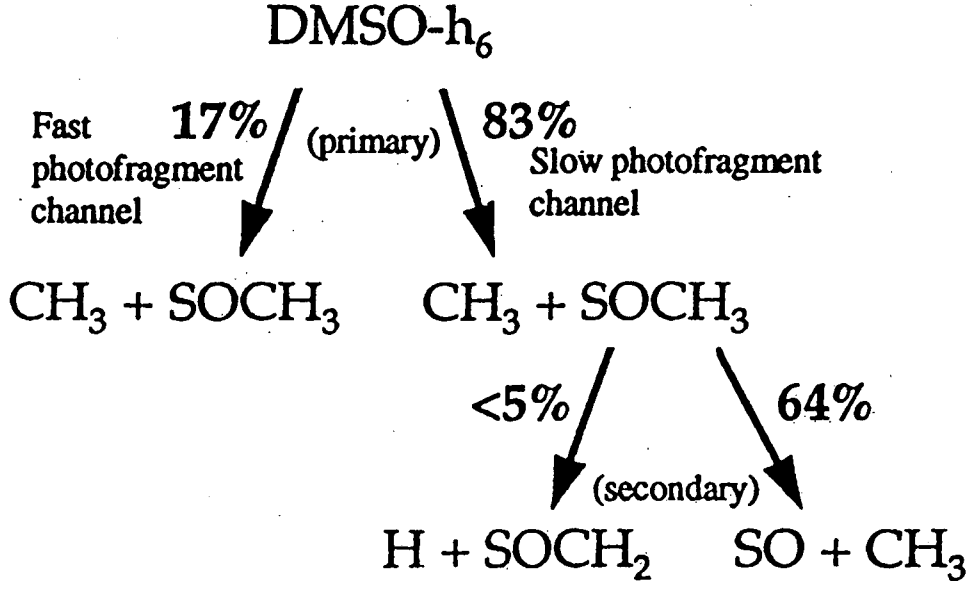
DMSO-h_6
Fast photofragment channel
17%
(primary)
83%
Slow photofragment channel
$CH_3 + SOCH_3$
$CH_3 + SOCH_3$
<5%
64%
(secondary)
$H + SOCH_2$
$SO + CH_3$

Figure 8

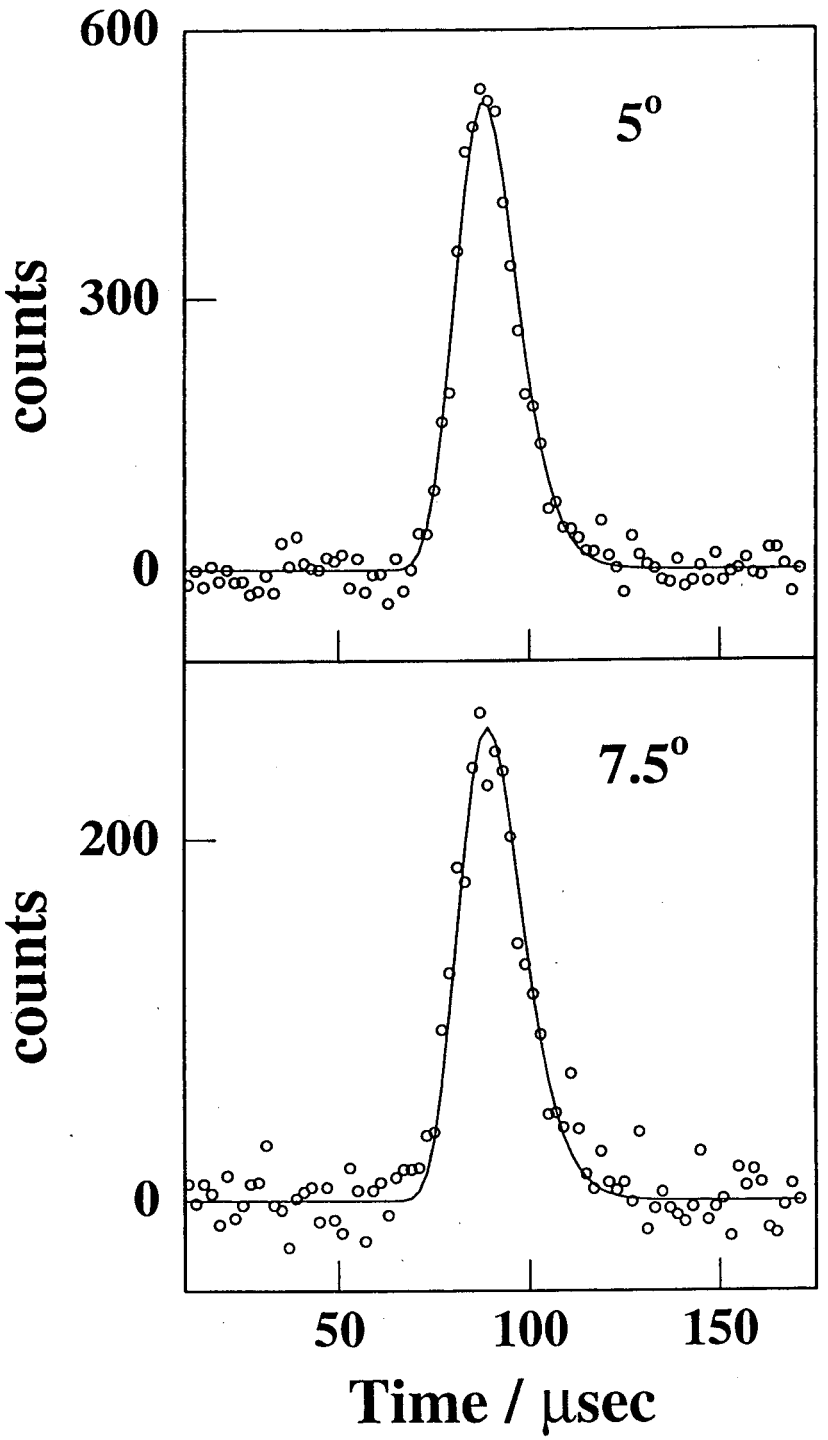

Figure 9

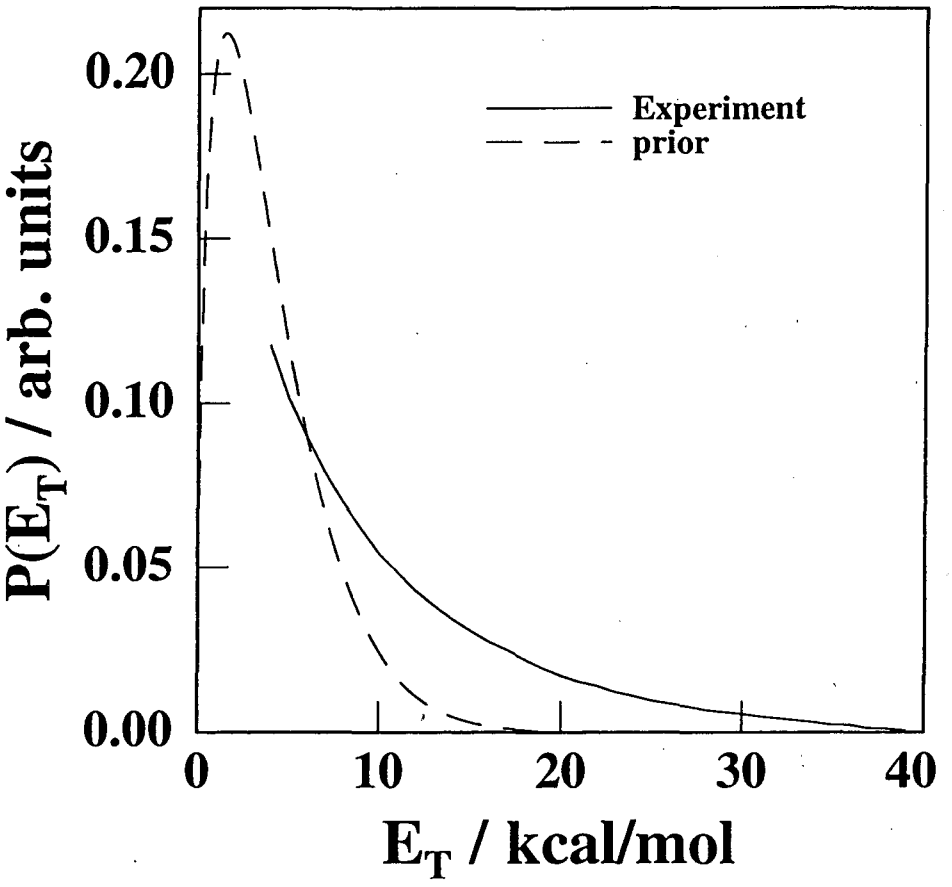
0.20
0.15
0.10
0.05
0.00
P(E_T) / arb. units
Experiment
prior
0
10
20
30
40
E_T / kcal/mol

Figure 10

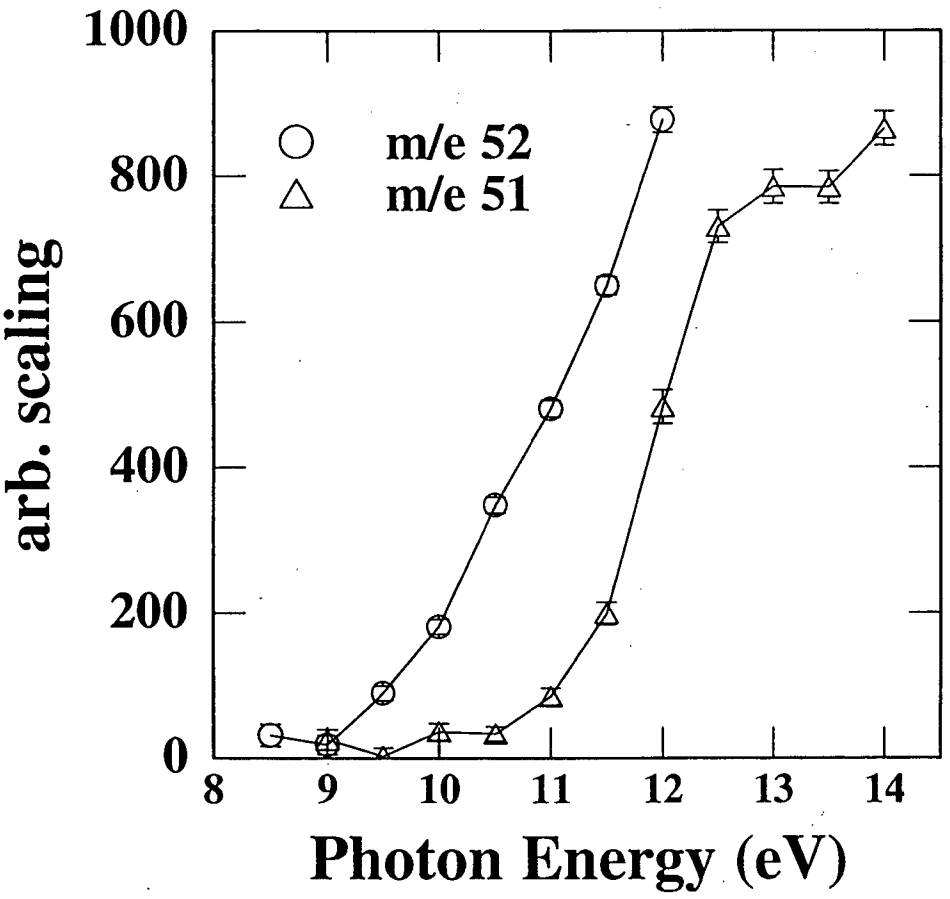
1000
800
600
400
200
0
arb. scaling
m/e 52
m/e 51
8
9
10
11
12
13
14
Photon Energy (eV)

Figure 11

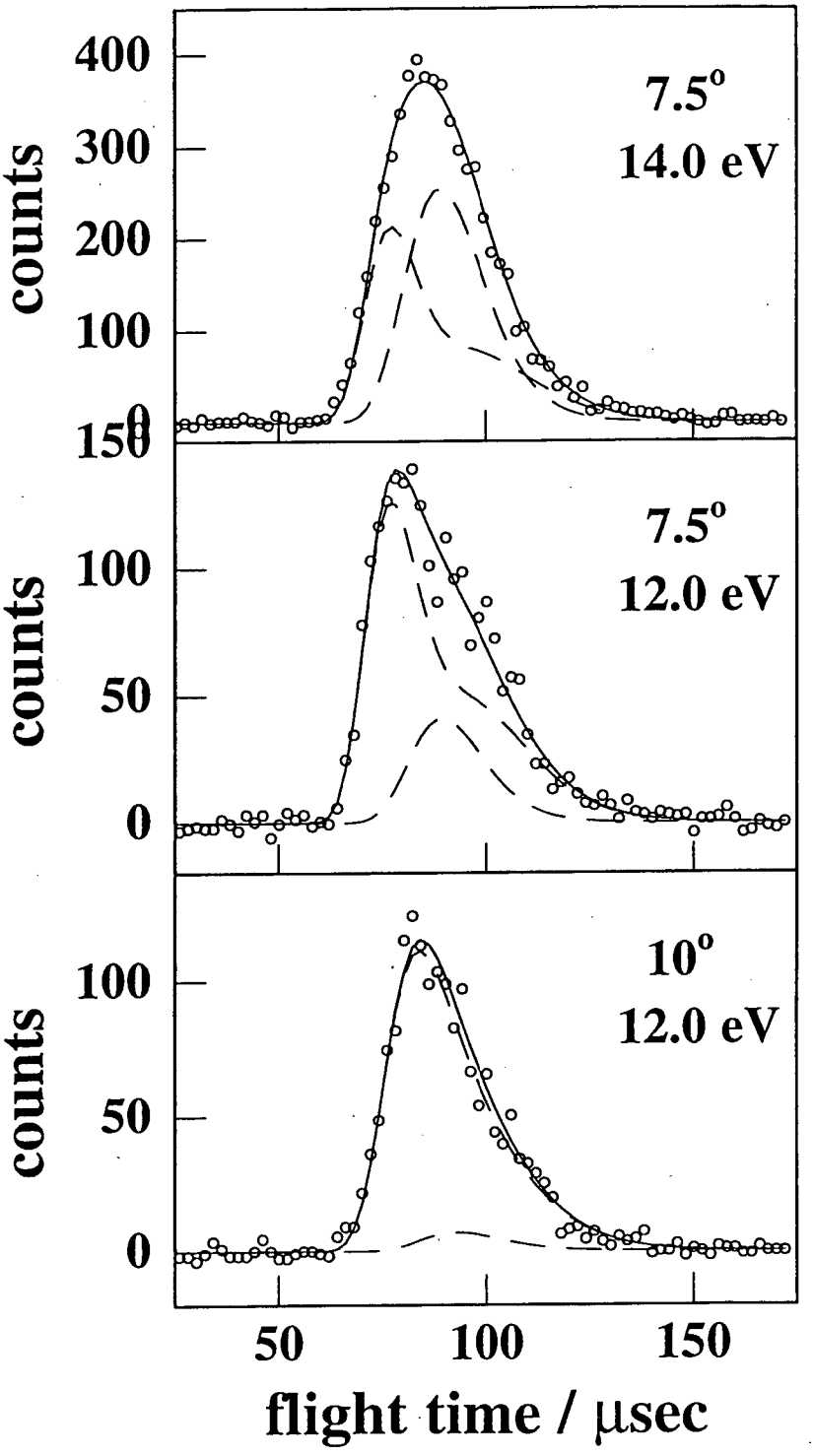
counts
400
300
200
100
0
7.5°
14.0 eV
counts
150
100
50
0
7.5°
12.0 eV
counts
100
50
0
10°
12.0 eV
50
100
150
flight time / μsec

Figure 12

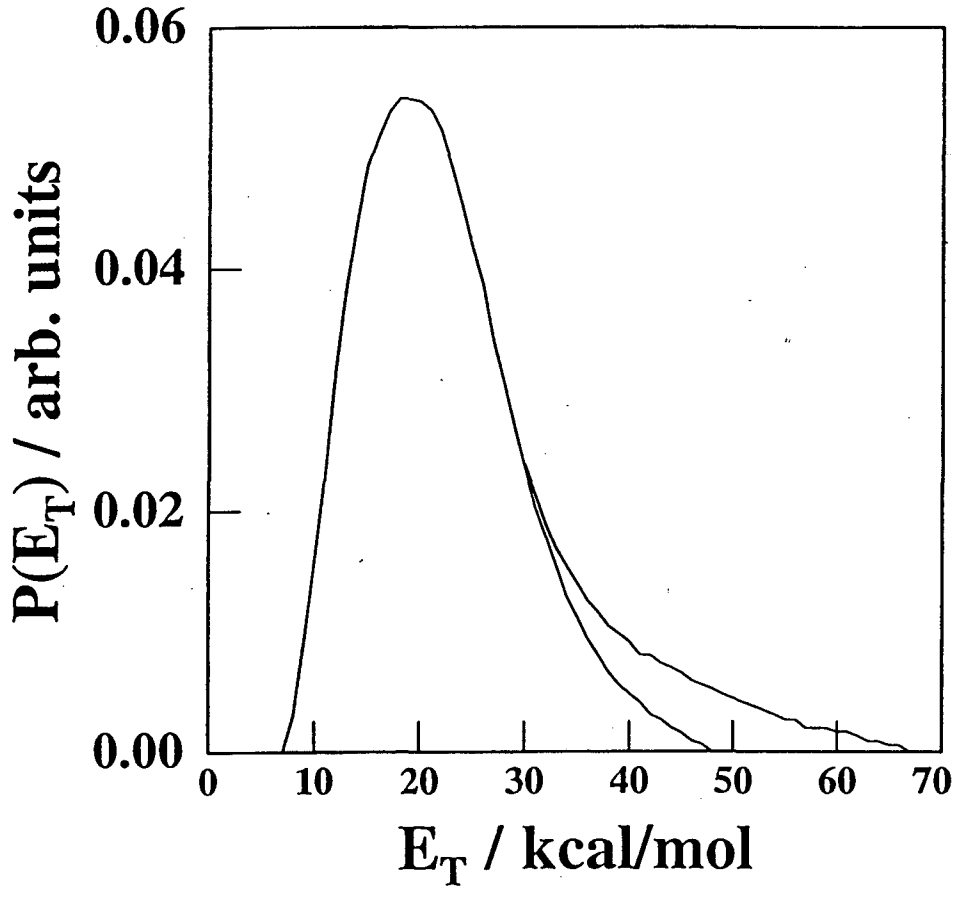

Figure 13

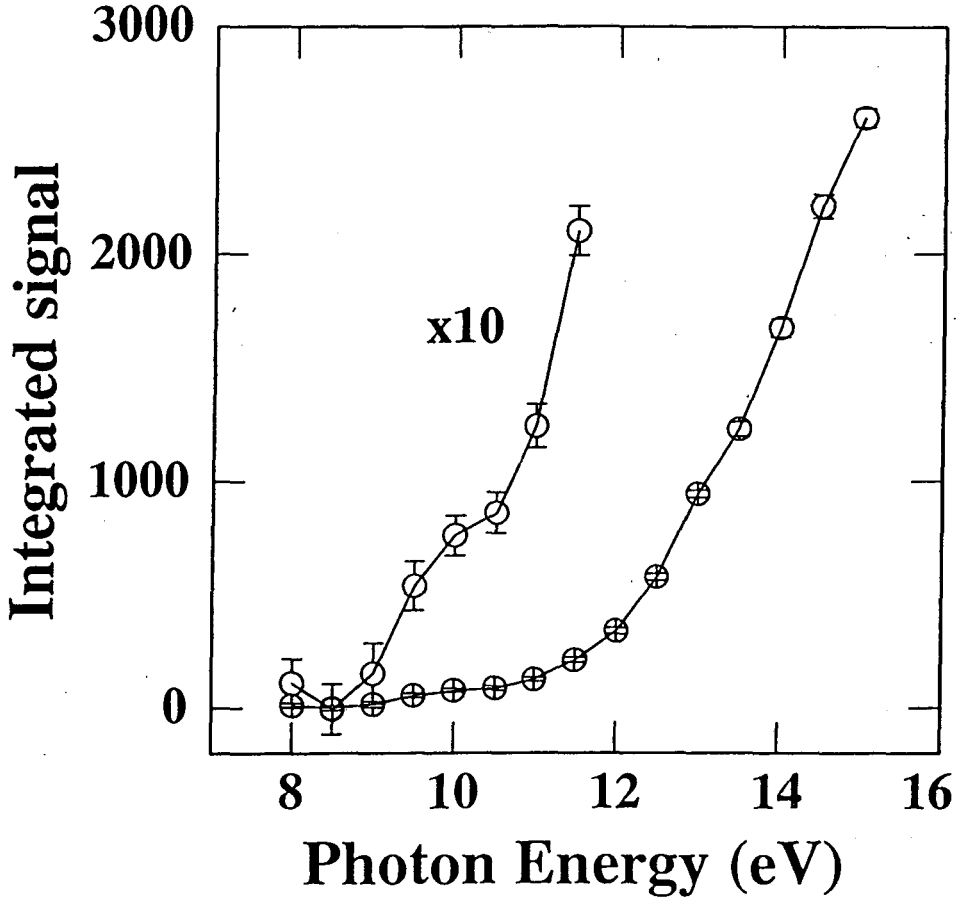
3000
2000
1000
0
Integrated signal
x10
8
10
12
14
16
Photon Energy (eV)

Figure 14

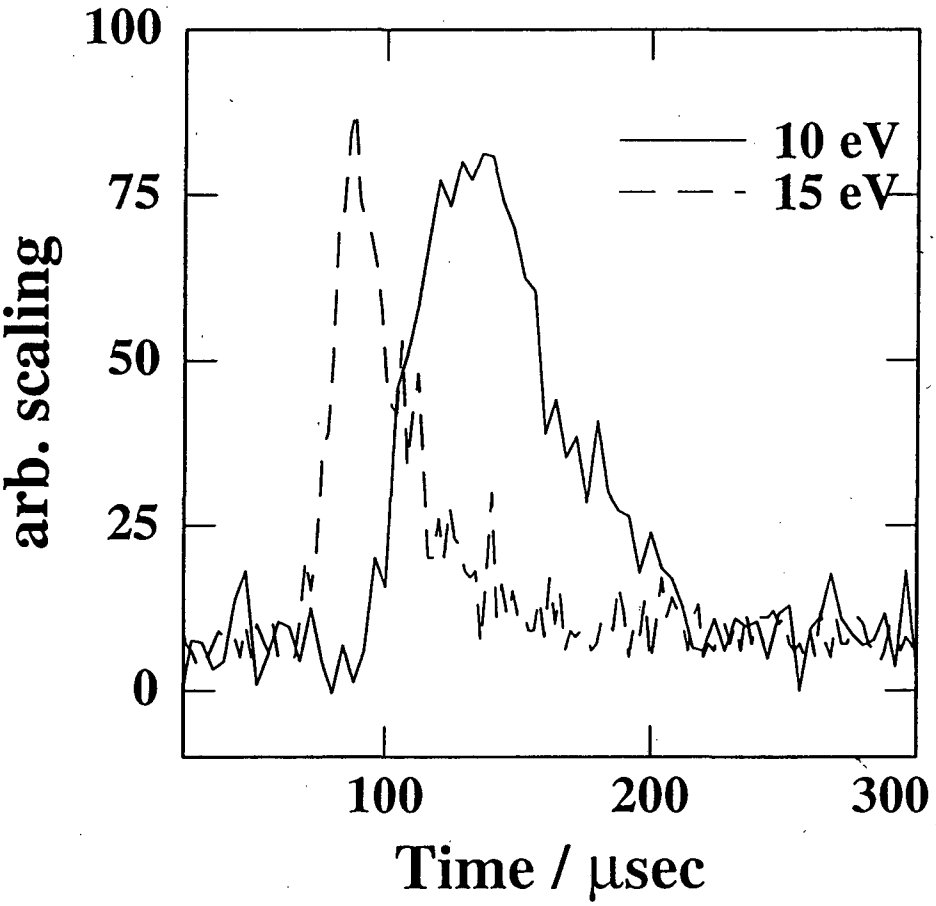

Figure 15

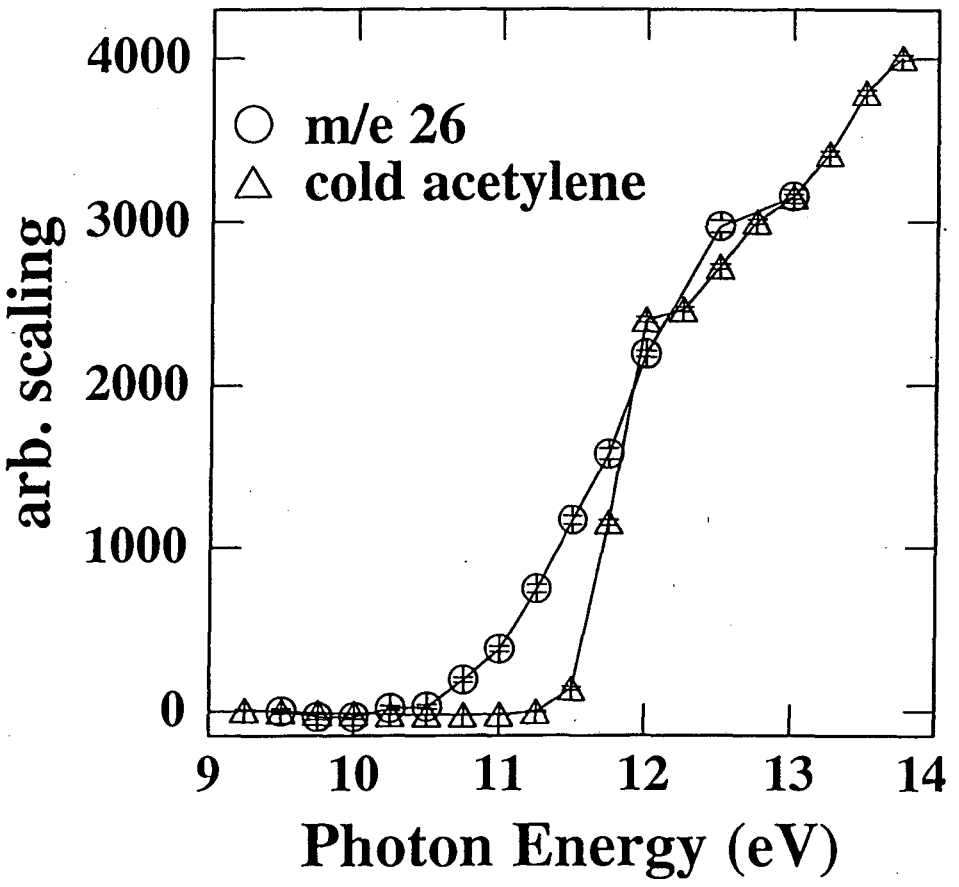
4000
3000
2000
1000
0
arb. scaling
m/e 26
cold acetylene
9
10
11
12
13
14
Photon Energy (eV)

Figure 16

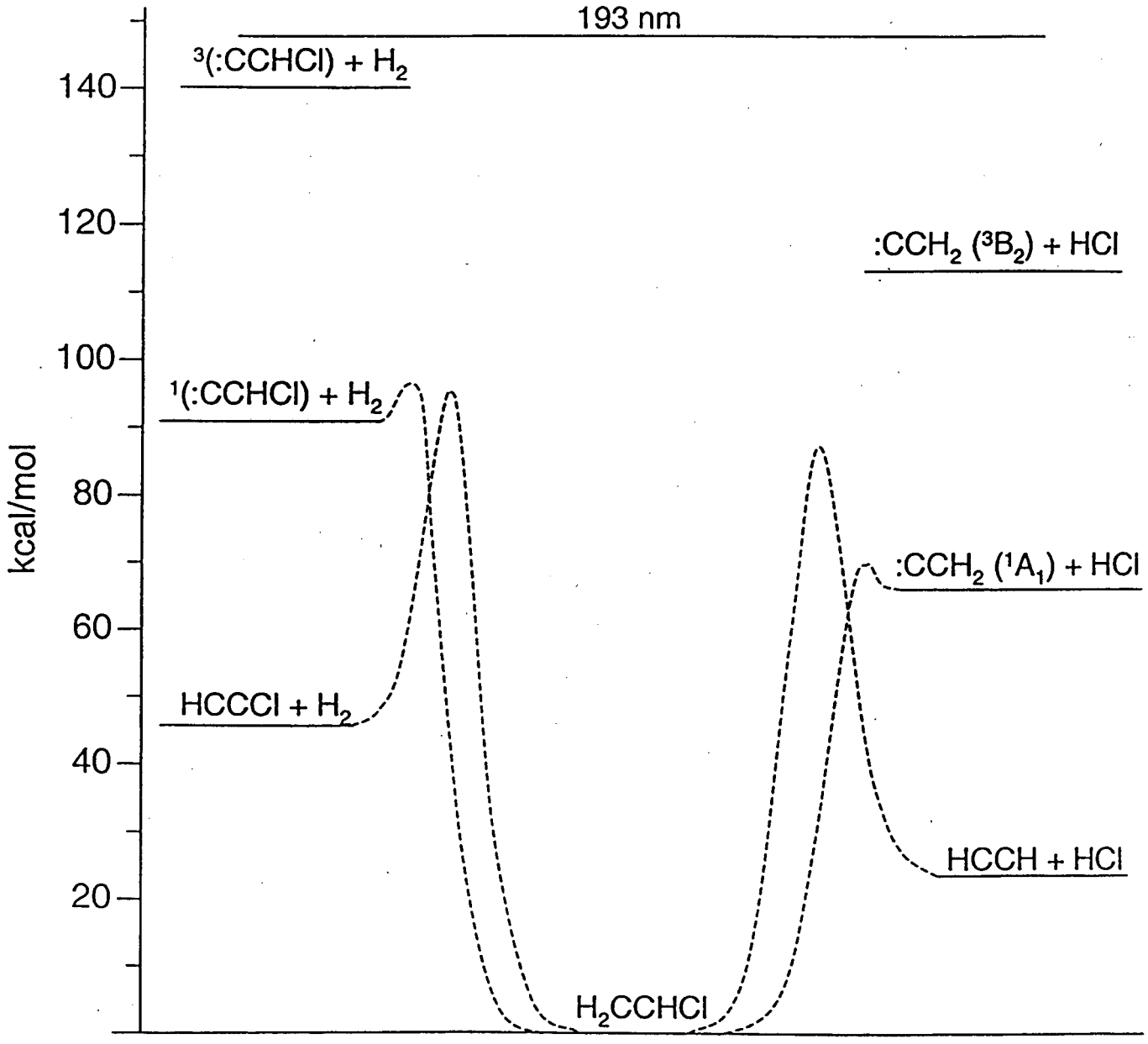
193 nm
^{3}(:CCHCl) + H_2
140
120
100
80
60
40
20
kcal/mol
:CCH_2 ($^3B_2$) + HCl
^{1}(:CCHCl) + H_2
:CCH_2 ($^1A_1$) + HCl
HCCCl + H_2
HCCH + HCl
H_2CCHCl

Figure 17

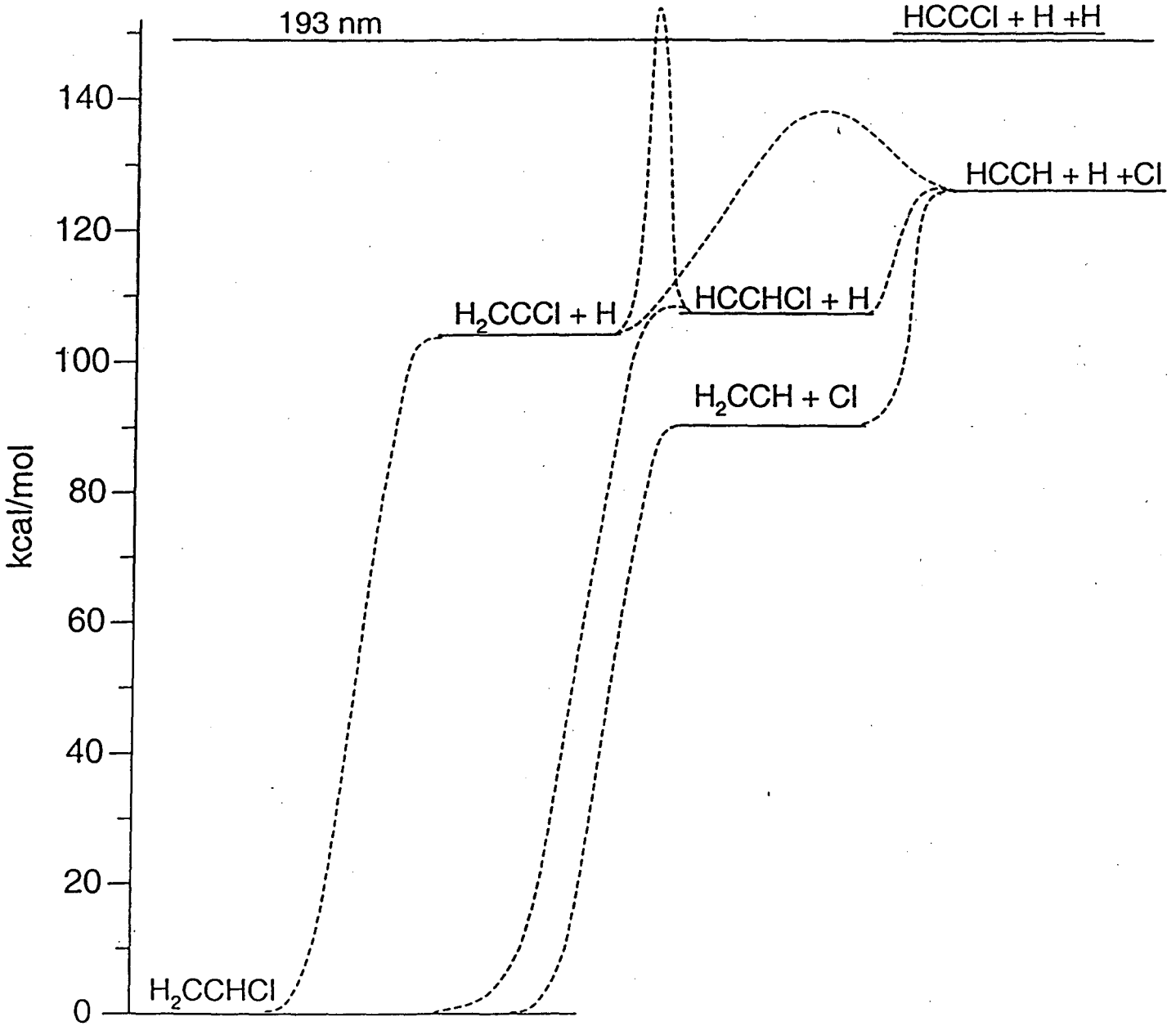
193 nm
HCCCl + H +H
140
120
100
80
60
40
20
0
kcal/mol
HCCH + H +Cl
H2CCCl + H
HCCHCl + H
H2CCH + Cl
H2CCHCl

Figure 18

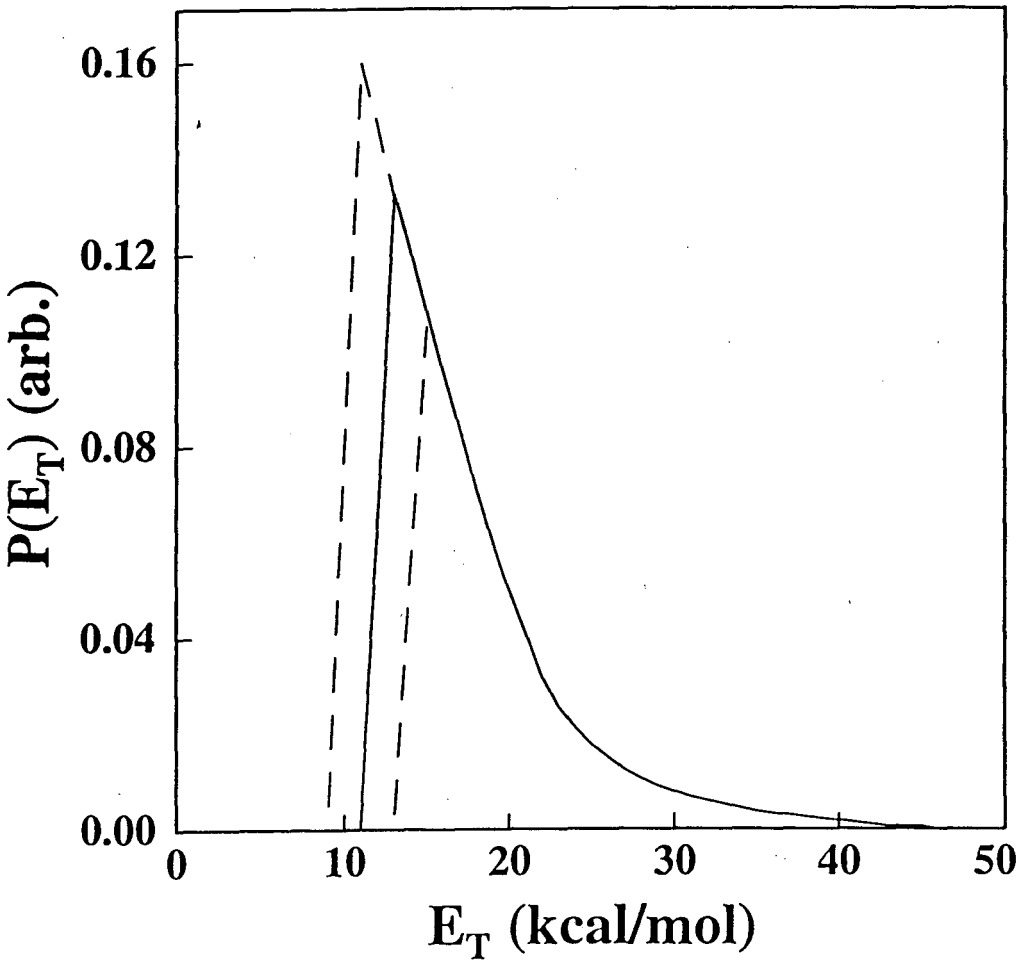

Figure 19

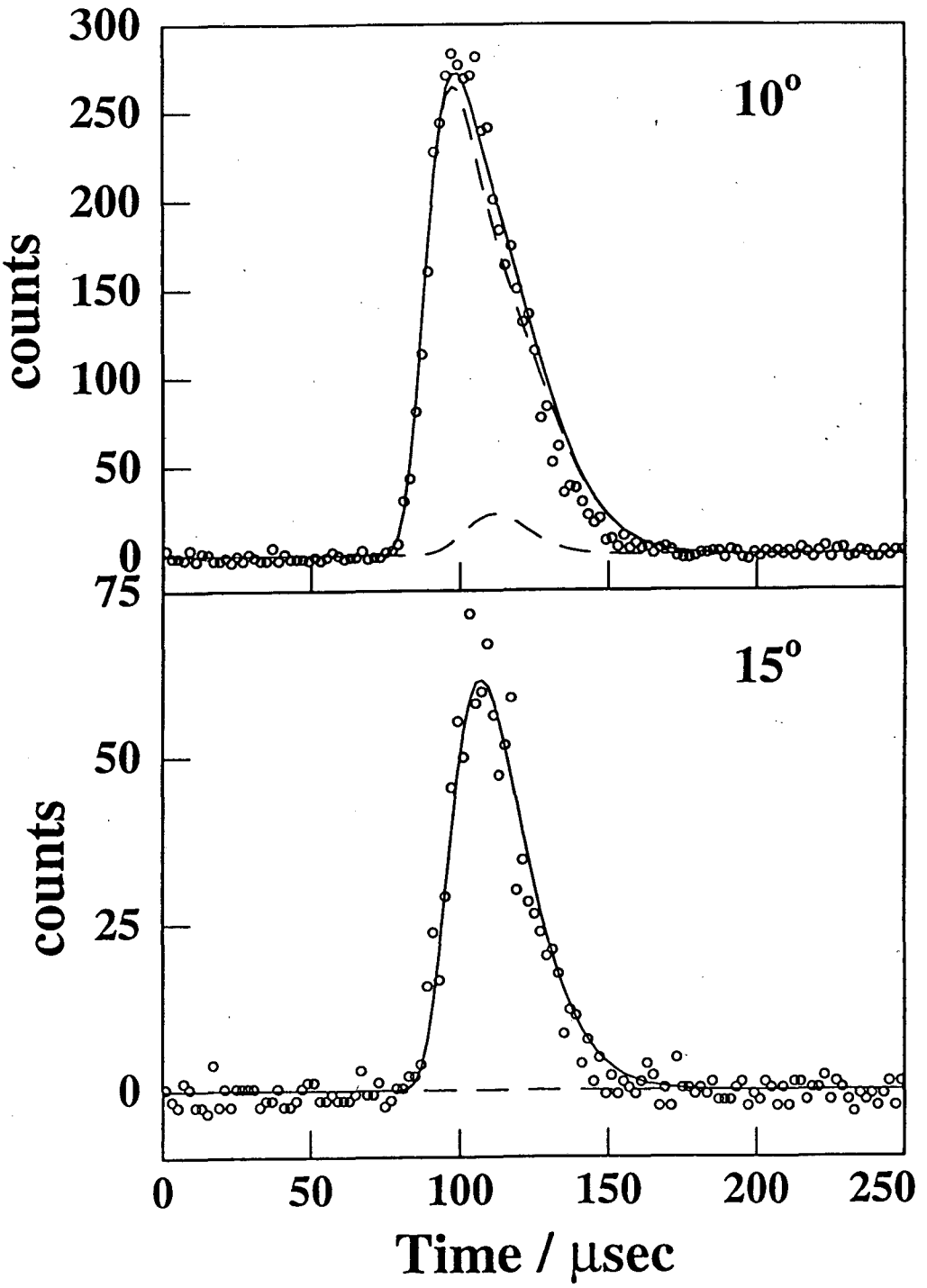
300
250
200
150
100
50
0
counts
10°
75
50
25
0
counts
15°
0
50
100
150
200
250
Time / μsec

Figure 20

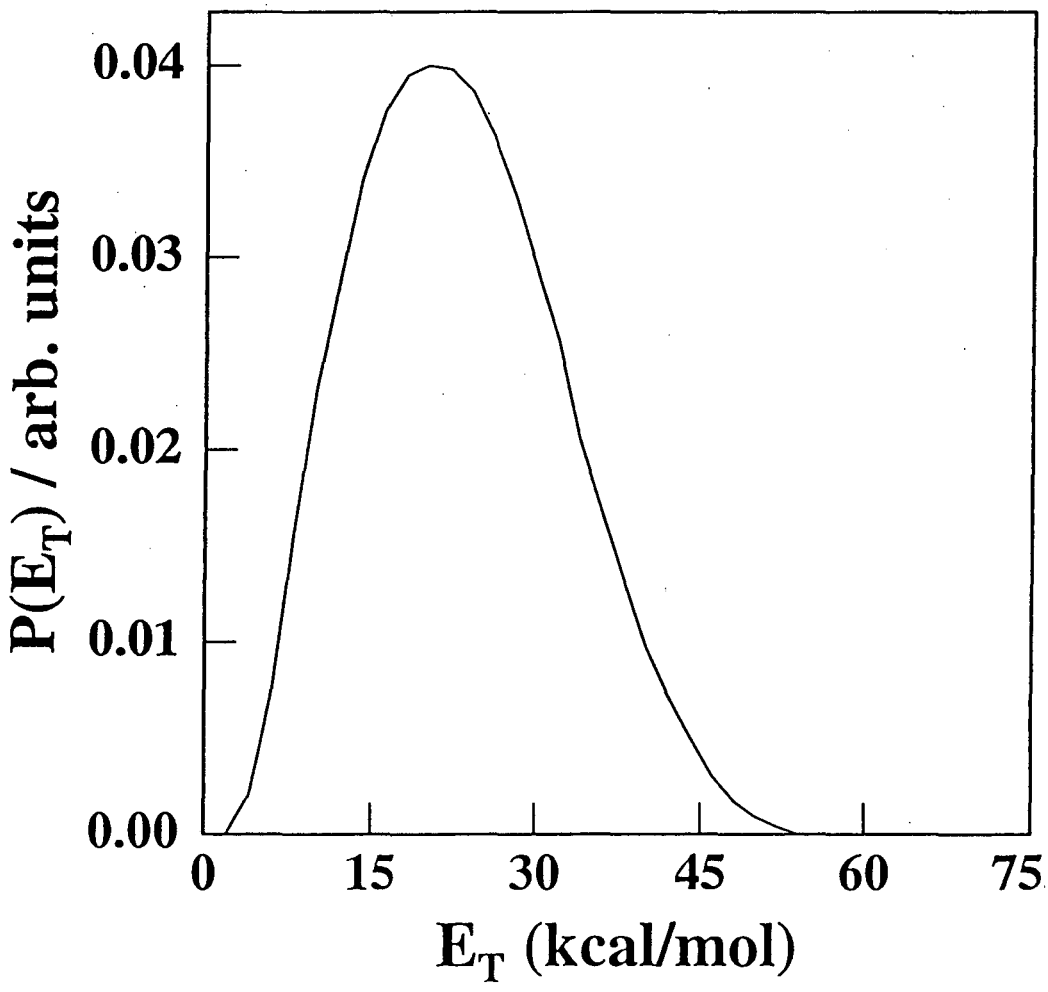

Figure 21

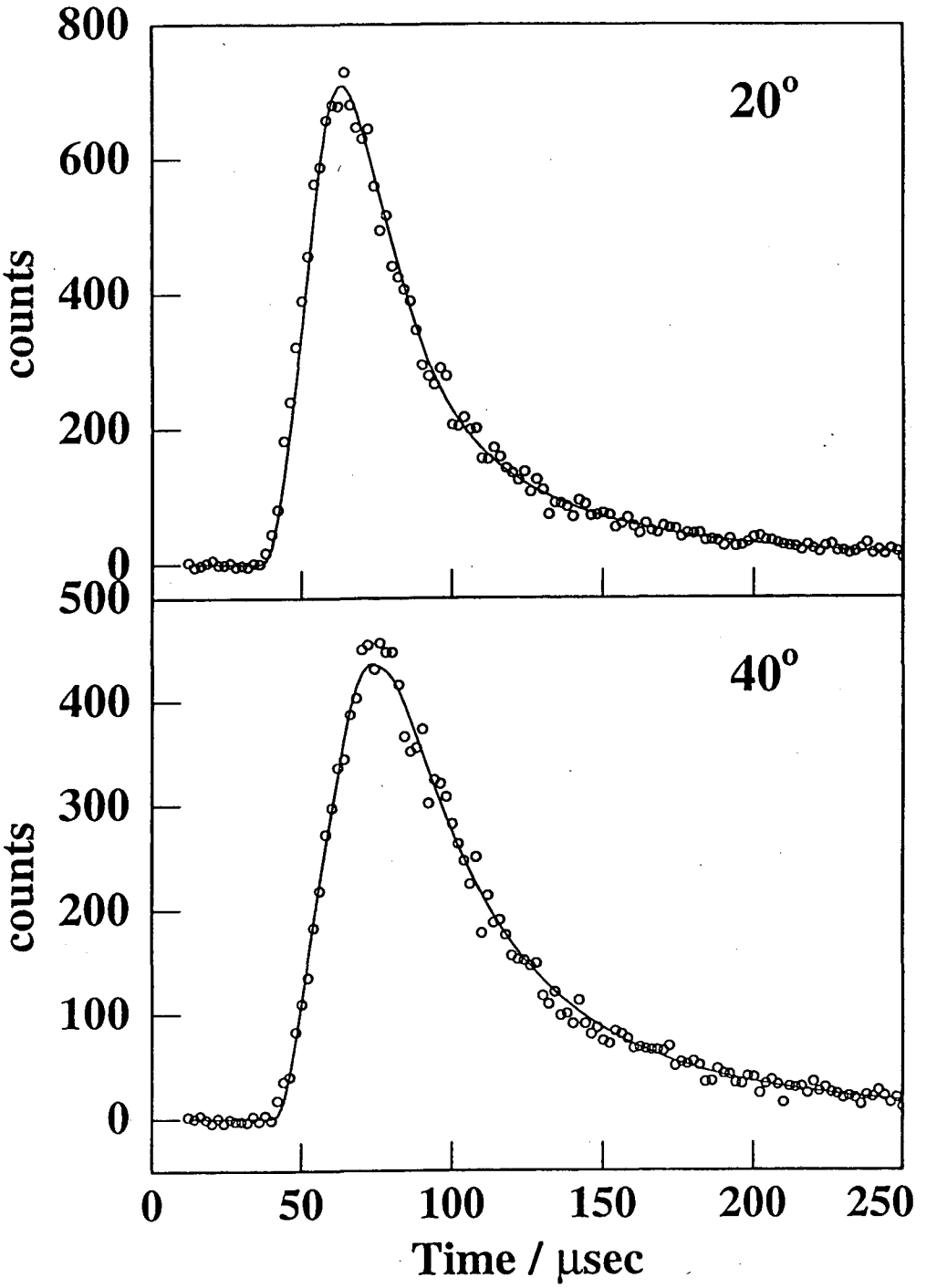
800
600
400
200
0
counts
20°
500
400
300
200
100
0
counts
40°
0
50
100
150
200
250
Time / μsec

Figure 22

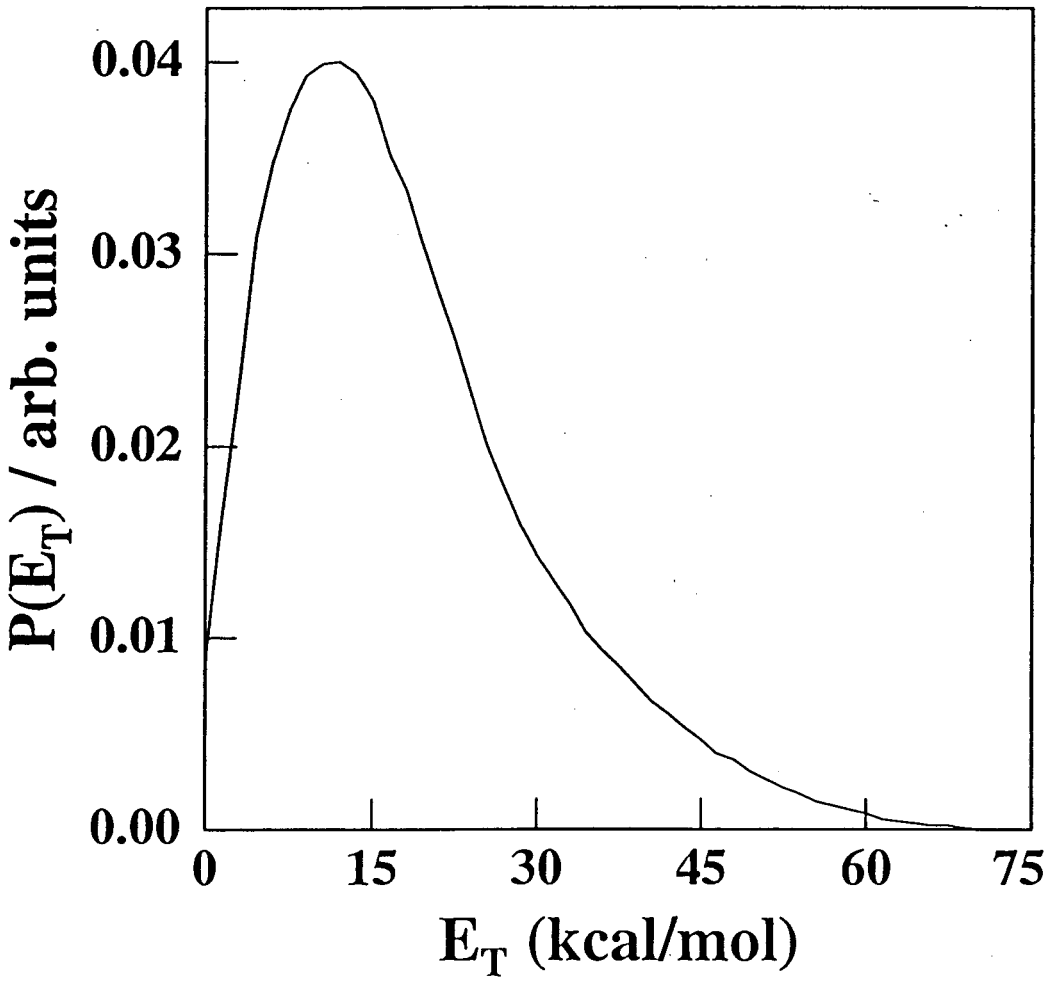

Figure 23

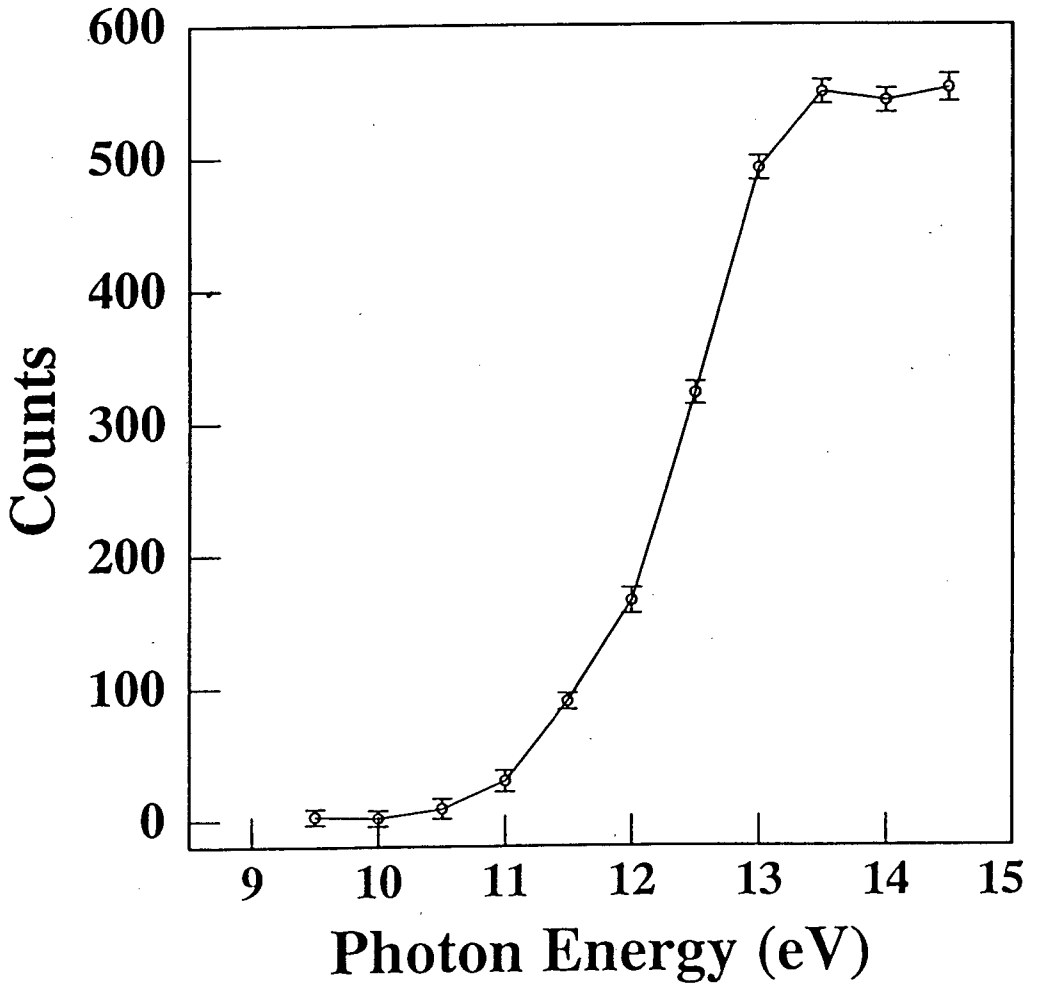
600
500
400
300
200
100
0
Counts
9
10
11
12
13
14
15
Photon Energy (eV)

Figure 24

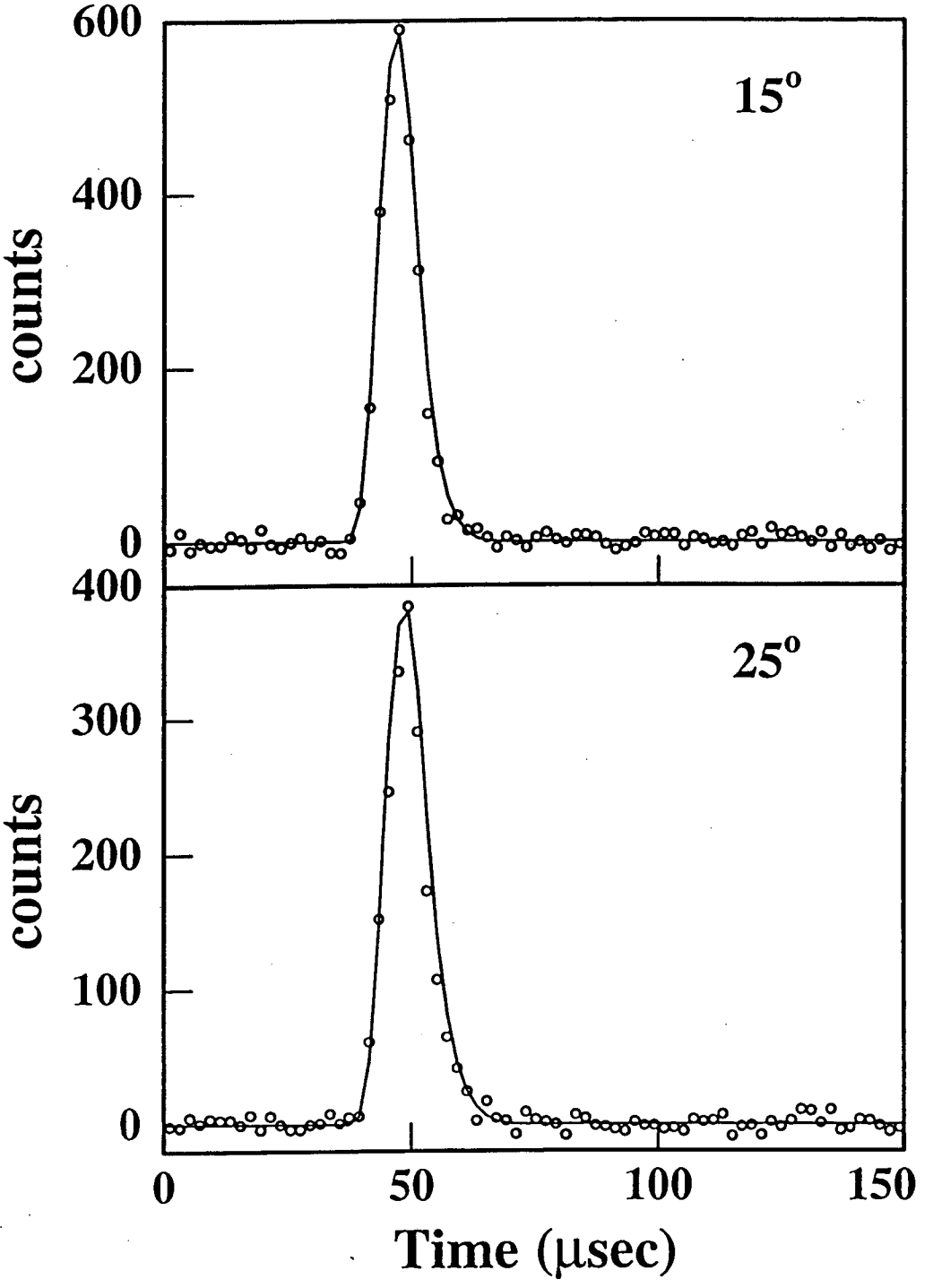
600
400
200
0
counts
15°
400
300
200
100
0
counts
25°
0
50
100
150
Time (μsec)

Figure 25

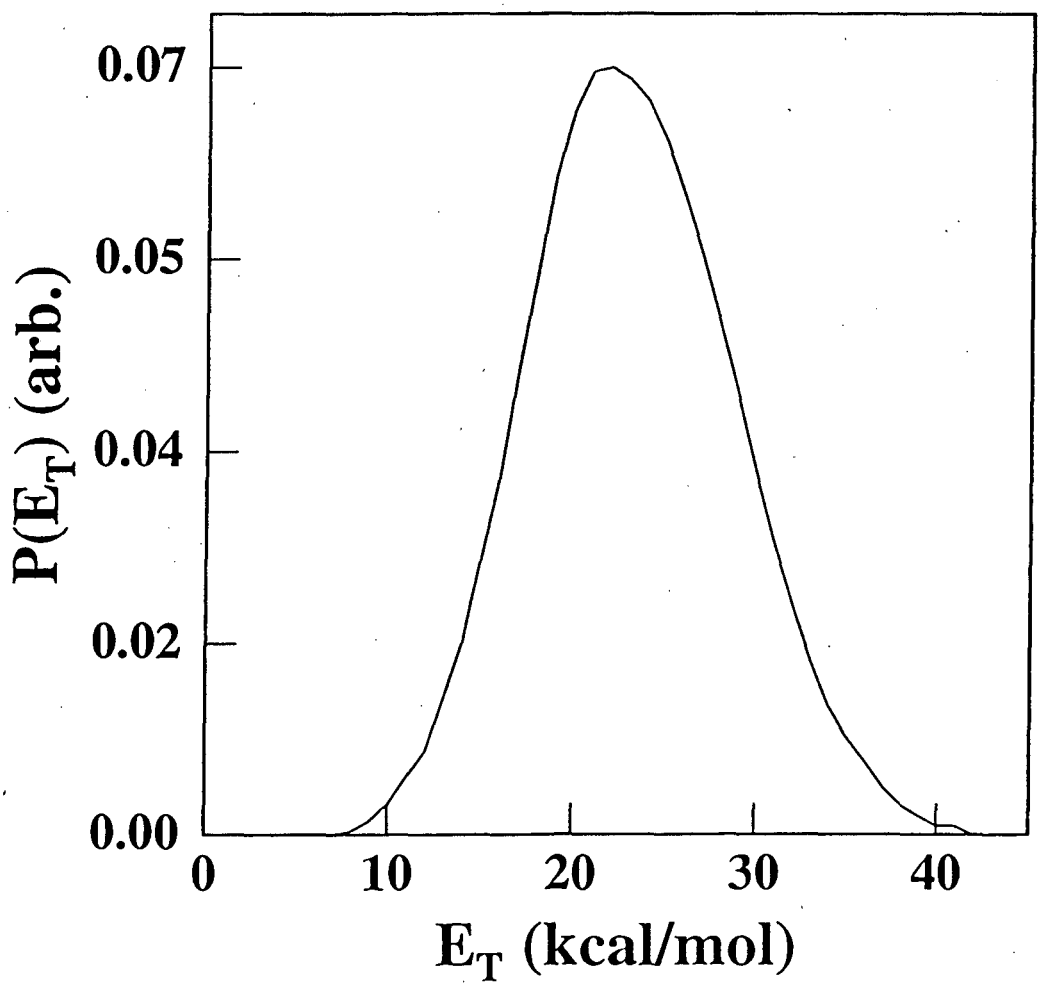

Figure 26

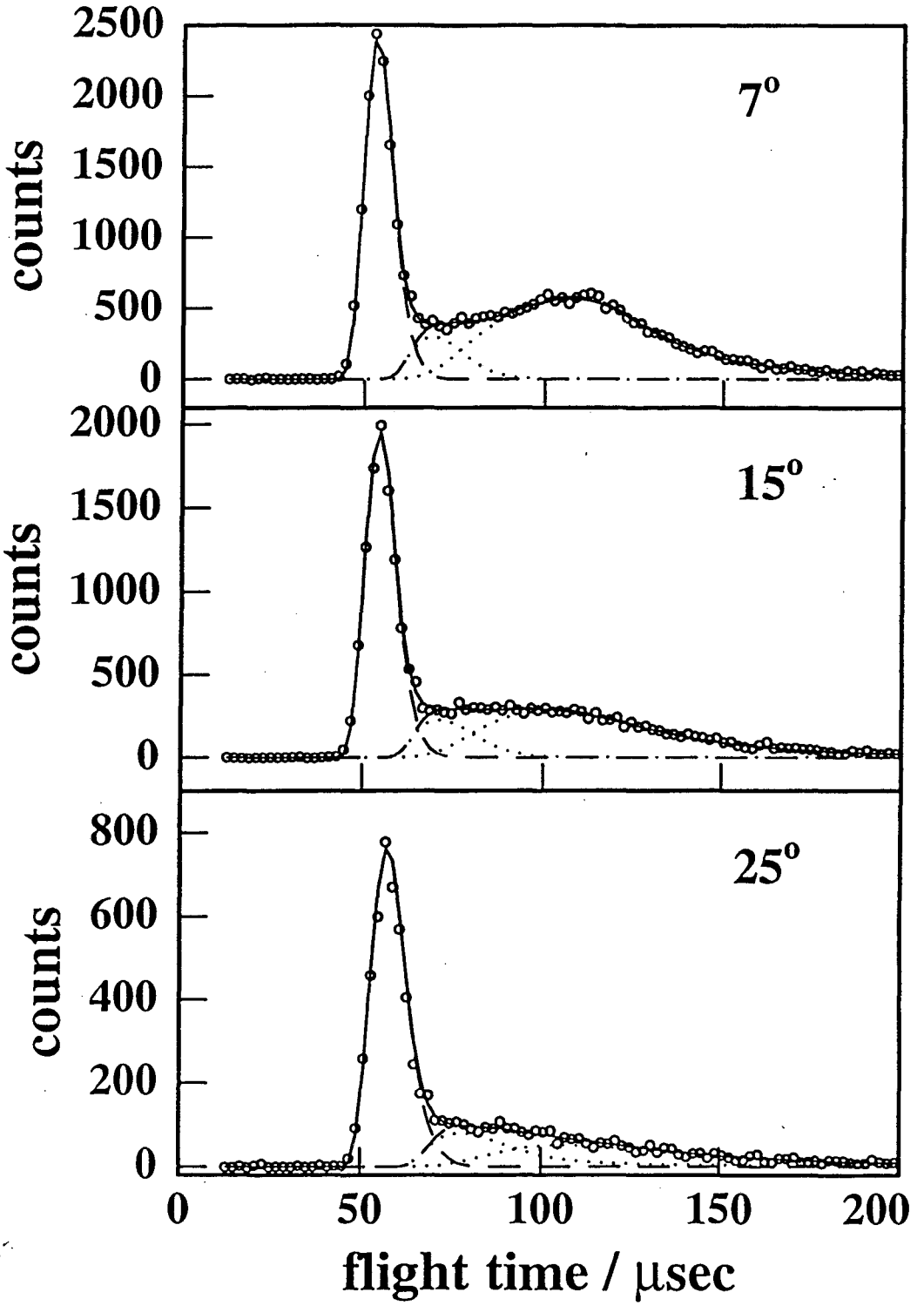
2500
2000
1500
1000
500
0
counts
7°
2000
1500
1000
500
0
counts
15°
800
600
400
200
0
counts
25°
0
50
100
150
200
flight time / μsec

Figure 27

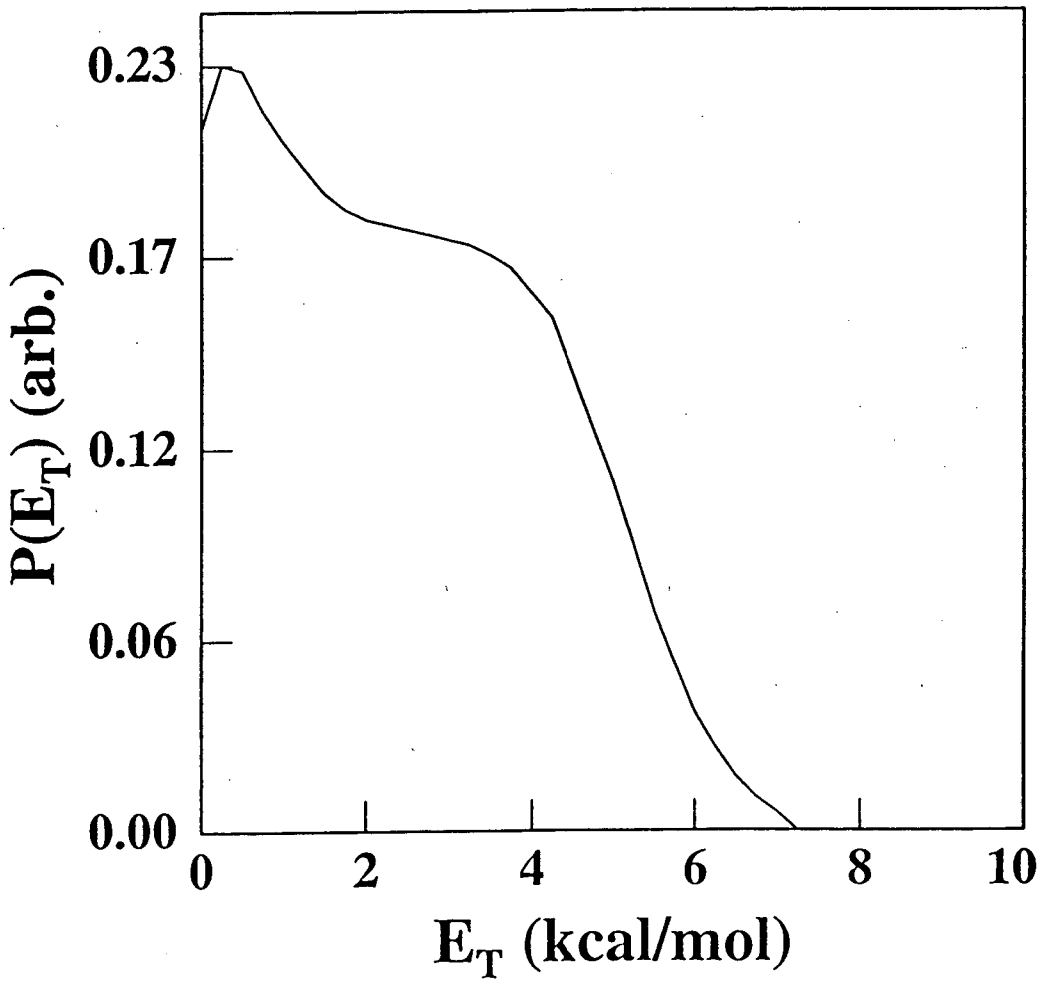

Figure 28

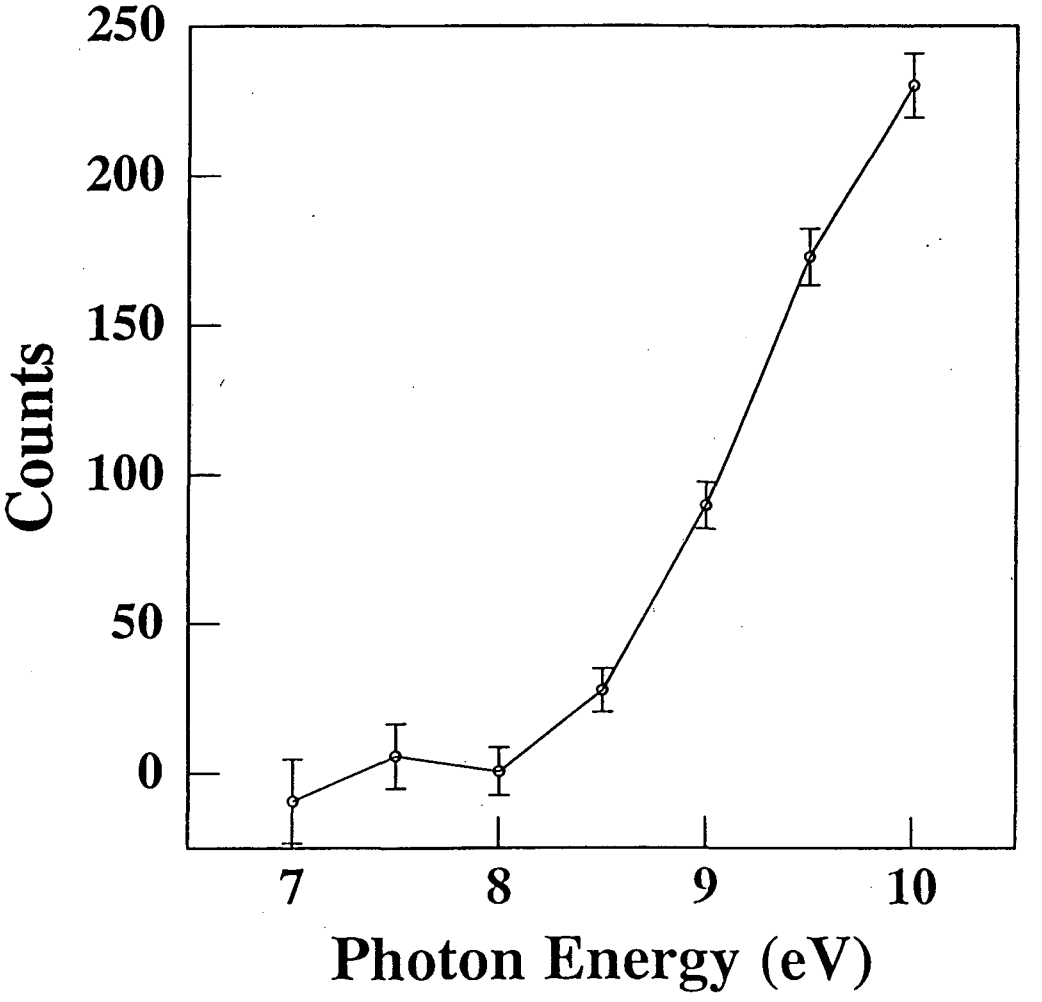

Figure 29

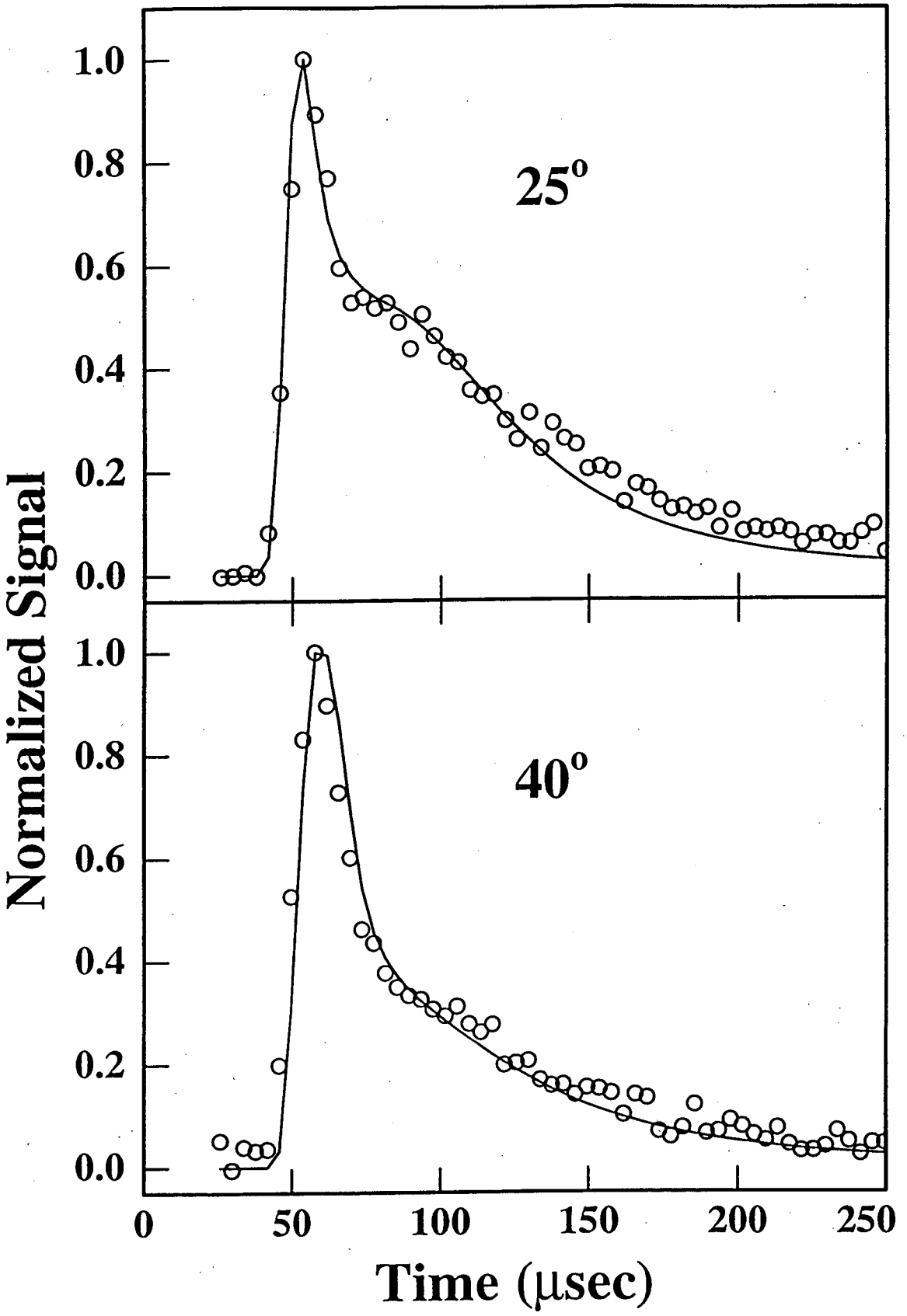
Normalized Signal
1.0
0.8
0.6
0.4
0.2
0.0
25°
40°
0
50
100
150
200
250
Time (μsec)

Figure 30

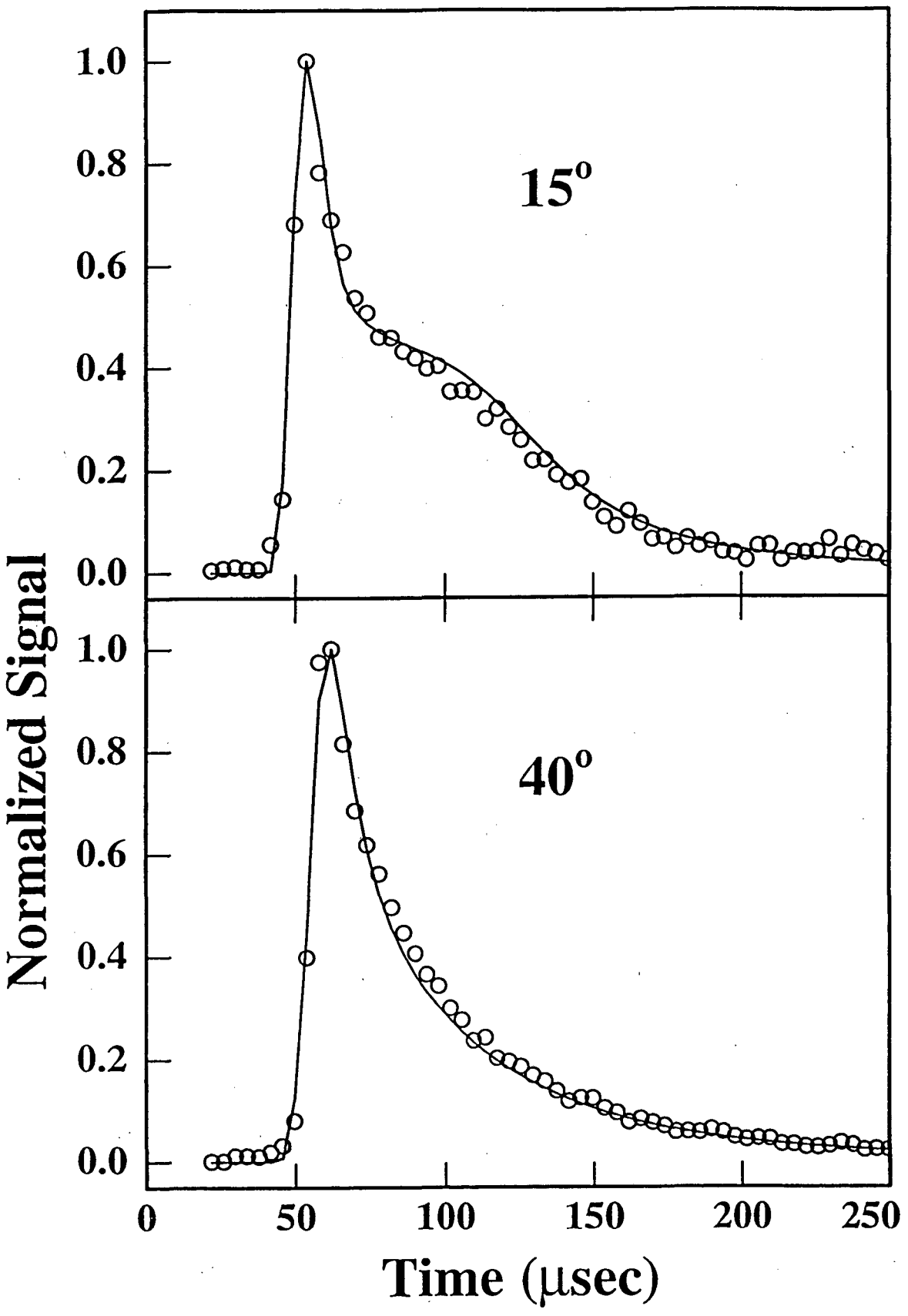
1.0
0.8
0.6
0.4
0.2
0.0
15°
1.0
0.8
0.6
0.4
0.2
0.0
40°
Normalized Signal
0
50
100
150
200
250
Time (μsec)

Figure 31

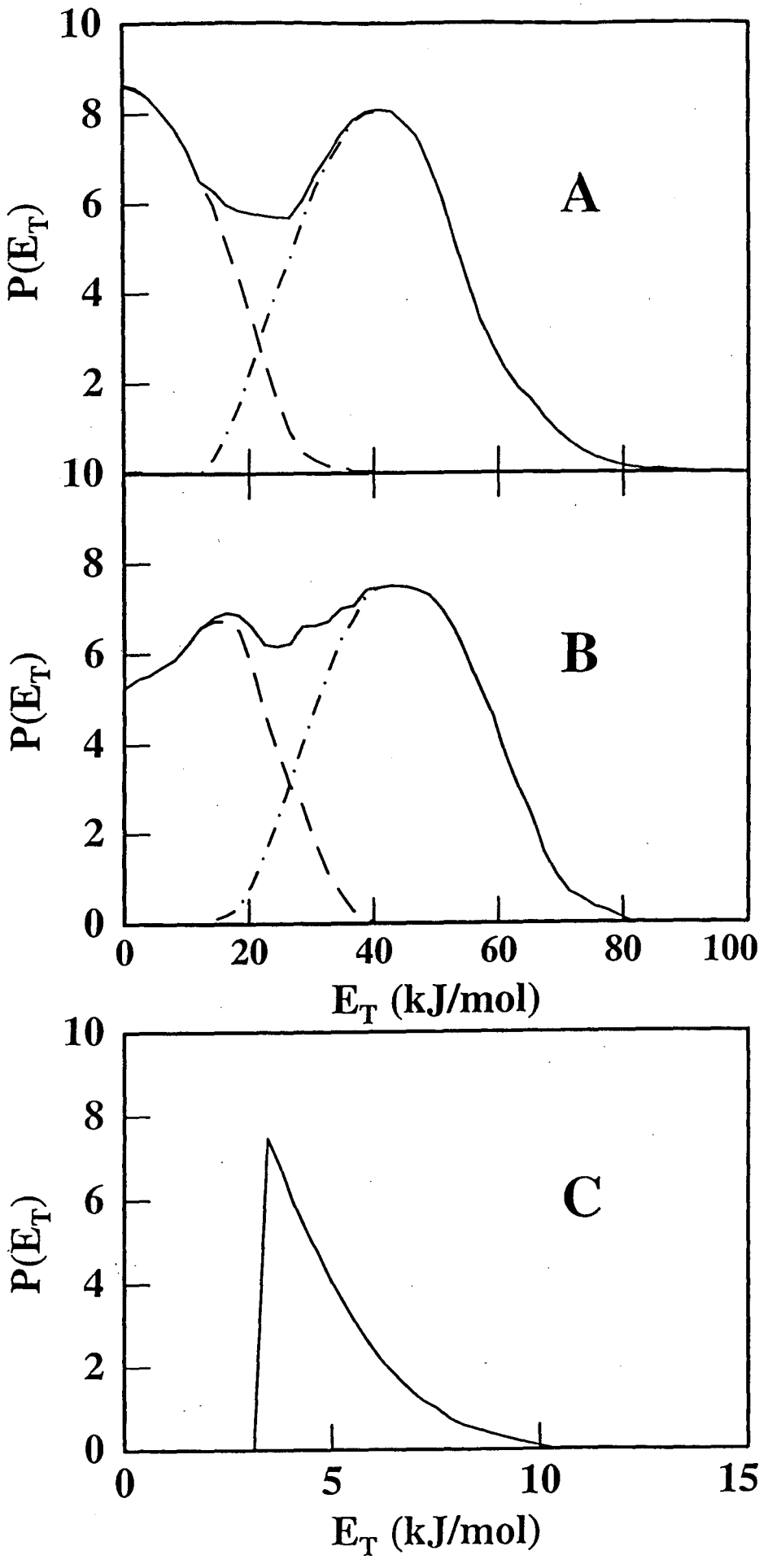

Figure 32

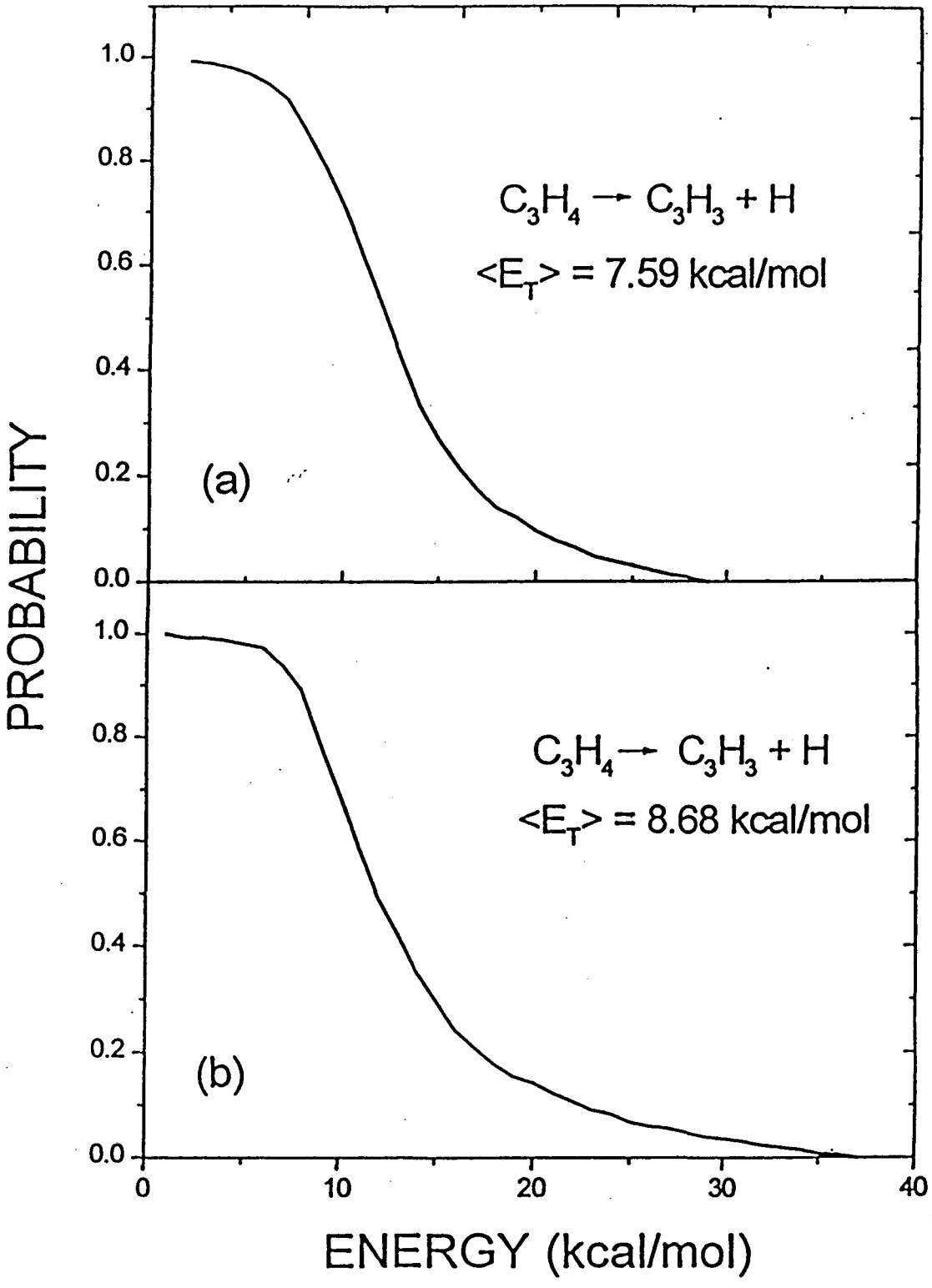
PROBABILITY
1.0
0.8
0.6
0.4
0.2
0.0
$C_3H_4 \rightarrow C_3H_3 + H$
$\langle E_T \rangle$ = 7.59 kcal/mol
(a)
1.0
0.8
0.6
0.4
0.2
0.0
$C_3H_4 \rightarrow C_3H_3 + H$
$\langle E_T \rangle$ = 8.68 kcal/mol
(b)
0
10
20
30
40
ENERGY (kcal/mol)

Figure 33

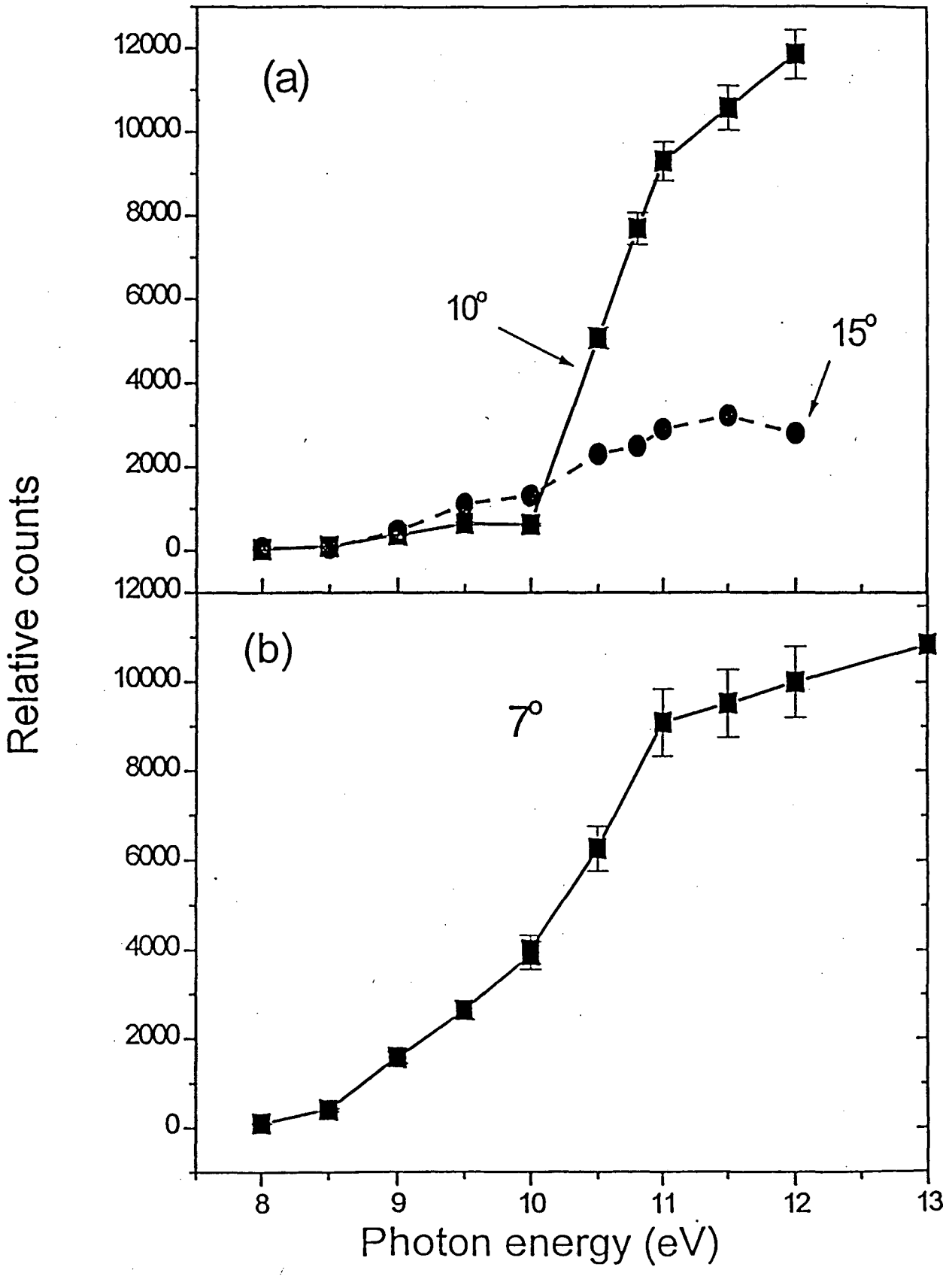
(a)
(b)
10°
15°
7°
Relative counts
Photon energy (eV)
12000
10000
8000
6000
4000
2000
0
8
9
10
11
12
13

Figure 34

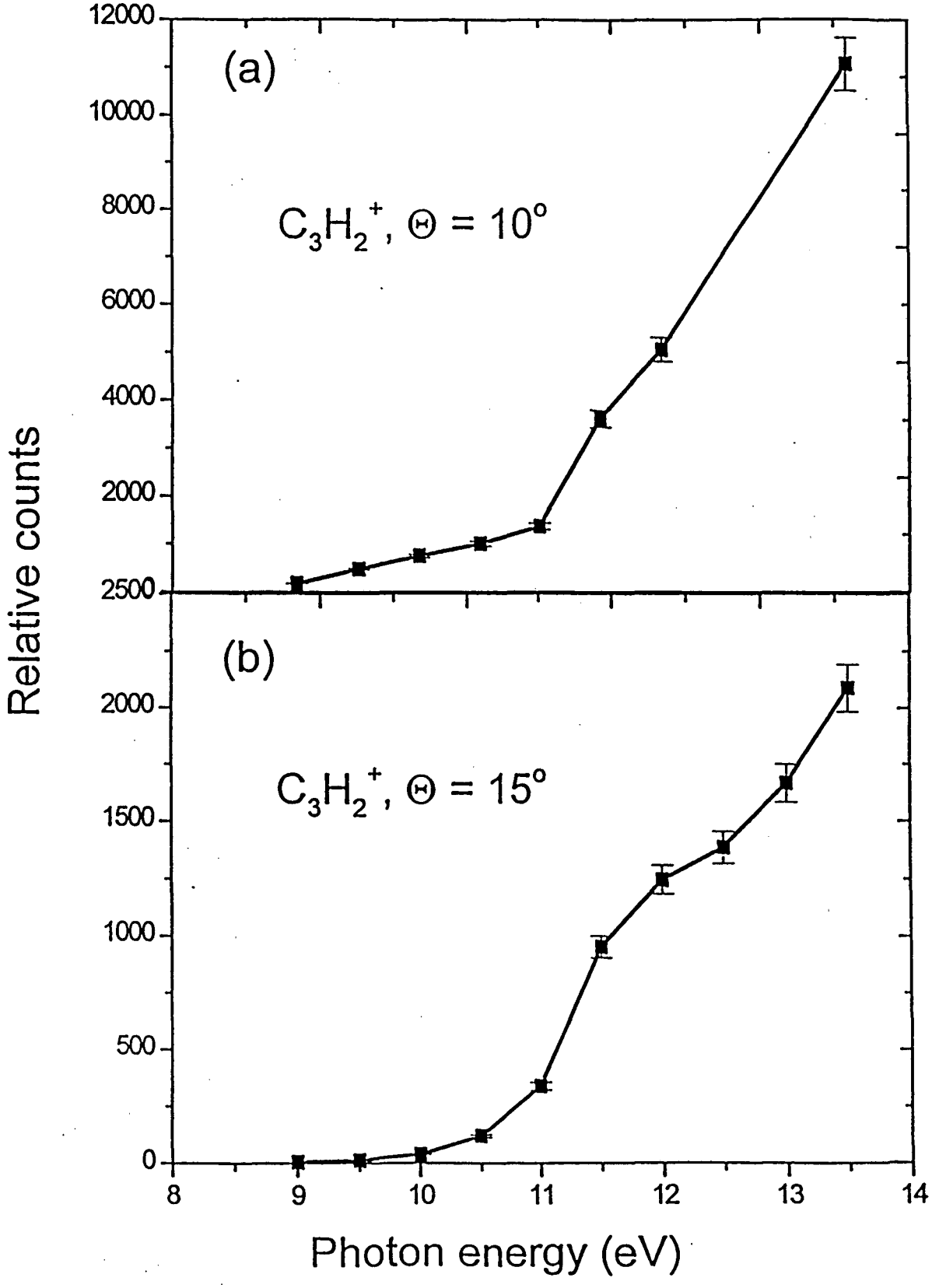
(a)
$C_3H_2^+$, Θ = 10°
(b)
$C_3H_2^+$, Θ = 15°
Relative counts
Photon energy (eV)
12000
10000
8000
6000
4000
2000
2500
2000
1500
1000
500
0
8
9
10
11
12
13
14

Figure 35

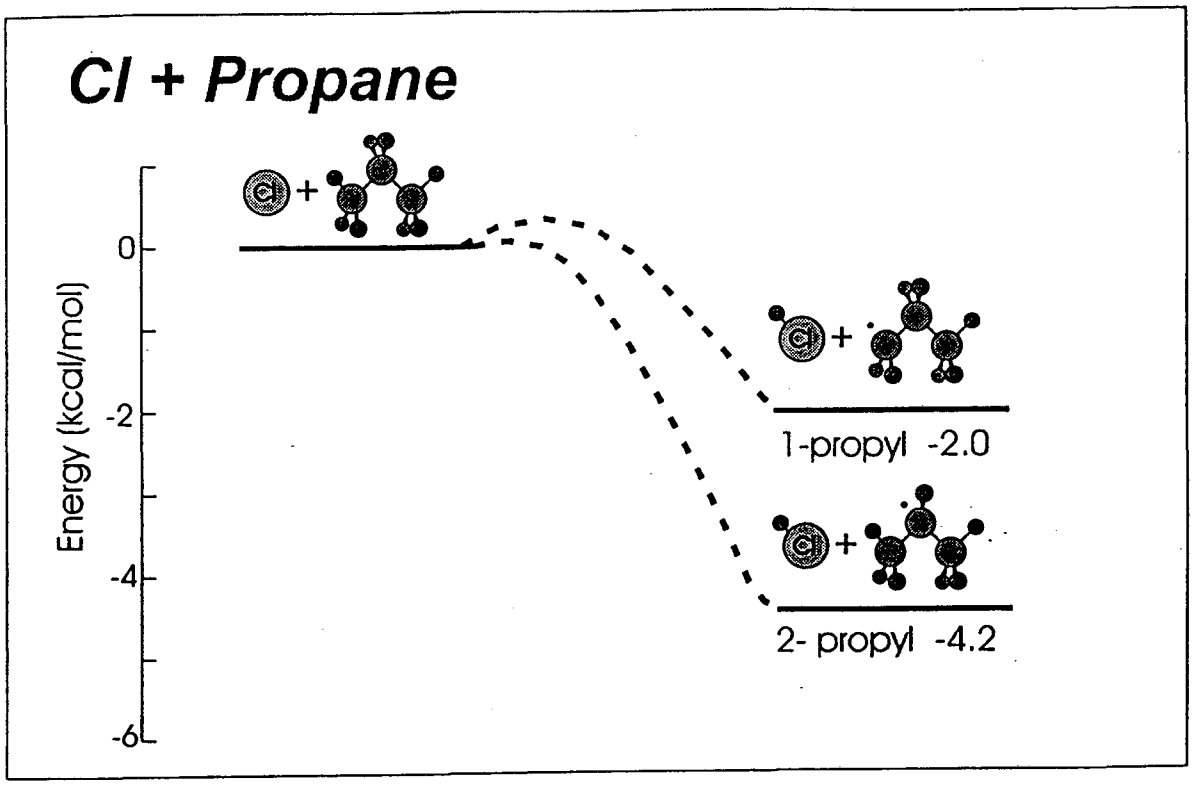
Cl + Propane
Energy (kcal/mol)
0
-2
-4
-6
Cl +
1-propyl -2.0
2- propyl -4.2

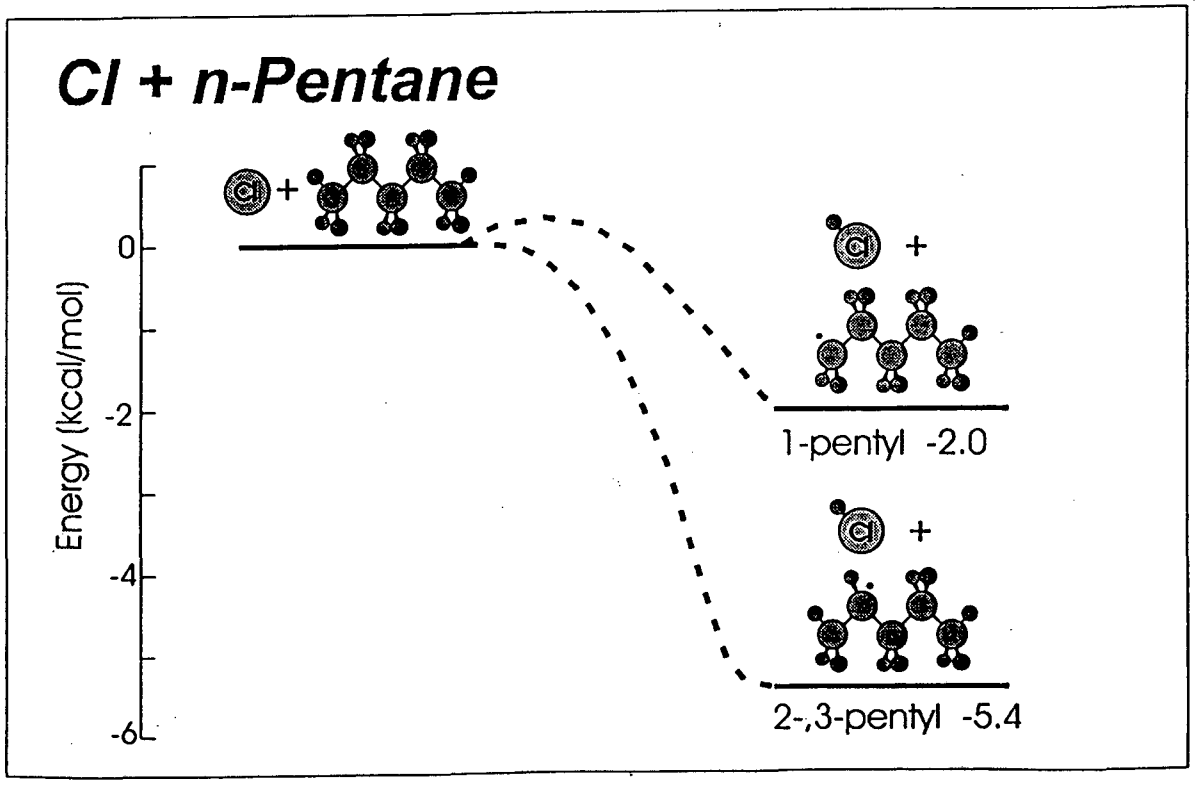
Cl + n-Pentane
Energy (kcal/mol)
0
-2
-4
-6
Cl +
1-pentyl -2.0
2-,3-pentyl -5.4

Figure 36

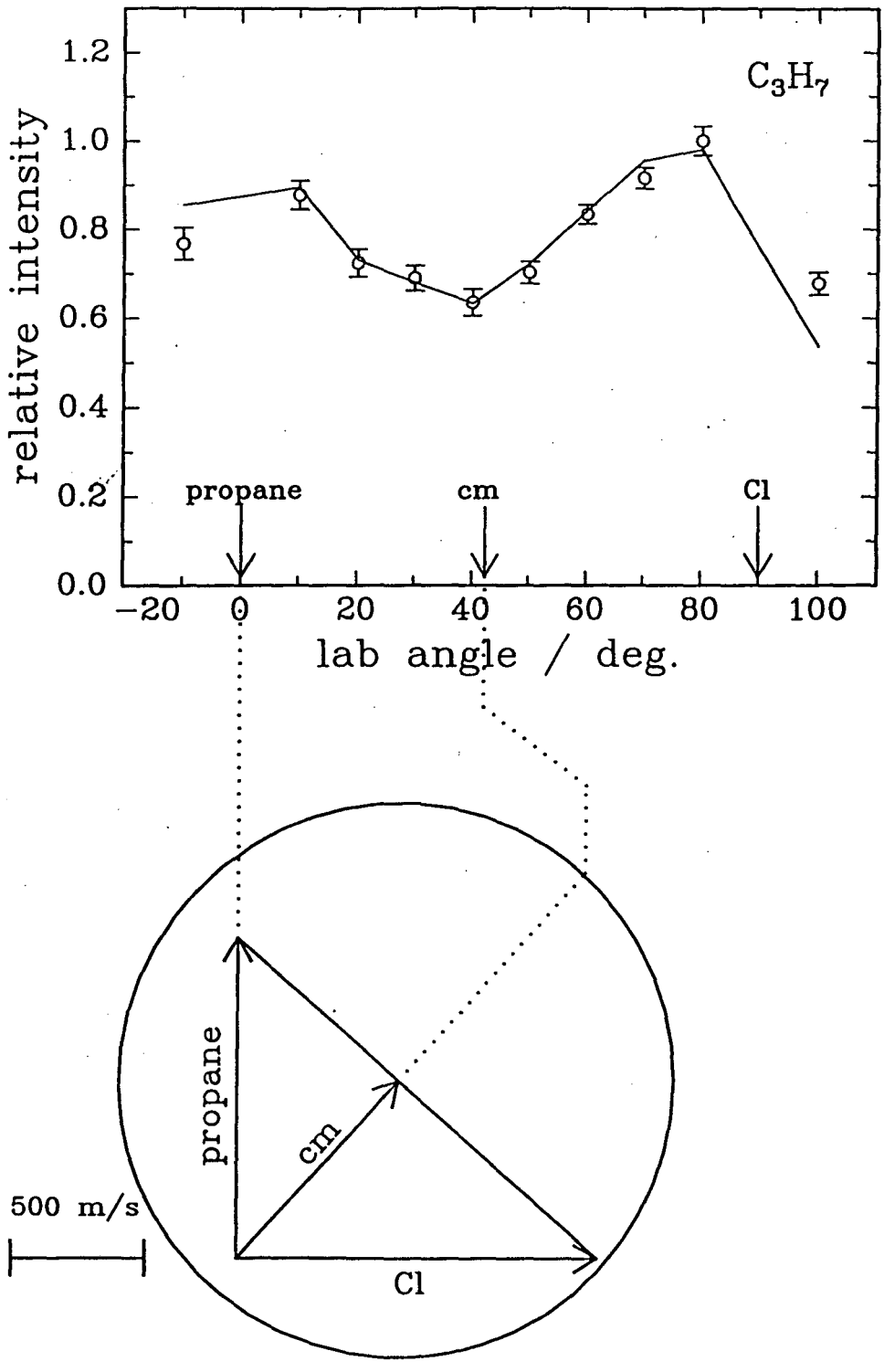
relative intensity
1.2
1.0
0.8
0.6
0.4
0.2
0.0
C_3H_7
propane
cm
Cl
−20
0
20
40
60
80
100
lab angle / deg.
propane
cm
Cl
500 m/s

Figure 37

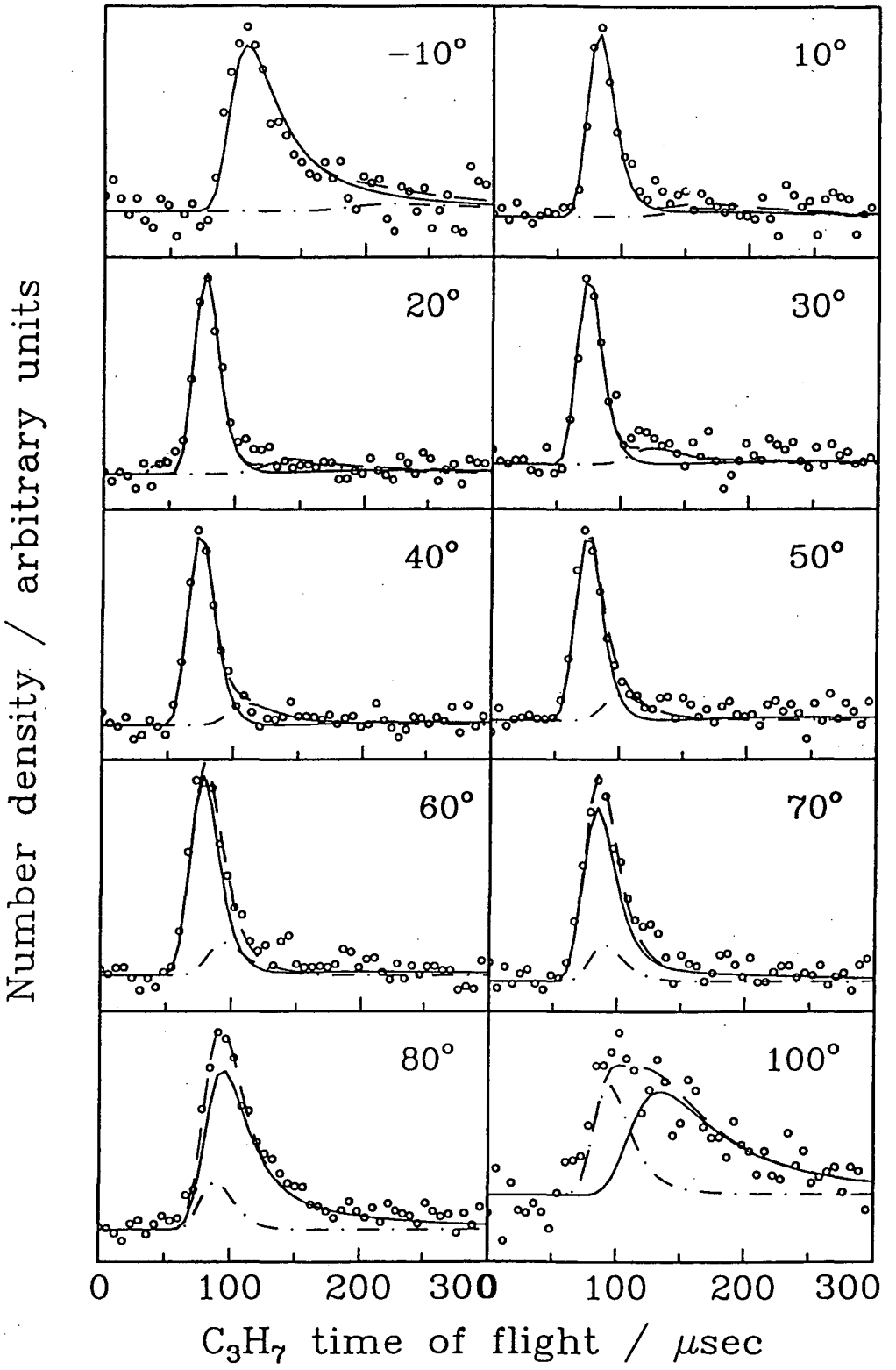
−10°
10°
20°
30°
40°
50°
60°
70°
80°
100°
Number density / arbitrary units
0
100
200
300
100
200
300
C_3H_7 time of flight / μsec

Figure 38

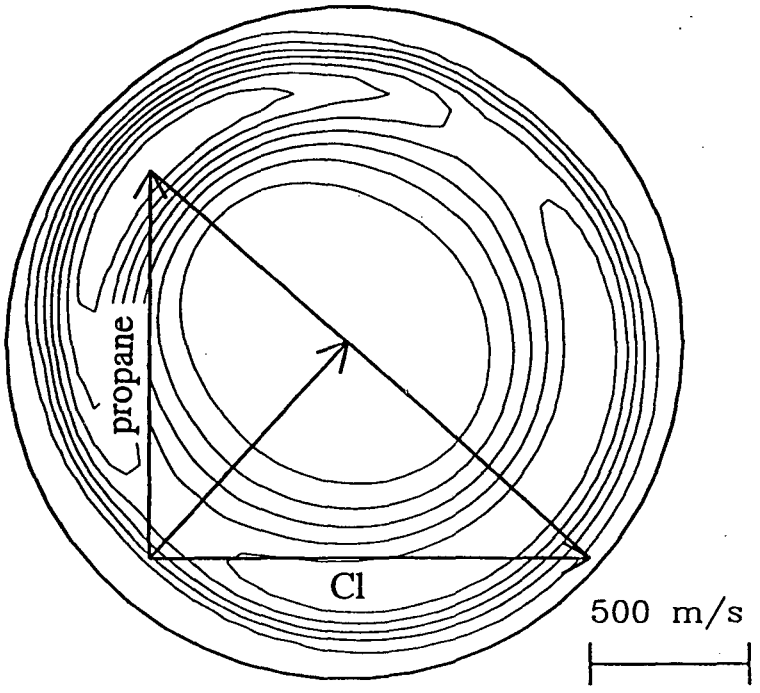

Figure 39

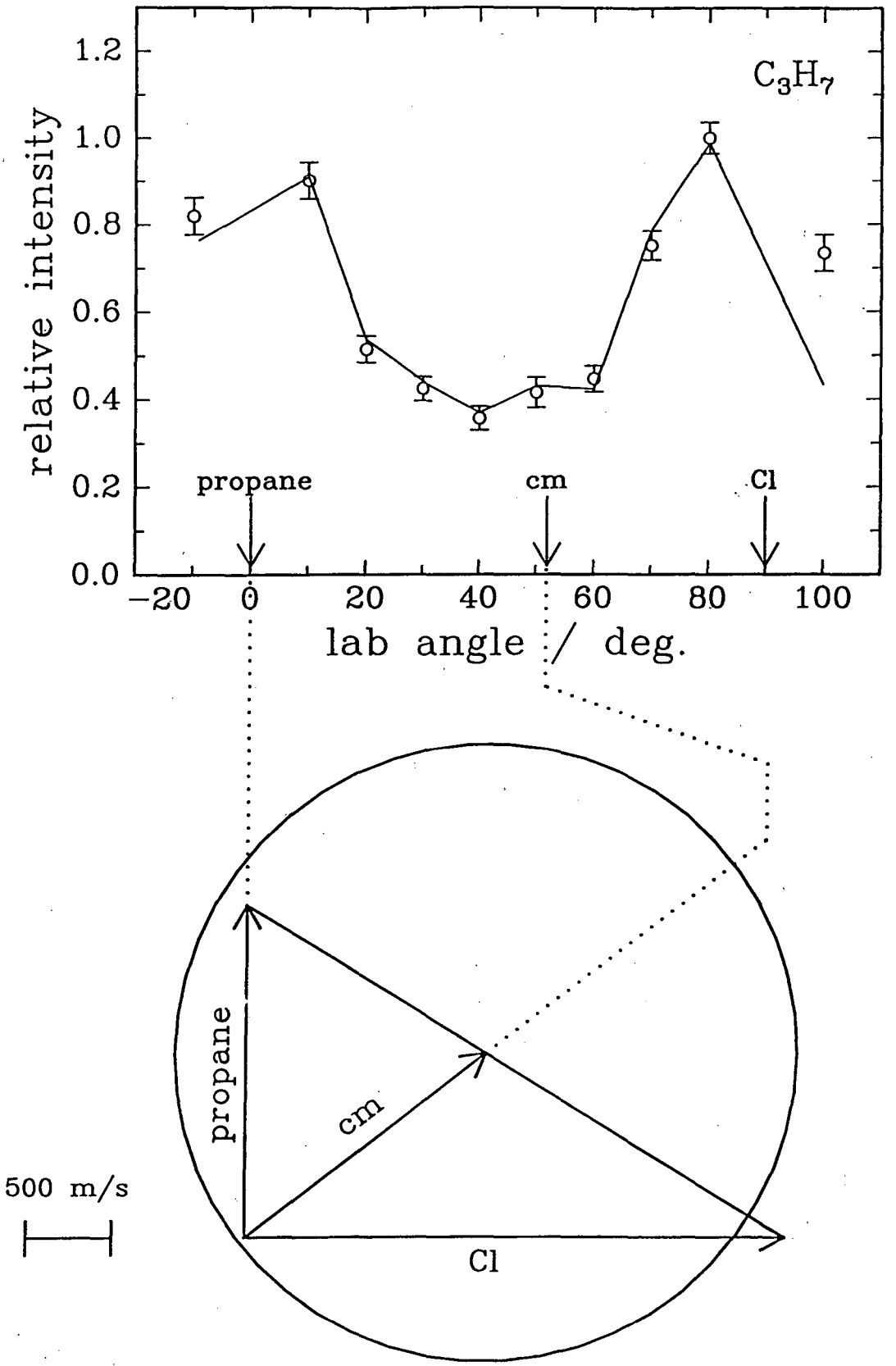
relative intensity
1.2
1.0
0.8
0.6
0.4
0.2
0.0
C_3H_7
propane
cm
Cl
−20
0
20
40
60
80
100
lab angle / deg.
propane
cm
Cl
500 m/s

Figure 40

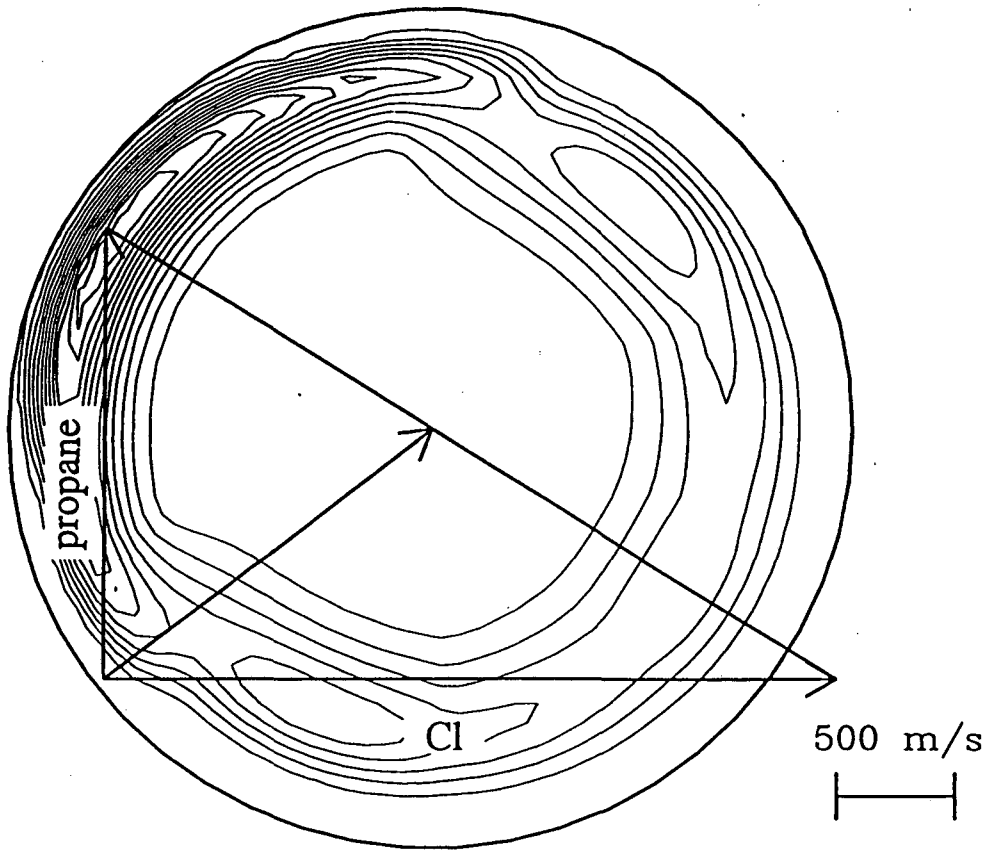

Figure 41

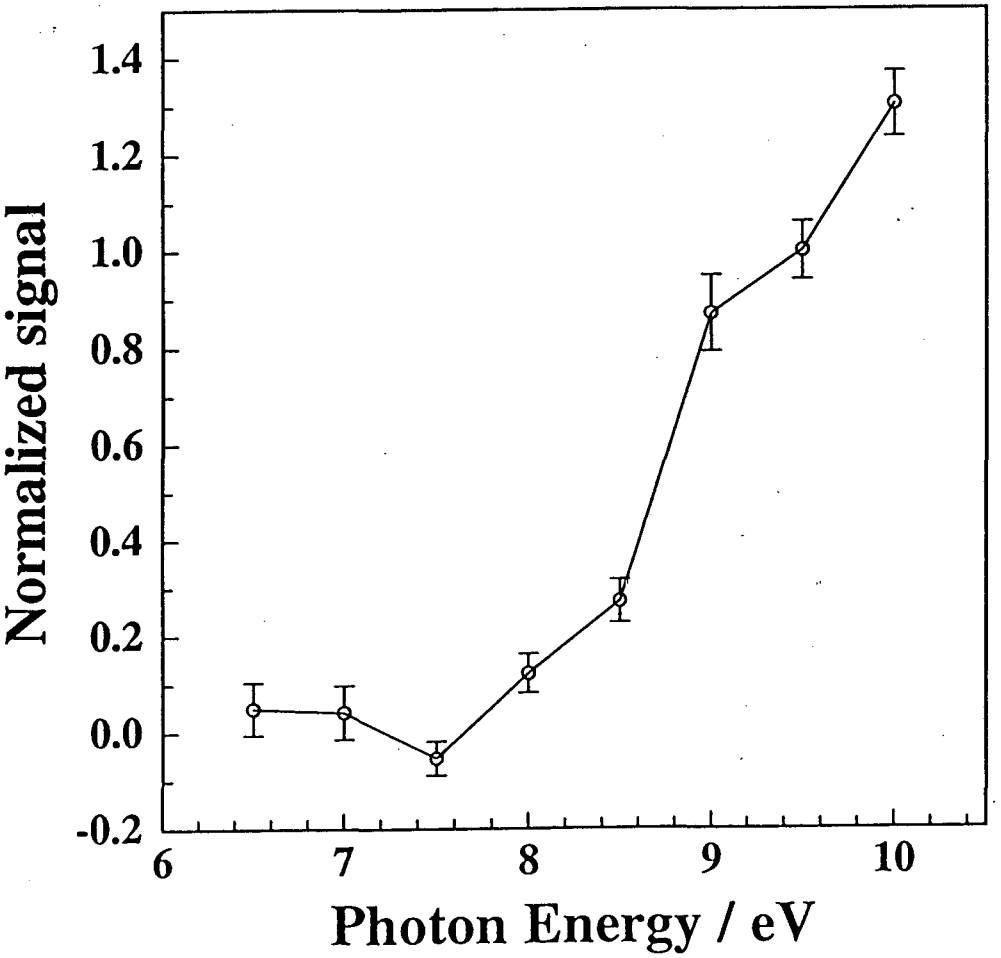
Normalized signal
1.4
1.2
1.0
0.8
0.6
0.4
0.2
0.0
-0.2
6
7
8
9
10
Photon Energy / eV

Figure 42

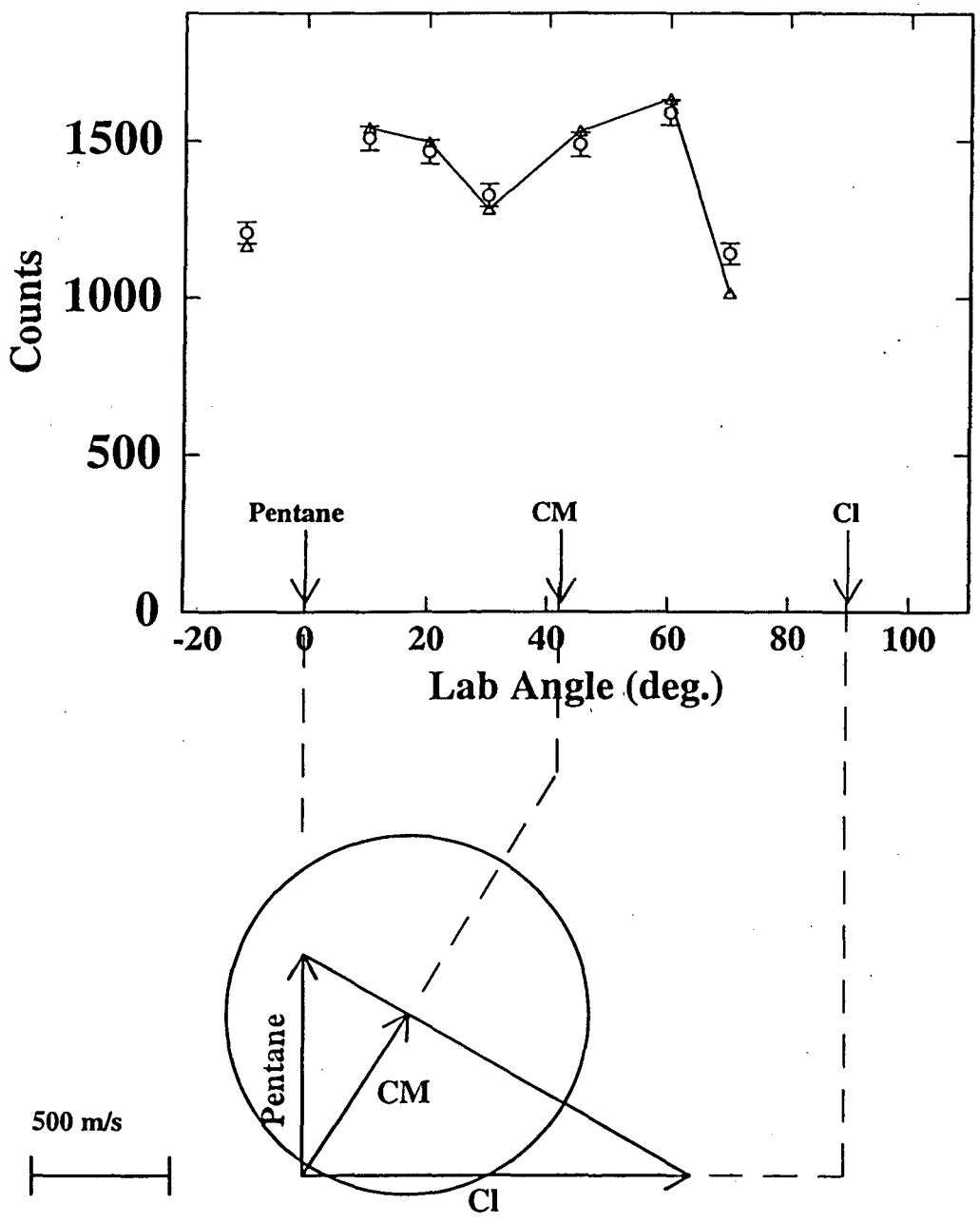
1500
1000
500
0
Counts
Pentane
CM
Cl
-20
0
20
40
60
80
100
Lab Angle (deg.)
Pentane
CM
500 m/s
Cl

Figure 43

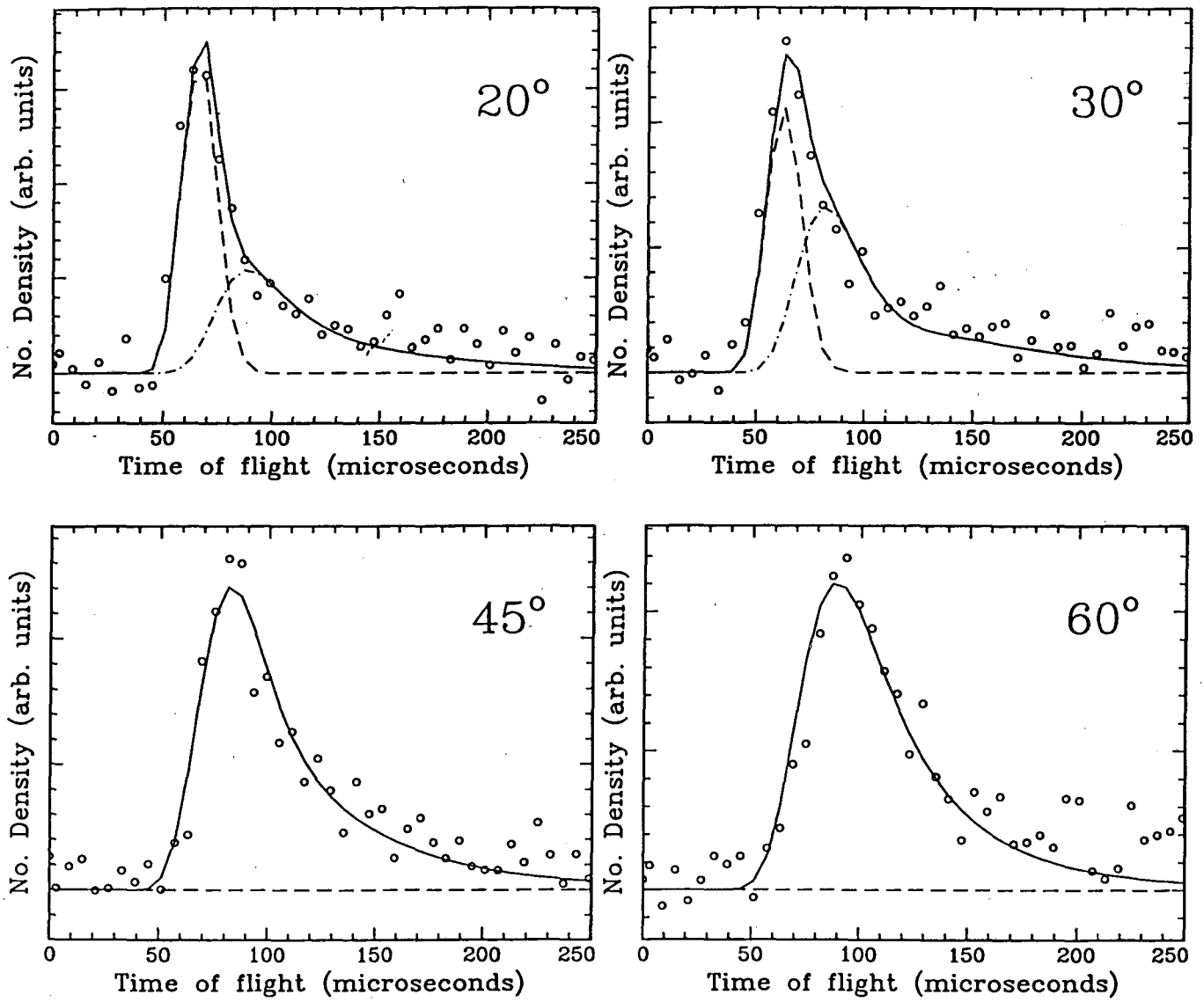
20°
30°
45°
60°
No. Density (arb. units)
Time of flight (microseconds)
0
50
100
150
200
250

Figure 44

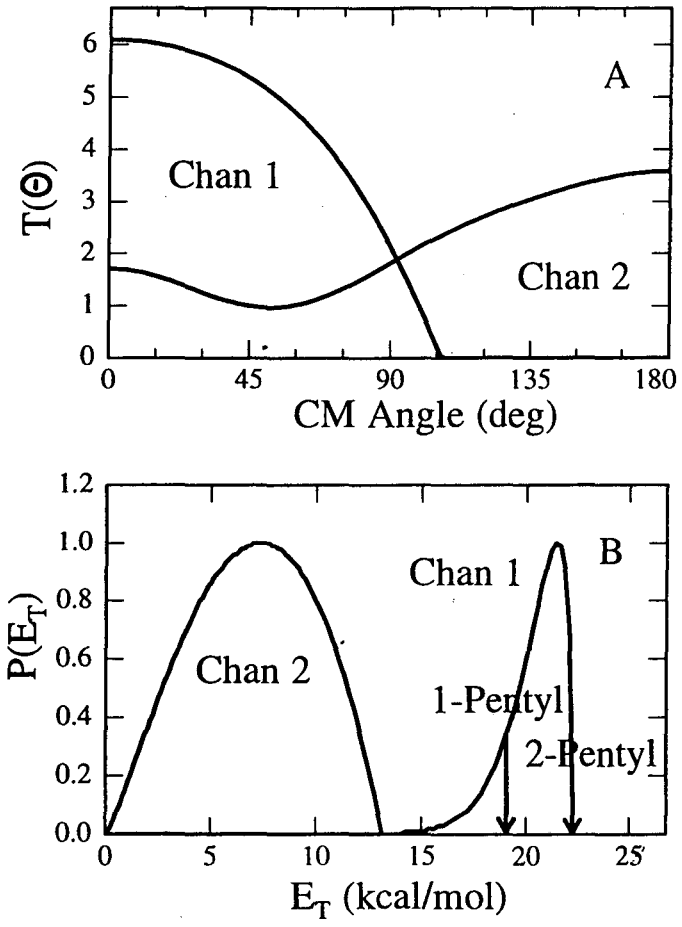
A
Chan 1
Chan 2
T(Θ)
CM Angle (deg)
B
Chan 1
Chan 2
1-Pentyl
2-Pentyl
P(E_T)
E_T (kcal/mol)

Figure 45

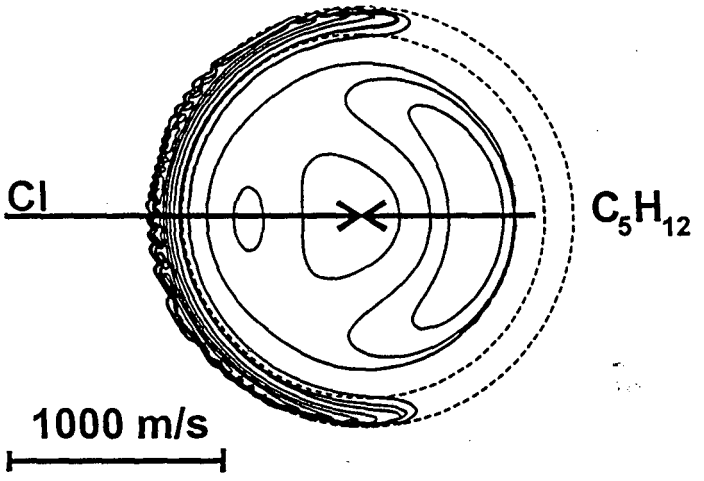

Figure 46

Ernest Orlando Lawrence Berkeley National Laboratory
One Cyclotron Road | Berkeley, California 94720

Prepared for the U.S. Department of Energy under Contract No. DE-AC03-76SF00098